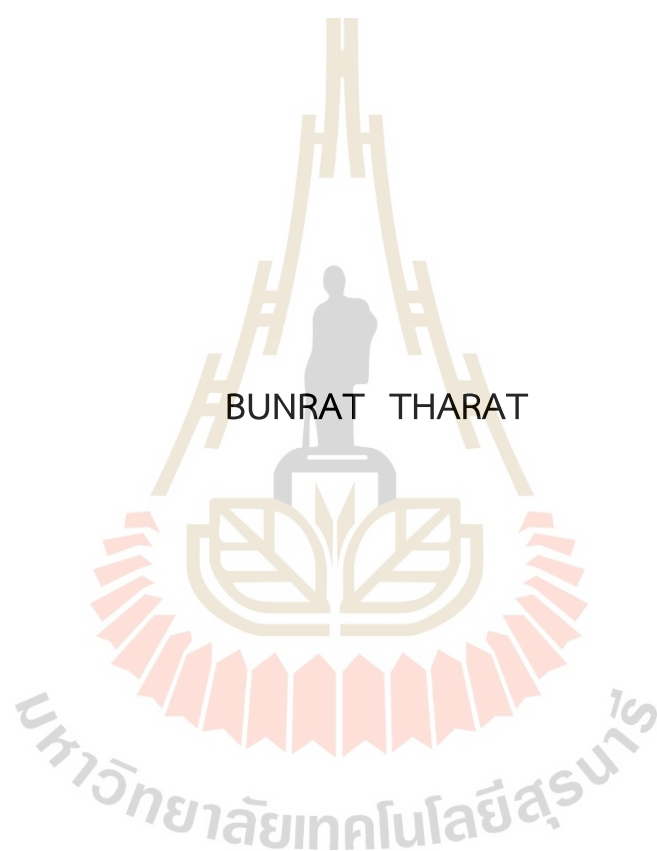MECHANISTIC STUDY OF 5-HYDROXYMETHYLFURFURAL TO
2,5-FURANDICARBOXYLIC ACID ON BETA-MANGANESE DIOXIDE
CATALYSTS: FIRST PRINCIPLES INFORMED MICROKINETIC ANALYSIS

BUNRAT THARAT

A Thesis Submitted in Partial Fulfillment of the Requirements for the
Degree of Doctor of Philosophy in Chemistry
Suranaree University of Technology
Academic Year 2023

การศึกษากลไกการเปลี่ยนไฮดรอกซีเมทิลเฟอร์ฟูรัลเป็นกรดฟูแรนไดคาร์บอกซิลิค บนตัวเร่งปฏิกิริยาเบต้าแมงกานีสไดออกไซด์ด้วยวิธีการวิเคราะห์จลนศาสตร์จุลภาค จากการคำนวณเชิงเฟิร์สต์พรินซิเพิล
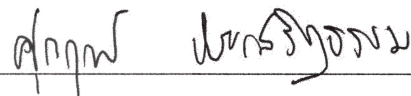
นายบุญรัตน์ ทารัตน์

วิทยานิพนธ์นี้เป็นส่วนหนึ่งของการศึกษาตามหลักสูตรปริญญาวิทยาศาสตรดุษฎีบัณฑิต
สาขาวิชาเคมี
มหาวิทยาลัยเทคโนโลยีสุรนารี
ปีการศึกษา 2566

MECHANISTIC STUDY OF 5-HYDROXYMETHYLFURFURAL TO 2,5-FURANDICARBOXYLIC ACID ON BETA-MANGANESE DIOXIDE CATALYSTS: FIRST PRINCIPLES INFORMED MICROKINETIC ANALYSIS

Suranaree University of Technology has approved this submitted in partial fulfillment of the requirements for the Degree of Doctor of Philosophy.

Thesis Examining Committee

_____

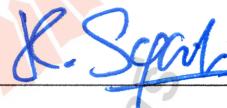(Assoc. Prof. Dr. Supareak Praserthdam)

Chairperson

_____

(Assoc. Prof. Dr. Suwit Suthirakun)

Member (Thesis Advisor)

_____

(Dr. Anchalee Junkaew)

Member (Thesis Co-Advisor)

_____
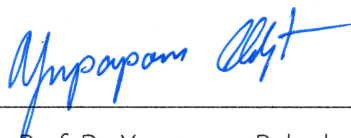
(Prof. Dr. Kritsana Sagarik)

Member

_____

(Assoc. Prof. Dr. Anyanee Kamkaew)

Member

_____   _____

(Assoc. Prof. Dr. Yupaporn Ruksakulpiwat)   (Prof. Dr. Santi Maensiri)

Acting Vice-Rector for Academic Affairs and   Dean of the Institute of Science

Quality Assurance

บุญรัตน์ ทารัตน์ : การศึกษากลไกการเปลี่ยนไฮดรอกซีเมทิลเฟอร์ฟูรัลเป็นกรดฟูแรนไดคาร์บอกซิลิค บนตัวเร่งปฏิกิริยาเบต้าแมงกานีสไดออกไซด์ด้วยวิธีการวิเคราะห์จลนศาสตร์จุลภาคจากการคำนวณเชิงเฟิร์สต์พรินซิเพิล (MECHANISTIC STUDY OF 5-HYDROXYMETHYLFURFURAL TO 2,5-FURANDICARBOXYLIC ACID ON BETA-MANGANESE DIOXIDE CATALYSTS: FIRST PRINCIPLES INFORMED MICROKINETIC ANALYSIS). อาจารย์ที่ปรึกษา : รองศาสตราจารย์ ดร.สุวิทย์ สุธีรากุล, 128 หน้า

ปฏิกิริยาแอโรบิกออกซิเดชันของ 5-ไฮดรอกซีเมทิลเฟอร์ฟูรัล (HMF) ไปเป็น 2,5-กรดฟูแรนไดคาร์บอกซิลิค (FDCA) ได้รับการศึกษาอย่างกว้างขวาง เนื่องจาก FDCA เป็นโมโนเมอร์สำหรับผลิตพอลิเอทิลีนฟูราโนเอต (PEF) ซึ่งเป็นโพลิเมอร์ชีวภาพที่รู้จักกันดี การพัฒนาตัวเร่งปฏิกิริยาที่มีประสิทธิภาพที่มีราคาไม่แพงยังคงเป็นสิ่งที่ท้าทาย เบต้าแมงกานีสไดออกไซด์ ได้ถูกเสนอว่าเป็นตัวเร่งที่ดีสำหรับปฏิกิริยานี้ อย่างไรก็ตามยังขาดความเข้าใจเชิงลึกเกี่ยวกับคุณสมบัติและกลไกการเกิดปฏิกิริยาบนพื้นผิวของตัวเร่งปฏิกิริยานี้ วิทยานิพนธ์นี้นำเสนอการศึกษากลไกการเกิดปฏิกิริยาการเปลี่ยน HMF ไปเป็น FDCA บนพื้นผิวหน้าตัดชนิด (110) ของตัวเร่งปฏิกิริยาเบต้าแมงกานีสไดออกไซด์ ด้วยระเบียบวิธีฟังก์ชันนอลความหนาแน่น และวิเคราะห์คุณสมบัติทางจลนพลศาสตร์ ผลการวิเคราะห์ทางจลนพลศาสตร์แสดงให้เห็นว่าปฏิกิริยาชอบเกิดผ่าน 2,5-ไดฟอร์มิลฟิวแรน (DFF) มากกว่าเกิดผ่าน กรด 5-ไฮดรอกซีเมทิล-2-ฟูแรน (HMFCA) ก่อนที่จะถูกเปลี่ยนไปเป็น กรด 5-ฟอร์มิล-2-ฟิวแรน (FFCA) และ FDCA ทั้งนี้ขั้นตอนในการเปลี่ยน DFF เป็น FFCA และ FFCA เป็น FDCA เป็นขั้นตอนกำหนดอัตราในการเกิดปฏิกิริยาบนพื้นผิวที่ไม่มีและมีหมู่ไฮดรอกซิล (OH) ตามลำดับ คุณสมบัติทางจลนศาสตร์ชี้ให้เห็นอย่างชัดเจนว่า หมู่ไฮดรอกซิลมีอิทธิพลและช่วยในกระบวนการเร่งปฏิกิริยาออกซิเดชันของ HMF ในขณะที่ออกซิเจนบนพื้นผิวก็มีบทบาทที่สำคัญในสภาวะพื้นผิวที่มีหมู่ OH ปริมาณต่ำ ออกซิเจนที่มีความว่องไวสูงทั้งสองชนิด (OH และออกซิเจนพื้นผิว) มีบทบาทสำคัญอย่างยิ่งรวมทั้งส่งเสริมการเกิดปฏิกิริยาออกซิเดชันของ FFCA การศึกษาเชิงคำนวณในวิทยานิพนธ์นี้ไม่เพียงแต่ช่วยอธิบายปรากฏการณ์ในระดับโมเลกุลของปฏิกิริยาบนพื้นผิวเท่านั้น แต่ผลลัพธ์ที่ได้ยังเป็นแนวทางในการปรับปรุงประสิทธิภาพของตัวเร่งปฏิกิริยาที่เป็นโลหะออกไซด์สำหรับปฏิกิริยาในการเปลี่ยน HMF เป็น FDCA อีกด้วย

สาขาวิชาเคมี

ปีการศึกษา 2566

ลายมือชื่อนักศึกษา_____

ลายมือชื่ออาจารย์ที่ปรึกษา_____

ลายมือชื่ออาจารย์ที่ปรึกษาร่วม_____

BUNRAT THARAT : MECHANISTIC STUDY OF 5-HYDROXYMETHYLFURFURAL TO 2,5-FURANDICARBOXYLIC ACID ON BETA-MANGANESE DIOXIDE CATALYSTS: FIRST PRINCIPLES INFORMED MICROKINETIC ANALYSIS. THESIS ADVISOR : ASSOC. PROF. SUWIT SUTHIRAKUN, Ph.D. 128 PP.

Keywords : 5-hydroxymethylfurfural; 2,5-furandicarboxylic acid; mechanistic study; manganese dioxide; density functional theory; microkinetic modeling
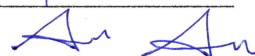
Aerobic oxidation of 5-hydroxymethylfurfural (HMF) to 2,5-furandicarboxylic acid (FDCA) has been extensively studied because FDCA is a monomer for producing polyethylene furanoate (PEF), the well-known bio-based polymers. The development of efficient catalysts with inexpensive prices is still challenging. Manganese dioxide (β-MnO$_2$) has been proposed as a promising candidate for this reaction. However, a deep understanding of the nature of the active and full reaction mechanism over this catalyst's surface is still lacking. This thesis presents a complete mechanistic study of HMF to FDCA over the β-MnO$_2$(110) surface investigated by the density functional theory (DFT) method and microkinetic analysis. Microkinetic analysis suggests that the 2,5-diformylfuran (DFF) path is preferable than the 5-hydroxymethyl-2-furan carboxylic acid (HMFCA) path before proceeding to the 5-formyl-2-furan carboxylic acid (FFCA) and FDCA. The DFF-to-FFCA and FFCA-to-FDCA are the rate-determining steps on the bare and hydroxylated surfaces, respectively. The kinetic properties clearly suggest that OH promotes HMF oxidation, while surface oxygen also plays a role in the low OH coverage. Both active oxygen species (i.e. OH and surface oxygen) are crucial to promote the FFCA oxidation reaction. This thesis not only reveals the molecular-scale phenomena of the surface reaction, but the outputs also guide the way to improve the activity of metal oxide-based catalysts for the HMF to FDCA reaction.

School of Chemistry

Academic Year 2023

Student's Signature _____

Advisor's Signature _____

Co-Advisor's Signature _____

ACKNOWLEDGEMENTS

Bunrat Tharat

CONTENTS

CONTENTS (Continued)

CONTENTS (Continued)

LIST OF TABLES

LIST OF FIGURES

LIST OF FIGURES (Continued)

LIST OF FIGURES (Continued)

LIST OF ABBREVIATIONS

HMF	=	5-hydroxymethylfurfural
HMFCA	=	5-hydroxymethyl-2-furan carboxylic acid
DFF	=	2,5-diformylfuran
FFCA	=	5-formyl-2-furan carboxylic acid
FDCA	=	2,5-furandicarboxylic acid
LA	=	levulinic acid
DMF	=	2,5-dimethylfuran
MA	=	Maleic anhydride
PEF	=	Polyethylene furanoate
PET	=	Polyethylene terephthalate
LDA	=	Local density approximation
PAW	=	Projector-augmented wave
PBE	=	Perdew-Burke-Ernzerhof
CI-NEB	=	Climbing image-nudged elastic band
NEB	=	Nudged elastic band
TS	=	Transition state
DFT	=	Density functional theory
VASP	=	Vienna ab initio simulation package
GGA	=	Generalized gradient approximation
LDA	=	Local density approximation
XC	=	Exchange-correlation
SCF	=	Self-consistent field
KS	=	Kohn-Sham equation
RDS	=	Rate-determining step
DMSO	=	Dimethyl sulfoxide
TST	=	Transition state theory
ODEs	=	Ordinary differential equations

LIST OF ABBREVIATIONS (Continued)

XRD	=	X-ray diffraction
BET	=	Brunauer–Emmett–Teller
FE-SEM	=	Femission-scanning electron microscope
HPLC	=	High-performance liquid chromatography
LHSV	=	Liquid hourly space velocity
MKM	=	Microkinetic models

CHAPTER I

INTRODUCTION

Biomass is an abundant natural resource, including a large amount of agricultural waste, such as rice husk, palm shell, and bagasse fiber. Therefore, biomass resources have been very popular for producing biofuel, bioenergy, and value-added products because they are inexpensive.

5-hydroxymethylfurfural (HMF), a versatile platform chemical derived from biomass, has been used as a precursor for synthesizing a variety of bio-chemicals, bio-fuels (van Putten, van der Waal et al., 2013), and value-added products. (Tong, Ma et al., 2010, Yuan, Liu et al., 2020). Companies can produce a variety of value-added chemicals from HMF such as 2-furoic acid, levulinic acid (LA), 2,5-dimethylfuran (DMF), 2,5-furandicarboxylic acid (FDCA), and maleic anhydride (MA) (Hu, Xu et al., 2018). 2,5-furandicarboxylic acid (FDCA) is one of the most attractive compounds derived from an aerobic oxidation of HMF. It is a monomer of polyethylene 2,5-furandicarboxylate (PEF), the well-known green polymers for replacing the oil derivative polyethylene terephthalate (PET) (Sajid, Zhao et al., 2018, Yang, Xu et al., 2021).

The thermochemical HMF oxidation via the heterogeneous catalysis has potential for the large-scale FDCA production due to its less required steps for catalyst recovery and regeneration compared to the homogeneous catalysis. Until now, there are still many challenges for scaling up the FDCA production including development of highly efficient catalysts (Sajid, Zhao et al., 2018, Deshan, Atanda et al., 2020, Yang, Xu et al., 2021). According to a previously proposed reaction mechanism, (Amaniampong, Trinh et al., 2015, Han, Li et al., 2017, Sajid, Zhao et al., 2018, Hayashi, Yamaguchi et al., 2019, Liu, Cao et al., 2019) the oxidation of HMF into FDCA occurs through three intermediates (following **Figure 1.1**): the HMF oxidation reaction ($2C_6H_6O_3 + 3O_2 \longrightarrow 2C_6H_4O_5 + 2H_2O$), HMF is oxidized to 5-formyl-

2-furan carboxylic acid (FFCA) via 5-hydroxymethyl-2-furan carboxylic acid (HMFCA) or 2,5-diformylfuran (DFF) intermediates before further oxidizing to FDCA as a final product. Due to the complicated pathways, the full mechanism and the insight into the high catalytic performance, which are decisive for rational design highly efficient catalysts, are still limited.
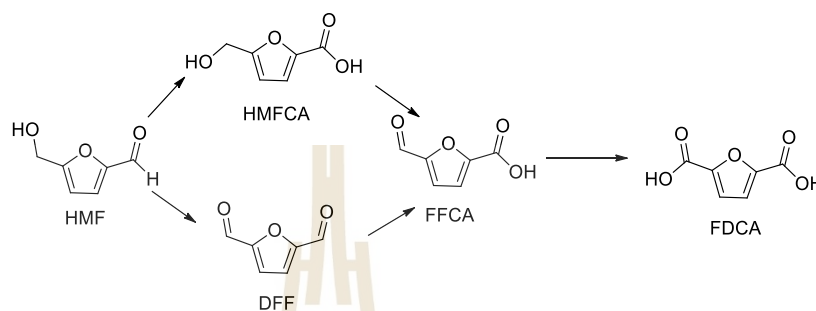
Figure 1.1 Reaction pathway of HMF oxidation to produce FDCA.

Currently, noble metal-based heterogeneous catalysts, such as Au (Casanova, Iborra et al., 2009, Cai, Ma et al., 2013, Megías-Sayago, Lolli et al., 2019), Pd (Lei, Yu et al., 2016), Pt (Vinke, van Dam et al., 1990, Miao, Wu et al., 2015, Zhou, Deng et al., 2015), and Ru (Yi, Teong et al., 2016, Mishra, Lee et al. 2017) on supports are most common due to their excellent catalytic activity, good recyclability, stability, and high performance. In addition, many bimetallic catalysts for HMF oxidation reaction, such as Au-Cu/TiO_2 (Pasini, Piccinini et al., 2011, Albonetti, Pasini et al., 2012), Au-Pd/CNT (Wan, Zhou et al., 2014), Pt-Bi/TiO_2 (Ait Rass, Essayem et al., 2015) and Pt-Pb/C (Verdeguer, Merat et al., 1993) have been proposed as good candidates for this reaction. These catalysts provided a high yield of FDCA (≥ 90 %), albeit their expensive prices are the major drawback for using in mass FDCA production.

Developing non-noble metal heterogeneous catalysts for conversion of HMF to FDCA could reduce cost of catalysts. Though the catalytic activity of these catalysts may not be as good as the noble metal catalysts, they still provide good catalytic performance with cheap, good recyclability, and stability. Inexpensive metal oxide catalysts such as MnO_2 (Saha, Gupta et al., 2013, Hayashi, Komanoya et al., 2017, Tong, Yu et al., 2017, Yu, Liu et al., 2018, Yamaguchi, Aono et al., 2020),

CuO (Ren, Song et al., 2018), Co_3O_4 (Ren, Song et al., 2018), $MnFe_2O_4$, (Zhang, Sun et al., 2018) and so on have been developed and tested for this reaction. Among them, β-MnO_2 is one of the promising candidates having good catalytic activity, good stability, and good recyclability (Hayashi, Komanoya et al., 2017, Hayashi, Oba et al., 2019, Aono, Hayashi et al., 2020, Cheng, Guo et al., 2021).

To improve the catalytic efficiency and understanding of the reaction mechanisms of HMF oxidation on a non-noble metal catalyst, this field has required both computational and experimental viewpoints. However, the catalytic HMF oxidation reaction at the molecular level is not easily accessible with conventional experiments. Molecular modeling can provide insight into properties that are difficult to attain by experiments. Due to the complicated pathways, the full mechanism and the insight into the high catalytic performance, which are decisive for rational design highly efficient catalysts, are still limited.

In experiment, DFF has been found as a key intermediate in the HMF-to-FFCA step (Gawade, Nakhate et al., 2018, Lin, Oh et al., 2021, Yu, Chen et al., 2021, Zhu, Cheng et al., 2022), and the FFCA to FDCA step is proposed as a rate determining step over Mn oxide and other oxide catalysts (Hayashi, Oba et al., 2019, Pal, Kumar et al., 2020, Wang, Lai et al., 2022). Most theoretical work focused on the FFCA to FDCA step or the oxygen vacancy formation in metal oxide-based catalysts (i.e. MnO_2, CuO_2 and Co_3O_4) (Ren, Song et al., 2018, Hayashi, Oba et al., 2019).

In literature, theoretical studies proposed that the low oxygen vacancy formation energy was the key factor for the high catalytic performance of β-MnO_2 compared to other MnO_2 allotropes (Hayashi, Oba et al., 2019, Yao and Wang, 2021). The active lattice oxygen on the catalyst surface promotes the catalytic performance of MnO_2 by assisting the activation of C–H and O–H of intermediates (Yao and Wang, 2021). To the best of our knowledge, many studies focus on the effect of lattice oxygen or superoxide species, however theoretical studies considering the effect of a hydroxyl group (OH), another possible active oxygen species on metal oxide-based catalysts, are scarce. Typically, a hydroxyl group is easily formed via hydroxylation or adding OH source to active metal oxides. Some

theoretical studies proposed that not only superoxide species, but hydroxyl group also plays a crucial role in the HMF-to-FDCA reaction in metal catalysts such as Pt, Pt and Au (Davis, Zope et al., 2012, Liu, Ma et al., 2019, Chen, Wang et al., 2021). Likewise, hydroxide ions (OH^-) from dissociated H_2O were suggested to play a significant role in the nucleophilic addition of OH– to the carbonyl group for this reaction in $Co_3O_4/Mn_{0.2}Co$ (Gao, Yin et al., 2020). The high acidity of the $Co_3O_4/Mn_{0.2}Co$ catalyst leads to the strong adsorption of HMF, including enhanced ability to form the carboxylic acid group of intermediate and FDCA. The experiment suggested that the availability of both Brønsted and Lewis acid sites on metal oxide surfaces is essential to achieve the high yield of FDCA (Mishra, Lee et al., 2017, Gao, Yin et al., 2020). However, clear explanation about the OH effect has not been investigated by theoretical study.

Herein, great catalytic performance of our synthesized MnO_2 was attested via retained high yield, greater than 85 mol% FDCA, in continuous flow. The role of hydroxyl group on the HMF oxidation in MnO_2 was assured by (i) comparing mechanism and kinetic properties between the non-hydroxylated and hydroxylated surfaces by plane-wave based density functional theory calculation (DFT) and microkinetic modeling and (ii) comparing reactions in water and dimethyl sulfoxide (DMSO) by experiment. Computational and experimental results successfully prove that both active surface oxygen and OH promote the aerobic oxidation of HMF to FDCA in $\beta-MnO_2$. This insight is necessary for development and design high performance metal oxide-based catalysts for this reaction.

1.1   Research objectives

Here we use various computational tools to obtain an understanding at molecular level of the HMF oxidation reaction mechanism to produce FDCA on $\beta-MnO_2$ catalysts as follows:

1.1.1   To study the mechanism of HMF oxidation to FDCA on non-hydroxylated and hydroxylated surfaces $\beta-MnO_2$–based catalysts using the first-principles method based on DFT calculations.

1.1.2   To calculate reaction rates, apparent activation energies, and identify rate-limiting steps using a microkinetic model based on the DFT results.

1.1.3   To study the roles of active surface oxygen and OH species on surface catalysts for HMF oxidation reaction.

A deeper molecular level understanding may yield further development and designs of reusable, low-cost, and effective $\beta-MnO_2$ catalysts for HMF conversion.

1.2   Scope and limitation of the study

This thesis aims to understand catalytic reactions and to develop low cost and effective $\beta-MnO_2$ based catalysts for the HMF conversion to FDCA by the computational methods. Mechanistic study of HMF oxidation to FDCA on non-hydroxylated and hydroxylated surfaces $\beta-MnO_2$–based catalysts is focused herein. This work was carried out a planewave-based density functional theory (DFT) (Kohn and Sham, 1965) implemented in Vienna ab initio simulation package (VASP 5.4.4). All electronic structure calculations used the Perdew-Burke-Ernzernhof functional (PBE) form of the generalized gradient approximation (GGA) (Perdew, Burke et al., 1996). The ultra-soft pseudopotential with projector augmented wave (PAW) method (Blöchl, 1994, Kresse and Joubert, 1999) was used to describe the nuclei and core electronic states. For describing the strongly correlated d electrons of Mn in $\beta-MnO_2$, the DFT+U approach was used with a Hubbard-like terms U = 2.8 eV and J = 1.2 eV for Mn 3d electron, as suggested by Mellan, T. A., et al. (Liechtenstein, Anisimov et al., 1995, Mellan, Maenetja et al., 2013, Song, Yan et al., 2018). In this work, an antiferromagnetic state was used for the $\beta-MnO_2$ model as observed by previous work (Paik, Osegovic et al., 2001, Sato, Wakiya et al., 2001). The climbing image nudged elastic band (CINEB) (Smidstrup, Pedersen et al., 2014), and DIMER methods (Henkelman and Jónsson, 1999, Henkelman and Jónsson, 2001, Olsen, Kroes et al., 2004) were employed for finding the transition state (TS).

 Microkinetic modeling was used to calculate reaction rates, and apparent activation energies, and identify rate-limiting steps at reaction conditions. In addition, the computation results have been compared with the experimental studies, which

were carried out by Dr. Kajornsak Faungnawakij et al., to understand the factors that influence the catalytic performance of this catalyst.

1.3 References

Ait Rass, H., Essayem, N., and Besson, M. (2015). Selective aerobic oxidation of 5-HMF into 2,5-furandicarboxylic acid with Pt catalysts supported on TiO_2- and ZrO_2-based supports. *ChemSusChem., 8,* 1206-1217.

Albonetti, S., Pasini, T., Lolli, A., Blosi, M., Piccinini, M., Dimitratos, N., Lopez-Sanchez, J.A., Morgan, D.J., Carley, A.F., Hutchings, G.J., and Cavani, F. (2012). Selective oxidation of 5-hydroxymethyl-2-furfural over TiO_2-supported gold–copper catalysts prepared from preformed nanoparticles: Effect of Au/Cu ratio. *Catal. Today., 195,* 120-126.

Amaniampong, P.N., Trinh, Q.T., Wang, B., Borgna, A., Yang, Y., and Mushrif, S.H. (2015). Biomass oxidation: formyl C-H bond activation by the surface lattice oxygen of regenerative CuO nanoleaves. *Angew. Chem., 54,* 8928-8933.

Aono, R., Hayashi, E., Yamaguchi, Y., Kamata, K., and Hara, M. (2020). Template-free synthesis of mesoporous beta-MnO_2 nanoparticles: structure, formation mechanism, and catalytic properties. *ACS Appl. Mater. Interfaces., 12,* 36004-36013.

Blöchl, P.E. (1994). Projector augmented-wave method. *Phys. Rev. B., 50,* 17953-17979.

Cai, Ma, H., Zhang, J., Song, Q., Du, Z., Huang, Y., and Xu, J. (2013). Gold nanoclusters confined in a supercage of Y zeolite for aerobic oxidation of HMF under mild conditions. *Chem. Eur. J., 19,* 14215-14223.

Casanova, Iborra, S., and Corma, A. (2009). Biomass into chemicals: aerobic oxidation of 5-hydroxymethyl-2-furfural into 2,5-furandicarboxylic acid with gold nanoparticle catalysts. *ChemSusChem., 2,* 1138-1144.

Chen, C., Wang, L., Zhu, B., Zhou, Z., El-Hout, S.I., Yang, J., and Zhang, J. (2021). 2,5-Furandicarboxylic acid production via catalytic oxidation of 5-hydroxymethylfurfural: catalysts, processes and reaction mechanism. *J. Energy Chem., 54,* 528-554.

Cheng, F., Guo, D., Lai, J., Long, M., Zhao, W., Liu, X., and Yin, D. (2021). Efficient base-free oxidation of 5-hydroxymethylfurfural to 2,5-furandicarboxylic acid over copper-doped manganese oxide nanorods with tert-butanol as solvent. *Front. Chem. Sci. Eng., 15,* 960–968.

Davis, S.E., Zope, B.N., and Davis, R.J. (2012). On the mechanism of selective oxidation of 5-hydroxymethylfurfural to 2,5-furandicarboxylic acid over supported Pt and Au catalysts. *Green Chem., 14,* 143-147.

Deshan, A.D.K., Atanda, L., Moghaddam, L., Rackemann, D.W., Beltramini, J., and Doherty, W.O.S. (2020). Heterogeneous catalytic conversion of sugars into 2,5-furandicarboxylic acid. *Front Chem., 8,* 659.

Gao, T., Yin, Y., Zhu, G., Cao, Q., and Fang, W. (2020). Co_3O_4 NPs decorated Mn-Co-O solid solution as highly selective catalyst for aerobic base-free oxidation of 5-HMF to 2,5-FDCA in water. *Catal. Today., 355,* 252-262.

Gawade, A.B., Nakhate, A.V., and Yadav, G.D. (2018). Selective synthesis of 2, 5-furandicarboxylic acid by oxidation of 5-hydroxymethylfurfural over $MnFe_2O_4$ catalyst. *Catal. Today., 309,* 119-125.

Han, X., Li, C., Liu, X., Xia, Q., and Wang, Y. (2017). Selective oxidation of 5-hydroxymethylfurfural to 2,5-furandicarboxylic acid over $MnO_x–CeO_2$ composite catalysts. *Green Chem., 19,* 996-1004.

Hayashi, Yamaguchi, Y., Kamata, K., Tsunoda, N., Kumagai, Y., Oba, F., and Hara, M. (2019). Effect of MnO_2 crystal structure on aerobic oxidation of 5-hydroxymethylfurfural to 2,5-furandicarboxylic acid. *J. Am. Chem. Soc., 141,* 890-900.

Hayashi, E., Komanoya, T., Kamata, K., and Hara, M. (2017). Heterogeneously-catalyzed aerobic oxidation of 5-hydroxymethylfurfural to 2,5-furandicarboxylic acid with MnO_2. *ChemSusChem., 10,* 654-658.

Hayashi, E., Oba, F., Yamaguchi, Y., Kamata, K., Tsunoda, N., Kumagai, Y., and Hara, M. (2019). Effect of MnO_2 crystal structure on aerobic oxidation of 5-hydroxymethylfurfural to 2,5-furandicarboxylic acid. *J. Am. Chem. Soc., 141,* 890-900.

Henkelman, G., and Jónsson, H. (1999). A dimer method for finding saddle points on high dimensional potential surfaces using only first derivatives. *J. Chem. Phys., 111,* 7010-7022.

Henkelman, G., and Jónsson, H. (2001). Long time scale kinetic Monte Carlo simulations without lattice approximation and predefined event table. *J. Chem. Phys., 115,* 9657-9666.

Hu, L., Xu, J., Zhou, S., He, A., Tang, X., Lin, L., Xu, J., and Zhao, Y. (2018). Catalytic advances in the production and application of biomass-derived 2,5-dihydroxymethylfuran. *ACS Catalysis., 8,* 2959-2980.

Kohn, W., and Sham, L.J. (1965). Self-consistent equations including exchange and correlation effects. *Phys. Rev., 140,* A1133-A1138.

Kresse, G., and Joubert, D. (1999). From ultrasoft pseudopotentials to the projector augmented-wave method. *Phys. Rev. B., 59,* 1758-1775.

Lei, D., Yu, K., Li, M.-R., Wang, Y., Wang, Q., Liu, T., Liu, P., Lou, L.-L., Wang, G., and Liu, S. (2016). Facet effect of single-crystalline Pd nanocrystals for aerobic oxidation of 5-hydroxymethyl-2-furfural. *ACS Catal., 7,* 421-432.

Liechtenstein, A.I., Anisimov, V.I., and Zaanen, J. (1995). Density-functional theory and strong interactions: Orbital ordering in Mott-Hubbard insulators. *Phys. Rev. B., 52,* R5467-R5470.

Lin, K.A., Oh, W.D., Zheng, M.W., Kwon, E., Lee, J., Lin, J.Y., Duan, X., and Ghanbari, F. (2021). Aerobic oxidation of 5-hydroxymethylfurfural into 2,5-diformylfuran using manganese dioxide with different crystal structures: A comparative study. *J. Colloid Interface Sci., 592,* 416-429.

Liu, Ma, H.-Y., Lei, D., Lou, L.-L., Liu, S., Zhou, W., Wang, G.-C., and Yu, K. (2019). Active oxygen species promoted catalytic oxidation of 5-hydroxymethyl-2-furfural on facet-specific Pt nanocrystals. *ACS Catal., 9,* 8306-8315.

Liu, H., Cao, X., Wei, J., Jia, W., Li, M., Tang, X., Zeng, X., Sun, Y., Lei, T., Liu, S., and Lin, L. (2019). Efficient aerobic oxidation of 5-hydroxymethylfurfural to 2,5-diformylfuran over Fe_2O_3-promoted MnO_2 catalyst. *ACS Sustain. Chem. Eng., 7,* 7812-7822.

Megías-Sayago, C., Lolli, A., Ivanova, S., Albonetti, S., Cavani, F., and Odriozola, J.A. (2019). Au/Al$_2$O$_3$ – efficient catalyst for 5-hydroxymethylfurfural oxidation to 2,5-furandicarboxylic acid. *Catal. Today., 333,* 169-175.

Mellan, T.A., Maenetja, K.P., Ngoepe, P.E., Woodley, S.M., Catlow, C.R.A., and Grau-Crespo, R. (2013). Lithium and oxygen adsorption at the β-MnO$_2$ (110) surface. *J. Mater. Chem. A., 1,* 14879-14887.

Miao, Wu, T., Li, J., Yi, T., Zhang, Y., and Yang, X. (2015). Aerobic oxidation of 5-hydroxymethylfurfural (HMF) effectively catalyzed by a Ce$_{0.8}$Bi$_{0.2}$O$_2$−δ supported Pt catalyst at room temperature. *RSC Adv., 5,* 19823-19829.

Mishra, D.K., Lee, H.J., Kim, J., Lee, H.-S., Cho, J.K., Suh, Y.-W., Yi, Y., and Kim, Y.J. (2017). MnCo$_2$O$_4$ spinel supported ruthenium catalyst for air-oxidation of HMF to FDCA under aqueous phase and base-free conditions. *Green Chem., 19,* 1619-1623.

Mishra, D.K., Lee, H.J., Kim, J., Lee, H.-S., Cho, J.K., Suh, Y.-W., Yi, Y., and Kim, Y.J. (2017). MnCo$_2$O$_4$ spinel supported ruthenium catalyst for air-oxidation of HMF to FDCA under aqueous phase and base-free conditions. *Green Chem., 19,* 1619-1623.

Olsen, R.A., Kroes, G.J., Henkelman, G., Arnaldsson, A., and Jónsson, H. (2004). Comparison of methods for finding saddle points without knowledge of the final states. *J. Chem. Phys., 121,* 9776-9792.

Paik, Y., Osegovic, J.P., Wang, F., Bowden, W., and Grey, C.P. (2001). ^{2}H MAS NMR Studies of the manganese dioxide tunnel structures and hydroxides used as cathode materials in primary batteries. *J. Am. Chem. Soc., 123,* 9367-9377.

Pal, P., Kumar, S., Devi, M.M., and Saravanamurugan, S. (2020). Oxidation of 5-hydroxymethylfurfural to 5-formyl furan-2-carboxylic acid by non-precious transition metal oxide-based catalyst. *J. of Supercritical Fluids., 160,* 104812.

Pasini, T., Piccinini, M., Blosi, M., Bonelli, R., Albonetti, S., Dimitratos, N., Lopez-Sanchez, J.A., Sankar, M., He, Q., Kiely, C.J., Hutchings, G.J., and Cavani, F. (2011). Selective oxidation of 5-hydroxymethyl-2-furfural using supported gold–copper nanoparticles. *Green Chem., 13,* 2091-2099.

Perdew, J.P., Burke, K., and Ernzerhof, M. (1996). Generalized gradient approximation made simple. *Phys. Rev. Lett., 77,* 3865-3868.

Ren, J., Song, K.-h., Li, Z., Wang, Q., Li, J., Wang, Y., Li, D., and Kim, C.K. (2018). Activation of formyl C-H and hydroxyl O-H bonds in HMF by the CuO(111) and Co_3O_4 (110) surfaces: A DFT study. *Appl. Surf. Sci., 456,* 174-183.

Saha, B., Gupta, D., Abu-Omar, M.M., Modak, A., and Bhaumik, A. (2013). Porphyrin-based porous organic polymer-supported iron(III) catalyst for efficient aerobic oxidation of 5-hydroxymethyl-furfural into 2,5-furandicarboxylic acid. *J. Catal., 299,* 316-320.

Sajid, M., Zhao, X., and Liu, D. (2018). Production of 2,5-Furandicarboxylic acid (FDCA) from 5-hydroxymethylfurfural (HMF): recent progress focusing on the chemical-catalytic routes. *Green Chem., 20,* 5427-5453.

Sato, H., Wakiya, K., Enoki, T., Kiyama, T., Wakabayashi, Y., Nakao, H., and Murakami, Y. (2001). Magnetic structure of β-MnO_2 x-ray magnetic scattering study. *J. Phys. Soc. Jpn., 70,* 37-40.

Smidstrup, S., Pedersen, A., Stokbro, K., and Jonsson, H. (2014). Improved initial guess for minimum energy path calculations. *J. Chem. Phys., 140,* 214106.

Song, Z., Yan, Z., Yang, X., Bai, H., Duan, Y., Yang, B., and Leng, L. (2018). First principles density functional theory study of Pb doped α-MnO_2 catalytic materials. *Chem. Phys. Lett., 695,* 216-221.

Tong, X., Ma, Y., and Li, Y. (2010). Biomass into chemicals: Conversion of sugars to furan derivatives by catalytic processes. *Appl. Catal. A: Gen., 385,* 1-13.

Tong, X., Yu, L., Chen, H., Zhuang, X., Liao, S., and Cui, H. (2017). Highly efficient and selective oxidation of 5-hydroxymethylfurfural by molecular oxygen in the presence of Cu-MnO_2 catalyst. *Catal. Comm., 90,* 91-94.

van Putten, R.-J., van der Waal, J.C., de Jong, E., Rasrendra, C.B., Heeres, H.J., and de Vries, J.G. (2013). Hydroxymethylfurfural, a versatile platform chemical made from renewable resources. *Chem. Rev., 113,* 1499-1597.

Verdeguer, P., Merat, N., and Gaset, A. (1993). Oxydation catalytique du HMF en acide 2,5-furane dicarboxylique. *J. Mol. Catal., 85,* 327-344.

Vinke, P., van Dam, H.E., and van Bekkum, H. (1990). Platinum catalyzed oxidation of 5-hydroxymethylfurfural. *Stud. Surf. Sci. Catal, 55,* 147-158.

Wan, X., Zhou, C., Chen, J., Deng, W., Zhang, Q., Yang, Y., and Wang, Y. (2014). Base-free aerobic oxidation of 5-hydroxymethyl-furfural to 2,5-furandicarboxylic acid in water catalyzed by functionalized carbon nanotube-supported Au–Pd alloy nanoparticles. *ACS Catal., 4,* 2175-2185.

Wang, F., Lai, J., Liu, Z., Wen, S., and Liu, X. (2022). Copper-manganese oxide for highly selective oxidation of 5-hydroxymethylfurfural to bio-monomer 2, 5-furandicarboxylic acid. *Biomass Conv. Bioref., 13,* 1-12.

Yamaguchi, Y., Aono, R., Hayashi, E., Kamata, K., and Hara, M. (2020). Template-free synthesis of mesoporous β-MnO_2 nanoparticles: Structure, formation mechanism, and catalytic properties. *ACS Appl. Mater. Interfaces., 12,* 36004-36013.

Yang, Y., Xu, D., Zhang, B., Xue, Z., and Mu, T. (2021). Substrate molecule adsorption energy: An activity descriptor for electrochemical oxidation of 5-Hydroxymethylfurfural (HMF). *Chem. Eng. J., 433,* 133842.

Yao, Y.-F., and Wang, G.-C. (2021). Mechanism insights into the aerobic oxidation of 5-hydroxymethylfurfural to 2,5-furandicarboxylic acid over MnO_2 catalysts. *J. Phys. Chem. C., 125,* 3818-3826.

Yi, G., Teong, S.P., and Zhang, Y. (2016). Base-free conversion of 5-hydroxymethylfurfural to 2,5-furandicarboxylic acid over a Ru/C catalyst. *Green Chem., 18,* 979-983.

Yu, K., Liu, Y., Lei, D., Jiang, Y., Wang, Y., Feng, Y., Lou, L.-L., Liu, S., and Zhou, W. (2018). $M^{3+}O(-Mn^{4+})_2$ Clusters in doped MnO_x catalysts as promoted active sites for the aerobic oxidation of 5-hydroxymethylfurfural. *Catal. Sci. Technol., 8,* 2299-2303.

Yu, L., Chen, H., Wen, Z., Jin, M., Ma, Z., Ma, X., Sang, Y., Chen, M., and Li, Y. (2021). Highly selective oxidation of 5-hydroxymethylfurfural to 2,5-diformylfuran over an α-MnO_2 catalyst. *Catalysis Today., 367,* 9-15.

Yuan, H., Liu, H., Du, J., Liu, K., Wang, T., and Liu, L. (2020). Biocatalytic production of 2,5-furandicarboxylic acid: recent advances and future perspectives. *Appl. Microbiol. Biotechnol., 104,* 527-543.

Zhang, S., Sun, X., Zheng, Z., and Zhang, L. (2018). Nanoscale center-hollowed hexagon $MnCo_2O_4$ spinel catalyzed aerobic oxidation of 5-hydroxymethylfurfural to 2,5-furandicarboxylic acid. *Catal. Comm., 113,* 19-22.

Zhou, C., Deng, W., Wan, X., Zhang, Q., Yang, Y., and Wang, Y. (2015). Functionalized carbon nanotubes for biomass conversion: The base-free aerobic oxidation of 5-hydroxymethylfurfural to 2,5-furandicarboxylic acid over platinum supported on a carbon nanotube catalyst. *ChemCatChem., 7,* 2853-2863.

Zhu, J., Cheng, F., Wang, F., Wen, S., and Liu, X. (2022). Selective oxidation of 5-hydroxymethylfurfural to 2, 5-diformylfuran over a vanadium manganese oxide catalyst. *Catal. Lett., 152,* 2280-2287.
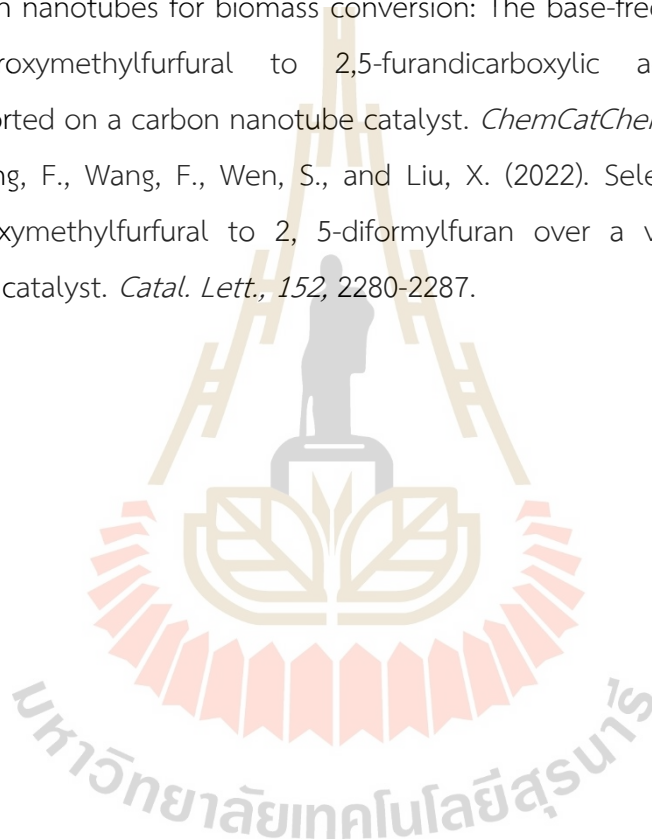
CHAPTER II

LITERATURE REVIEW

2.1 Catalytic reactions of HMF to bio-fuel and bio-chemicals

Catalytic reactions are required to convert biomass to desired platform chemicals and fuels. New efficient catalytic systems, which require less reactions, separation, and purification processes, have been sought to reduce cost in bio-chemical technologies (Wang, Zhu et al., 2019). Various homogeneous and heterogeneous catalytic systems have been explored over the past decades. Heterogeneous catalysts are more practical than homogenous catalysts, because products/catalysts can be easily separated and purified. They are simply recovered and reused, which is good for a large-scale production (Li and Zhang, 2016). Nowadays, development of high efficiency heterogeneous catalysts for HMF conversion is one of challenges in the bio-fuel and bio-chemical industries.

HMF contains many functional groups (that are C=O, C–O, C=C and the furan ring), that can transform to a variety of products via chemical reactions. As shown in **Figure 2.1**, particular derivatives from HMF can be synthesized via different choice of chemical reactions (that are oxidation, hydrogenation, ring opening). Various heterogeneous catalytic materials such as, metals, metal alloys, metal oxides, have been tested for HMF conversion (Davis, Ide et al., 2013, Li, Yang et al., 2016, Kong, Zhu et al., 2018). For instance, vanadium-based oxides (that are V_2O_5, $VOHPO_4$, $(VO)_2P_2O_7$) can convert HMF to maleic anhydride (MA) with up to > 70% yield via oxidation (Li and Zhang, 2016). Not only the type and composition of catalysts and support materials, but experimental conditions, such as pressure, temperature, solvent/medium, and reaction time, also play important roles on the selectivity and efficiency of a catalytic system. Although, tremendous experimental studies and some computational investigations have been done for the catalytic reactions of HMF. Understanding in the molecular level in many parts are still required for

developing highly efficient catalytic systems in practical use. The oxidation of HMF to FDCA is the focus of this work.
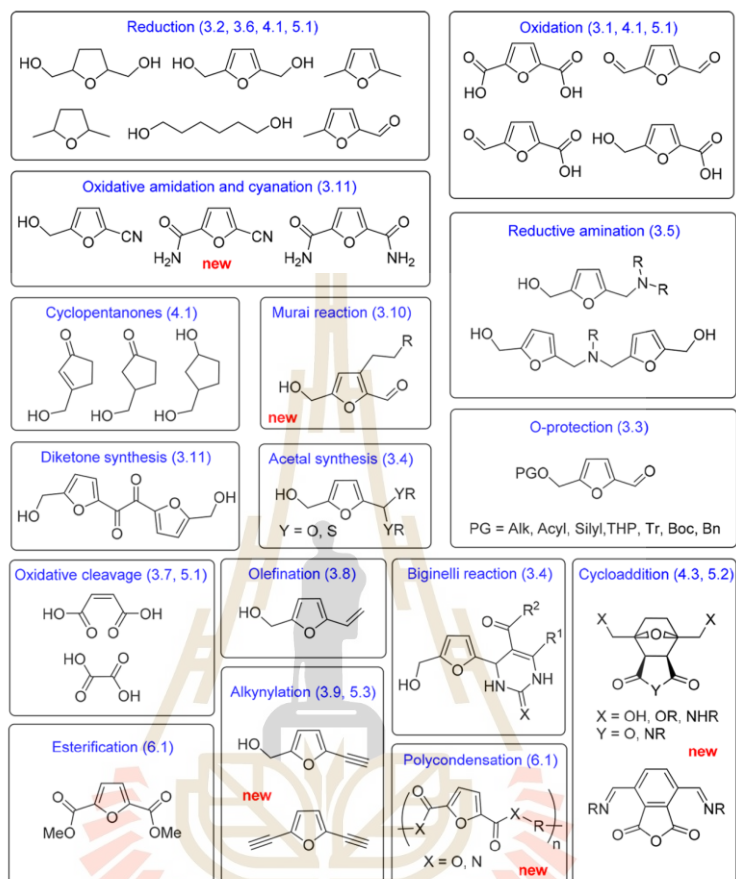
Figure 2.1 Examples of products of main reaction pathways of HMF (Kucherov, Romashov et al., 2018).

2.2 Oxidation of HMF to FDCA

The oxidation of HMF to FDCA can proceed via two pathways as illustrated in **Figure 2.2.** HMF can be oxidized to 5-hydroxymethyl-2-furan carboxylic acid (HMFCA) or 2,5-diformylfuran (DFF) intermediates first, then they will be further oxidized to FFCA and FDCA, respectively. From the literature, efficiency and selectivity of FDCA production from HMF have been tested using numerous heterogeneous catalysts under varied conditions. Examples of this reaction in selected heterogeneous catalytic systems are given in **Table 2.1, 2.2, 2.3, and 2.4.**
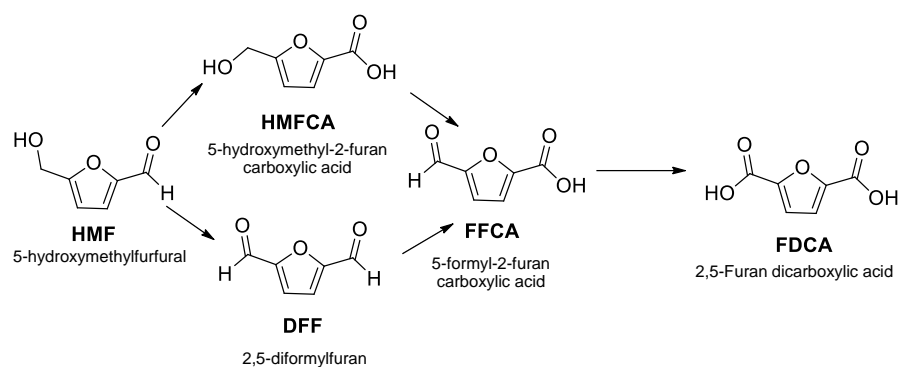
Figure 2.2 Reaction routes of HMF oxidation to FDCA.

Noble metals on many support materials have been used as catalysts for the HMF oxidation as summarized in **Table 2.1**. Those Au, Pd, Pt and Ru-based catalysts produce high yield of FDCA. In **Table 2.1**, Au-based catalysts are high performance catalysts for this reaction as they produce high yields of FDCA up to 99% (Casanova, Iborra et al., 2009, Cai, Ma et al., 2013, Miao, Zhang et al., 2015, Megías-Sayago, Lolli et al., 2019). In the literature, the collaboration between experiment and computational studies has been carried out to understand the oxidation of HMF in noble metal catalyst. From the work of Lei and co-workers, (Lei, Yu et al., 2016) the HMF conversion to FDCA on Pd nanocatalyst was examined using experimental and theoretical approaches. They employed a plane-wave based DFT method to investigate the reaction mechanisms on Pd(100) and Pd(111) facets. They proposed that the oxidation of HMF to FDCA on Pd proceeds through (i) HMF to HMFCA, (ii) HMFCA to FFCA, and (iii) FFCA to FDCA steps, respectively. They reported that the facet and size of synthesized Pd nanocatalysts affect the catalytic performance. The (111) facet on Pd-nanooctahedrons showed better performance than the (100) facet of Pd nanocubes. The potential energy profiles of HMFCA to FFCA clearly show that the energy barriers (E_a) on Pd (111) are lower than those of Pd (100), as depicted in **Figure 2.3**. Their computational and experimental results provide very useful and deep understanding of the facet dependence of HMF oxidation in this noble catalyst.
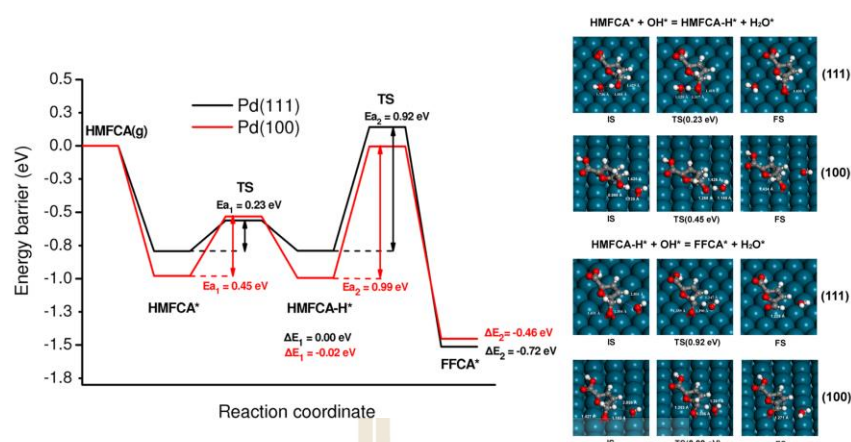
Figure 2.3 Comparison of potential energy profiles of HMFCA to FFCA steps over Pd(111) and Pd(100) surfaces and relevant configurations (Lei, Yu et al., 2016).

In addition, Liu, Y., et al., reported that the active oxygen species promoted catalytic oxidation of HMF on facet specific of Pt nanocrystals, where cubic (Pt-NCs), octahedral (Pt-NOs), and spherical (Pt-NSs) morphologies were synthesized and used as catalysts in oxidation of HMF to FDCA. Through experimental and computational investigations, it was shown that Pt-NCs enclosed by the (100) facets exhibited significantly enhanced catalytic activity compared to Pt-NOs enclosed by the (111) facets and Pt-NSs, for the oxidation of HMF. Through DFT calculations, the different conversion pathways of O_2 on Pt nanocrystals were demonstrated. Molecular O_2 tends to be dissociated to generate the hydroxyl radical ($^•OH$) on a Pt (100) surface but prefers to be reduced to superoxide radical ($^•O_2^-$) on a Pt (111) surface (Liu, Ma et al., 2019).

The potential energy profiles of HMFCA to FFCA clearly show that the activation energies (E_a) on Pt(100) are lower than those in Pt(111). The reaction on Pt (100) is kinetically more favorable than that of the reaction on Pt(111), as depicted in **Figure 2.4**. The result indicates that, the active oxygen species affect the catalytic performance. It can obviously decrease the energy barrier of the O–H bond scission of HMFCA.
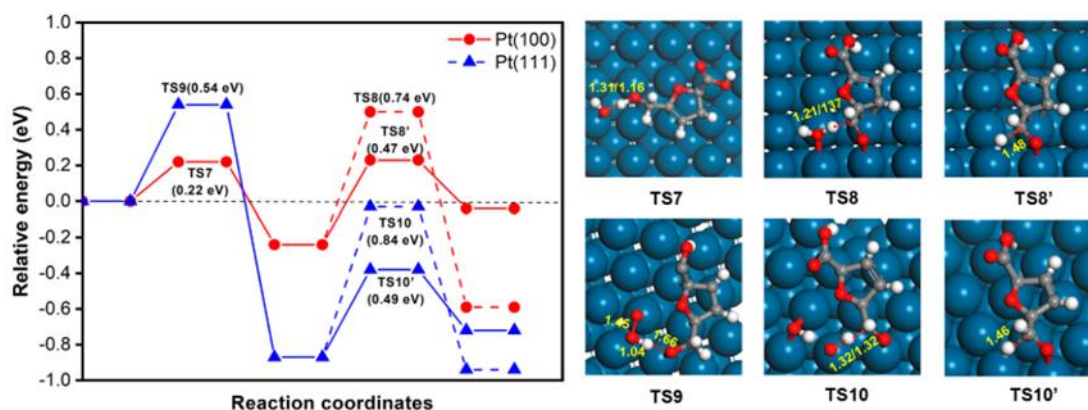
Figure 2.4 Comparison of potential energy profiles of HMFCA to FFCA steps over Pt (111) and Pt (100) surfaces and relevant configurations (Liu, Ma et al., 2019).

Many bi-metal-based catalysts present good performance for oxidizing HMF to FDCA as shown in **Table 2.2**. However, expensive costs of these noble catalysts are the major impediment of using them in the scale-up production. Consequently, non-noble metal heterogeneous catalysts have gained more attention these days. The HMF conversion in many transition metals and their oxides have been examined, as summarized in **Table 2.3**. For instance, Hayashi et al. investigated the oxidation of HMF in many non-noble metal oxides, such as manganese oxides (that are MnO_2, Mn_2O_3, Mn_3O_4, MnO, MnOOH, $SrMnO_3$), iron oxides (that are Fe_2O_3, Fe_3O_4, FeO), cobalt oxides (that are Co_3O_4, CoO), copper oxides (Cu_2O, CuO) and NiO (Eri Hayashi, Tasuku Komanoya et al., 2017). Among those tested metal oxides, MnO_2 showed the highest yield for the oxidation of HMF to FDCA under the condition presented in **Table 2.3**. They claimed that MnO_2 is simply recovered by filtration and re-used (Eri Hayashi, Tasuku Komanoya et al., 2017). For another example, Mn_3O_4, Co_3O_4, and their bimetallic forms were tested for catalytic oxidation of HMF to FDCA by Zhang *et al* (Zhang, Sun et al., 2018). Under the condition shown in **Table 2.3**, $MnCo_2O_4$ can convert HMF to FDCA up to 70.9%, while Mn_3O_4 and Co_3O_4 give lower yield of FDCA. Yan *et al.* synthesized nanobelt-arrayed vanadium oxide hierarchical microspheres to catalyze selective oxidation of HMF to 2,5-diformylfuran (DFF) (Yan, Li et al., 2017). The synthesized catalyst provides high conversion of 93.7% with excellent selectivity of 95.4%. Tong and coworkers (Tong, Yu et al., 2017) have developed a new selective aerobic oxidation of HMF to produce DFF using the Cu-doped MnO_2

catalyst. It was found that 86.0% conversion of HMF and 96.1% selectivity of DFF can be obtained in alcoholic solvent. Han et al. synthesized MnO_x–CeO_2 mixed oxides by a co-precipitation method and used to catalyze the direct aerobic oxidation of HMF to FDCA in the aqueous phase (Han, Li et al., 2017). The results indicate that MnO_x–CeO_2 mixed oxides can convert HMF to FDCA up to 91.0% and it can be reused for five times without much loss of catalytic activity. In addition, Hayashi et al. investigated the HMF oxidation to FDCA on MnO_2-based catalysts. Through a combination of computational and experimental studies, it is suggested that the catalytic activities of HMF oxidation strongly depend on the crystal structure of MnO_2. Computations based on DFT indicate that β-MnO_2 is likely to be a good candidate as oxidation catalysts since it exhibits lower oxygen vacancy formation energies (Hayashi, Yamaguchi et al., 2019).

Recently, Ren et al. reported that CuO and Co_3O_4 catalysts provide the high yield of FDCA production as present in **Table 2.3**. The HMF adsorption energy (E_{ad}) and the hydroxyl (O-H) bond activation on CuO(111) and Co_3O_4(110) surfaces were carried out in this work. The computational insight into the role of the CuO and Co_3O_4 catalysts toward the bond activations of HMF molecule was reported (Ren, Song et al., 2018). The calculated results show that HMF chemically adsorbs on both metal oxide surfaces. The hydroxyl O–H bond breaking is kinetically more favorable than that of the formyl C–H bond and it is likely to be the first step in the HMF oxidation process toward the formation of FDCA as depicted in **Figure 2.5 and 2.6** (Ren, Song et al., 2018).
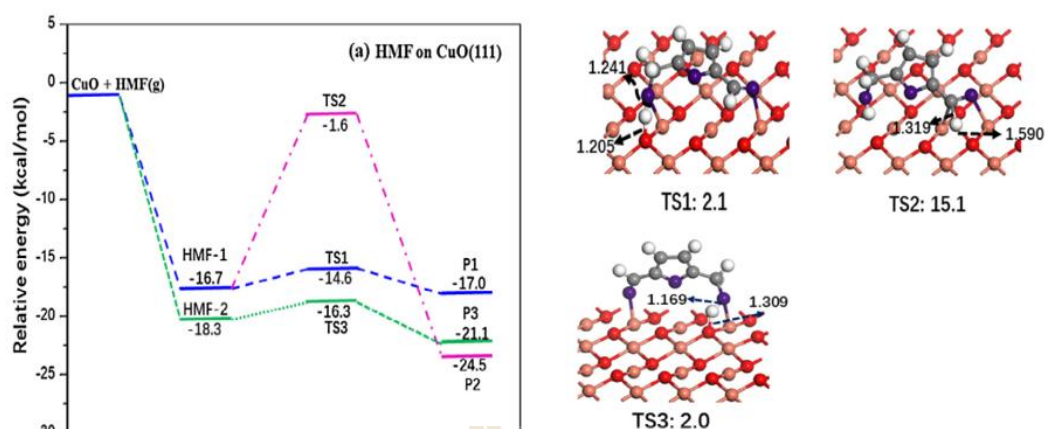
Figure 2.5 Schematic potential energy diagram for the formyl C-H (pink line) and hydroxyl O-H bonds (blue and green line) of HMF scission on CuO(111) (Ren, Song et al., 2018).
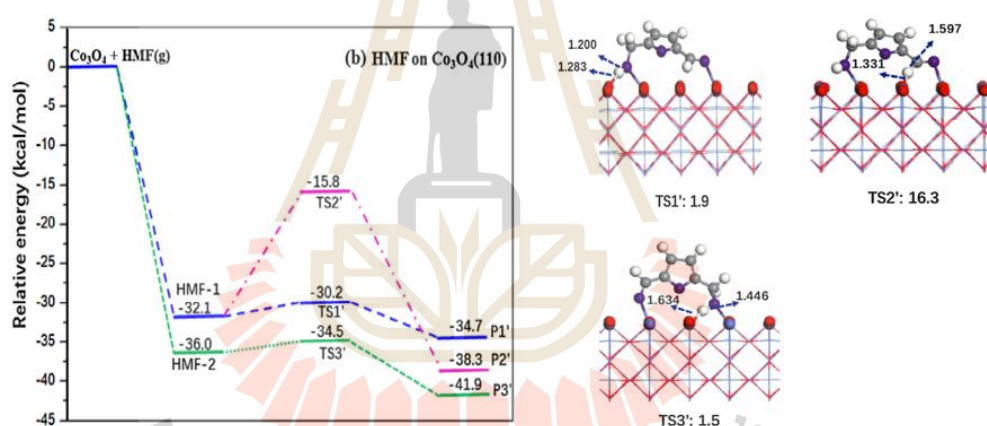
Figure 2.6 Schematic potential energy diagram for the formyl C-H (pink line) and hydroxyl O-H bonds (blue and green line) of HMF scission on Co_2O_4(110) (Ren, Song et al., 2018).

Jiang et al. reported that a Pd-MnO$_2$ catalyst can convert HMF into FDCA with a high yield of 88% in aqueous solution using O$_2$ as an oxidant at ambient pressure (Liao, Hou et al., 2019). They found that Pd-MnO$_2$ showed higher activity in the production of FDCA than its Pd nanoparticle and Pd-based catalysts. In addition, DFT calculations were performed to explain the origin of the high catalytic activity of Pd-MnO$_2$. Computations reveal that Pd-MnO$_2$ possesses lower adsorption energy of HMF (-3.34 eV) than that of the Pd nanoparticle deposited on MnO$_2$ (Pd$_{13}$/MnO$_2$) (-2.79 eV) suggesting strong interaction between HMF and Pd single site on Pd-MnO$_2$, as

depicted in **Figure 2.7**. Experimental and theoretical results suggest that MnO_2-supported atomic Pd have enhanced the catalytic oxidation of HMF to FDCA.
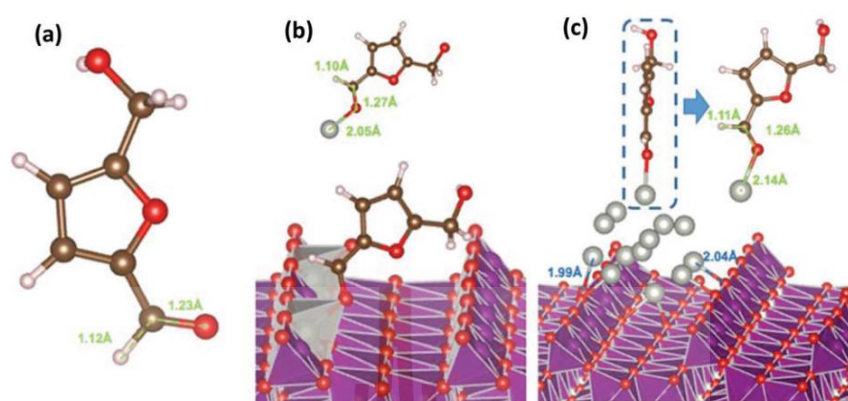
Figure 2.7 Geometric structures of HMF adsorbed onto the activated Pd site supported on the α-MnO_2 (110) surface. (a) Free HMF in vacuum. (b) HMF adsorbed on Pd-MnO_2. (c) HMF adsorbed on Pd_{13}/MnO_2 (Liao, Hou et al., 2019).

Recently, heterostructure manganese catalysts for selective oxidation of HMF to DFF were synthesized including $MnCO_3$, ε-MnO_2, and Mn_2O_3. These catalysts exhibit a high percent selectivity and yield of DFF. The lattice oxygen played a crucial role in the oxidation process, which was confirmed by subjecting the spent catalyst to XPS analysis. Also, they proposed a plausible mechanistic pathway for the transformation of HMF to DFF under O_2 atmosphere, as depicted in **Figure 2.8.** (Pal and Saravanamurugan, 2020).
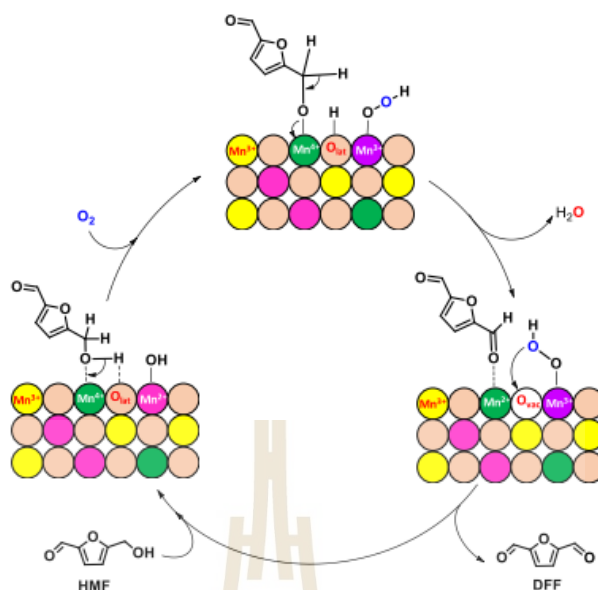
Figure 2.8 Proposed Mechanisms of HMF oxidation to DFF on heterostructure manganese catalysts (Pal and Saravanamurugan, 2020).

2.3 Metals-doped manganese oxide catalysts for HMF oxidation

Catalytic performance of MnO_2 can be further improved by foreign metal doping as summarized in **Table 2.4.** For instance, Hu et al. reported that the Cu doping α-MnO_2 leads to higher catalytic activity of CO oxidation because it reduced the size of α-MnO_2 rods, exposed more (001) surfaces, and increased the surface area. In addition, Cu doping did not change the crystal structure of α-MnO_2 (Hu, Chen et al., 2020). Tong et al. investigated Cu doped MnO_2 catalysts for HMF oxidation to DFF (Tong, Yu et al., 2017). The results showed a 74.8% conversion of HMF, and 50.9% yield of DFF. Also, the increased surface area and the pore volume of Cs/MnO_x after Cs doped MnO_x lead to a high HMF conversion of 98.4% and a high DFF yield of 94.7% at 100 °C under 10 bar oxygen pressure (Yuan, Liu et al., 2018). Ke et al. presented nitrogen-doped manganese oxide (N-MnO_2) catalysts is interesting for HMF oxidation to DFF (Ke, Jin et al., 2019).

Moreover, Liao et al. reported that Pd doped into the crystalline framework of α-MnO_2 can be synthesized by hydrothermal method. The doped catalysts showed higher activity in the production of FDCA (Liao, Hou et al., 2019). **Figure 2.7b** shows a Pd species in Pd-MnO_2 predominantly exist as single atoms and substitute at

Mn sites in the crystalline lattice. The results showed a high 100% conversion of HMF and 88.1% yield of FDCA. Similarly, Pd nanoparticles supported on MnO_2 was prepared using a conventional deposition precipitation method. A computational method has been used to obtain insight into the role of Pd doping toward the improved catalytic activity. A Pd_{13} cluster supported on MnO_2 surface was modeled as an approximation for the Pd nanoparticle deposited on MnO_2 ($PdNP/MnO_2$), as depicted in **Figure 2.7c.** The 100% conversion of HMF and 67.8% yield of FDCA were reported (Liao, Hou et al., 2019). Computations reveal that the stable adsorption configurations of the HMF molecule on $Pd-MnO_2$ and Pd_{13}/MnO_2, as depicted in **Figure 2.7b. and 2.7c.** The adsorption energy of HMF on $Pd-MnO_2$ has a lower than Pd_{13}/MnO_2. This suggests that Pd single site has stronger binding affinity for HMF. The electronic properties of the catalyst were also investigated. **Figure 2.9** show the charge density distribution plot reveals electron transfer from atomic Pd to MnO_2. In addition, the bader charge analysis indicate the Pd single atom lost more electrons than Pd_{13}, which is consistent with the XPS result. Therefore, HMF received more electrons from $Pd-MnO_2$ than from Pd_{13}/MnO_2.
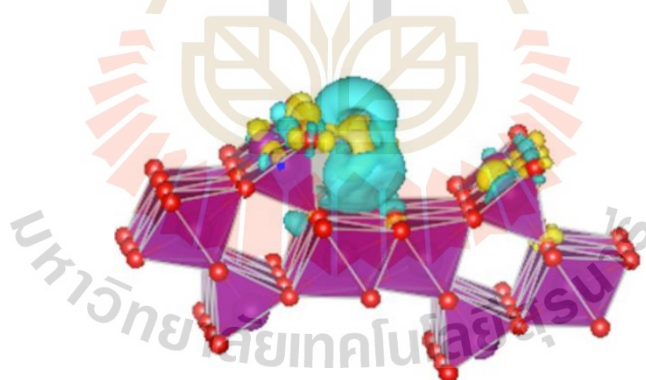
Figure 2.9 The charge density distribution of $Pd-MnO_2$. Mn atom (purple), Pd atom (silver) and O atom (red). The yellow and the blue color represent the accumulation and depletion of electrons, respectively (Liao, Hou et al., 2019).

Until now, the understanding of the oxidation HMF to FDCA in non-noble metal oxides are still scarce. There are large unknown parts that are necessary to explore by experimental and computational approaches. From this literature review, MnO_2-based catalysts show great catalytic performance for the FDCA production. In

addition, different MnO_2 phases have different stability, reactivity and other properties (Kitchaev, Dacek et al., 2017). To the best of our knowledge, there is still lack of deep investigation, especially molecular simulation of the reactions in the MnO_2 based catalysts. To date, the full mechanistic study has not been reported. Therefore, this work applies DFT approaches to investigate the HMF oxidation to FDCA in MnO_2-based catalysts and to gain useful information for developing high efficient heterogeneous catalysts for this application.

Table 2.1 HMF to FDCA in noble metal-based catalysts.

Catalyst	Base	Reaction condition	Solvent	HMF Conv. (%)	FDCA Yield (%)	Ref.
Noble metal-based catalysts						
Au/CeO_2	NaOH (4 equiv.)	10 bar air 65 ℃, 8 h	Water	100	99	(Casanova, Iborra et al., 2009)
$Au/Ce_{0.9}Bi_{0.1}O_{2-\delta}$	NaOH (4 equiv.)	10 bar O_2, 65 ℃, 2 h	Water	100	99	(Miao, Zhang et al., 2015)
Au/HY	NaOH (5 equiv.)	3 bar O_2, 60 ℃, 6 h	Water	>99	99	(Cai, Ma et al., 2013)
Au/Al_2O_3	NaOH (4 equiv.)	10 bar O_2, 70 ℃, 4 h	Water	100	99	(Megías-Sayago, Lolli et al., 2019)
$Pd/KF/Al_2O_3$	NaOH (5 equiv.)	O_2 flow (35 ml/min), 90 ℃, 8 h	Water	>99	91	(Siyo, Schneider et al., 2014)
Pd/HT-5	-	O_2 bubbling, 100 ℃, 8 h	Water	>99	99	(Wang, Yu et al., 2016)
γ-Fe_2O_3@HAP-Pd(0)	K_2CO_3 (0.5 equiv.)	O_2 flow (30 ml/min), 100 ℃, 6 h	Water	97	93	(Zhang, Zhen et al., 2015)
C-Fe_3O_4-Pd	K_2CO_3 (0.5 equiv.)	O_2 flow (20 ml/min), 80 ℃, 4 h	Water	98	92	(Mei, Liu et al., 2015)
Pt/γ-Al_2O_3	pH = 9	0.2 bar O_2, 60 ℃, 6 h	Water	100	99	(Vinke, van Dam et al., 1990)
Pt/C-O-Mg	-	10 bar O_2, 110 ℃, 12 h	Water	99	97	(Ait Rass, Essayem et al., 2015)

Table 2.1 HMF to FDCA in noble metal-based catalysts (Continued).

Catalyst	Base	Reaction condition	Solvent	HMF Conv. (%)	FDCA Yield (%)	Ref.
Noble metal-based catalysts						
Pt/CNT	-	5 bar O_2, 95 ℃, 14 h	Water	100	98	(Zhou, Deng et al., 2015)
Pt/Ce$_{0.8}$Bi$_{0.2}$O$_{2-\delta}$	NaOH (4 equiv.)	10 bar O_2, 23 ℃, 0.5 h	Water	100	98	(Miao, Wu et al., 2015)
Ru/C	-	5 bar O_2, 120 ℃, 10 h	Water	100	88	(Yi, Teong et al., 2016)
Ru/MnCoO$_4$	-	24 bar O_4, 120 ℃, 10 h	Water	100	99	(Mishra, Lee et al., 2017)
Pt	NaHCO$_3$ (0.8 mmol)	72 mL/min O_2, 100 ℃, 10 h	Water	100	95.1	(Liu, Ma et al., 2019)
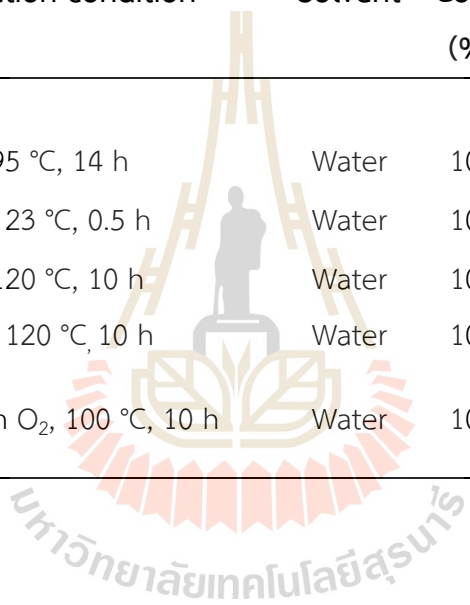
Table 2.2 HMF to FDCA in bimetallic catalysts.

Catalyst	Base	Reaction condition	Solvent	HMF Conv. (%)	FDCA Yield (%)	Ref.
Bimetallic catalysts						
Au-Cu/TiO$_2$ [Au:Cu = 1:1]	NaOH (4 equiv.)	10 bar O$_2$, 95 °C, 4 h	Water	100	99	(Pasini, Piccinini et al., 2011)
Au-Cu/TiO$_2$ [Au:Cu = 3:1]	NaOH (4 equiv.)	10 bar O$_2$, 95 °C, 4 h	Water	100	90	(Albonetti, Pasini et al., 2012)
Au-Pd/CNT	-	10 bar air, 100 °C, 12 h	Water	100	96	(Wan, Zhou et al., 2014)
Au$_8$-Pd$_2$/AC	NaOH (2 equiv.)	3 bar O$_2$,60 °C, 4 h	Water	99	99	(Villa, Schiavoni et al., 2013)
Au-Pd/La-CaMgAl-LDH	-	5 bar O$_2$, 120 °C, 6 h	Water	100	>99	(Gao, Xie et al., 2017)
Pt-Bi/C	Na$_2$CO$_3$ (2 equiv.)	40 bar O$_2$, 100 °C, 6 h	Water	100	99	(Ait Rass, Essayem et al., 2013)
Pt-Bi/TiO$_2$	Na$_2$CO$_3$ (2 equiv.)	40 bar O$_2$,100 °C, 6 h	Water	99	99	(Ait Rass, Essayem et al., 2015)
Pt-Pb/C	NaOH (1.25 M)	1 bar O$_2$, 25 °C, 2 h	Water	100	99	(Verdeguer, Merat et al., 1993)
Ni$_{0.90}$Pd$_{0.10}$	Na$_2$CO$_3$ (1 equiv.)	Air bubbling, 80 °C, 4 h	Water	99	70	(Gupta, Kavita Rai et al., 2017)
Ni$_{0.90}$Pd$_{0.10}$/Mg(OH)$_2$	-	Air bubbling, 100 °C, 10 h	Water	99	78	(Gupta., Rohit K. Singh et al., 2017)

Table 2.3 HMF to FDCA in non-noble metal catalysts.

Catalyst	Base	Reaction condition	Solvent	HMF Conv. (%)	FDCA Yield (%)	Ref.
Non-noble metal catalysts						
FeII-POP-1	-	10 bar air, 100 °C, 10 h	Water	100	79	(Saha, Gupta et al., 2013)
MnO_2	$NaHCO_3$ (3 equiv.)	10 bar O_2, 100 °C, 24	Water	100	91	(Hayashi, Komanoya et al., 2017)
MnO_2	$NaHCO_3$	0.8 MPa O_2, 100 °C, 28 h	Water	100	56.7	(Yu, Liu et al., 2018)
MnO_x	$NaHCO_3$	0.8 MPa O_2, 100 °C, 28 h	Water	100	72.8	(Yu, Liu et al., 2018)
MnO_x-CeO_2	$KHCO_3$ (4 equiv.)	20 bar O_2, 110 °C, 12 h	Water	98	91	(Han, Li et al., 2017)
$Li_2CoMn_3O_8$	-	55 bar O_2, 150 °C, 8 h	AcOH	100	80	(Agarwal, Kailasam et al., 2018)
nano-Fe_3O_4-CoO_x	-	70% t-BuOOH, 80 °C, 12 h	DMSO	97	69	(Kweon, Hwang et al., 2015)
$Fe_{0.6}$-$Zr_{0.4}$-O_2	-	20 bar O_2, 160 °C, 24 h	Water	100	61	(Yan, Xin et al., 2018)
$MnFe_2O_4$	-	t-BuOOH, 100 °C, 5 h	Water	100	85	(Gawade, Nakhate et al., 2018)
$CuO \cdot MnO_2CeO_2$	-	9 bar O_2, 130 °C, 4 h	Water	99	99	(Ventura, Nocito et al., 2018)
Ni-MnO_x	$NaHCO_3$	0.8 MPa O_2, 100 °C, 28 h	Water	100	93.8	(Yu, Liu et al., 2018)
Co–MnO_x	$NaHCO_3$	0.8 MPa O_2, 100 °C, 28 h	Water	100	84.5	(Yu, Liu et al., 2018)
Fe–MnO_x	$NaHCO_3$	0.8 MPa O_2, 100 °C, 28 h	Water	100	78.6	(Yu, Liu et al., 2018)
$MnCo_2O_4$	$KHCO_3$	10 bar O_2, 100 °C, 24 h	Water	99.5	70.9	(Zhang, Sun et al., 2018)

Table 2.3 HMF to FDCA in non-noble metal catalysts (Continued).

Catalyst	Base	Reaction condition	Solvent	HMF Conv. (%)	FDCA Yield (%)	Ref.
Non-noble metal catalysts						
CuO	NaOH	NaClO, 40 ℃, 2 h	Water	100	99.84	(Ren, Song et al., 2018)
Co_3O_4	NaOH	NaClO, 40 ℃, 2 h	Water	100	95.72	(Ren, Song et al., 2018)
β-MnO_2	$NaHCO_3$	1 MPa O_2, 100 ℃, 24 h	Water	100	86	(Yamaguchi, Aono et al., 2020)
CoO_x-MC	K_2CO_3	0.5 bar O_2, 80 ℃, 30 h	Water	98.3	95.3	(Liu, Zhang et al., 2020)
2D Mn_2O_3	$NaHCO_3$	1.4 MPa O_2, 100 ℃, 16 h	-	100	99.5	(Bao, Sun et al., 2020)
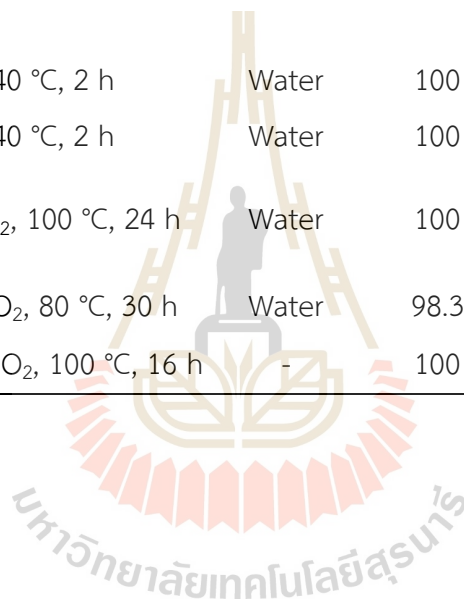
Table 2.4 Metal-doped MnO$_2$ for HMF oxidation reaction.

Catalyst	Base	Reaction condition	Solvent	HMF Conv. (%)	FDCA Yield (%)	Ref.
Metal-Doped on MnO$_2$ for HMF oxidation						
Pd/α-MnO$_2$	K$_2$CO$_3$ (4 equiv.)	O$_2$ flow (25 mL/ min), 100 °C, 4 h	water	100	88.1	(Liao, Hou et al., 2019)
PdNP/(α-MnO$_2$)	K$_2$CO$_3$ (4 equiv.)	O$_2$ flow (25 mL/ min), 100 °C, 4 h	water	100	67.8	(Liao, Hou et al., 2019)
MnO$_2$	-	0.3 MPa O$_2$, 140 °C, 5 h	CH$_3$OH	57.9	4.3	(Tong, Yu et al., 2017)
Cu-MnO$_2$	-	0.3 MPa O$_2$, 140 °C, 5 h	CH$_3$OH	74.8	1	(Tong, Yu et al., 2017)
Cu-MnO$_2$	-	0.3 MPa O$_2$, 140 °C, 5 h	water	30.2	25.5	(Tong, Yu et al., 2017)
Cr-MnO$_2$	-	0.3 MPa O$_2$, 140 °C, 5 h	CH$_3$OH	77.6	6.8	(Tong, Yu et al., 2017)
V-MnO$_2$	-	0.3 MPa O$_2$, 140 °C, 5 h	CH$_3$OH	67.9	1.2	(Tong, Yu et al., 2017)
Mo-MnO$_2$	-	0.3 MPa O$_2$, 140 °C, 5 h	CH$_3$OH	56.1	7.1	(Tong, Yu et al., 2017)

Table 2.4 Metal-doped MnO$_2$ for HMF oxidation reaction (Continued).

Catalyst	Base	Reaction condition	Solvent	HMF Conv. (%)	FDCA Yield (%)	Ref.
Metal-Doped on MnO$_2$ for HMF oxidation						
Mg-MnO$_2$	-	0.3 MPa O$_2$, 140 °C, 5 h	CH$_3$OH	54.5	5.9	(Tong, Yu et al., 2017)
Ca-MnO$_2$	-	0.3 MPa O$_2$, 140 °C, 5 h	CH$_3$OH	51.5	4.6	(Tong, Yu et al., 2017)
Al-MnO$_2$	-	0.3 MPa O$_2$, 140 °C, 5 h	CH$_3$OH	39.5	7.4	(Tong, Yu et al., 2017)
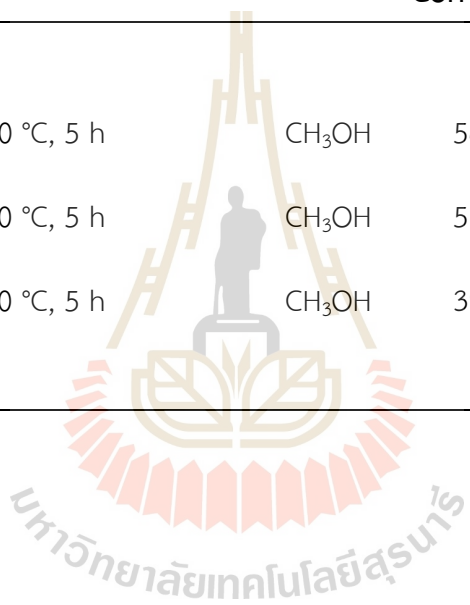
2.4 References

Agarwal, B., Kailasam, K., Sangwan, R.S., and Elumalai, S. (2018). Traversing the history of solid catalysts for heterogeneous synthesis of 5-hydroxymethylfurfural from carbohydrate sugars: A review. *Renew. Sustain. Energy Rev., 82,* 2408-2425.

Ait Rass, H., Essayem, N., and Besson, M. (2013). Selective aqueous phase oxidation of 5-hydroxymethylfurfural to 2,5-furandicarboxylic acid over Pt/C catalysts: influence of the base and effect of bismuth promotion. *Green Chem., 15,* 2240-2251.

Ait Rass, H., Essayem, N., and Besson, M. (2015). Selective aerobic oxidation of 5-HMF into 2,5-furandicarboxylic acid with Pt catalysts supported on TiO_2- and ZrO_2-based supports. *ChemSusChem., 8,* 1206-1217.

Albonetti, S., Pasini, T., Lolli, A., Blosi, M., Piccinini, M., Dimitratos, N., Lopez-Sanchez, J.A., Morgan, D.J., Carley, A.F., Hutchings, G.J., and Cavani, F. (2012). Selective oxidation of 5-hydroxymethyl-2-furfural over TiO2-supported gold–copper catalysts prepared from preformed nanoparticles: Effect of Au/Cu ratio. *Catal. Today, 195,* 120-126.

Bao, L., Sun, F.Z., Zhang, G.Y., and Hu, T.L. (2020). Aerobic Oxidation of 5-Hydroxymethylfurfural to 2,5-furandicarboxylic acid over holey 2D Mn_2O_3 nanoflakes from a Mn-based MOF. *ChemSusChem., 13,* 548-555.

Cai, Ma, H., Zhang, J., Song, Q., Du, Z., Huang, Y., and Xu, J. (2013). Gold nanoclusters confined in a supercage of Y zeolite for aerobic oxidation of HMF under mild conditions. *Chem. Eur. J., 19,* 14215-14223.

Casanova, Iborra, S., and Corma, A. (2009). Biomass into chemicals: Aerobic oxidation of 5-hydroxymethyl-2-furfural into 2,5-furandicarboxylic acid with gold nanoparticle catalysts. *ChemSusChem., 2,* 1138-1144.

Casanova, O., Iborra, S., and Corma, A. (2009). Biomass into Chemicals: Aerobic oxidation of 5-hydroxymethyl-2-furfural into 2,5-furandicarboxylic acid with gold nanoparticle catalysts. *ChemSusChem., 2,* 1138-1144.

Eri Hayashi, Tasuku Komanoya, Keigo Kamata, and Hara., M. (2017). Heterogeneously-catalyzed aerobic oxidation of 5-hydroxymethylfurfural to 2,5-furandicarboxylic acid with MnO_2. *ChemSusChem., 10,* 654-658.

Gao, Z., Xie, R., Fan, G., Yang, L., and Li, F. (2017). Highly efficient and stable bimetallic AuPd over La-doped Ca–Mg–Al layered double hydroxide for base-free aerobic oxidation of 5-hydroxymethylfurfural in water. *ACS Sustain. Chem. Eng., 5,* 5852-5861.

Gawade, A.B., Nakhate, A.V., and Yadav, G.D. (2018). Selective synthesis of 2, 5-furandicarboxylic acid by oxidation of 5-hydroxymethylfurfural over $MnFe_2O_4$ catalyst. *Catal. Today., 309,* 119-125.

Gupta, Kavita Rai, Rohit K. Dwivedi, Ambikesh D. Singh, and K., S. (2017). Catalytic aerial oxidation of biomass-derived furans to furan carboxylic acids in water over bimetallic nickel–palladium alloy nanoparticles. *ChemCatChem., 9,* 2760-2767.

Gupta., K.R., Rohit K. Singh, and K., S. (2017). Catalytic aerial oxidation of 5-hydroxymethyl-2-furfural to furan-2,5-dicarboxylic acid over Ni–Pd nanoparticles supported on $Mg(OH)_2$ nanoflakes for the synthesis of furan diesters. *Inorg. Chem. Front., 4,* 871-880.

Han, X., Li, C., Liu, X., Xia, Q., and Wang, Y. (2017). Selective oxidation of 5-hydroxymethylfurfural to 2,5-furandicarboxylic acid over MnO_x–CeO_2 composite catalysts. *Green Chem., 19,* 996-1004.

Hayashi, Yamaguchi, Y., Kamata, K., Tsunoda, N., Kumagai, Y., Oba, F., and Hara, M. (2019). Effect of MnO_2 crystal structure on aerobic oxidation of 5-hydroxymethylfurfural to 2,5-furandicarboxylic acid. *J. Am. Chem. Soc., 141,* 890-900.

Hayashi, E., Komanoya, T., Kamata, K., and Hara, M. (2017). Heterogeneously-catalyzed aerobic oxidation of 5-hydroxymethylfurfural to 2,5-furandicarboxylic acid with MnO_2. *ChemSusChem., 10,* 654-658.

Hu, X., Chen, J., Li, S., Chen, Y., Qu, W., Ma, Z., and Tang, X. (2020). The promotional effect of copper in catalytic oxidation by Cu-doped α-MnO_2 nanorods. *J. Phys. Chem. C, 124,* 701-708.

Ke, Q., Jin, Y., Ruan, F., Ha, M.N., Li, D., Cui, P., Cao, Y., Wang, H., Wang, T., Nguyen, V.N., Han, X., Wang, X., and Cui, P. (2019). Boosting the activity of catalytic oxidation of 5-hydroxymethylfurfural to 2,5-diformylfuran over nitrogen-doped manganese oxide catalysts. *Green Chem., 21,* 4313-4318.

Kitchaev, D.A., Dacek, S.T., Sun, W., and Ceder, G. (2017). Thermodynamics of phase selection in MnO_2 framework structures through alkali intercalation and hydration. *J. Am. Chem. Soc., 139,* 2672-2681.

Kucherov, F.A., Romashov, L.V., Galkin, K.I., and Ananikov, V.P. (2018). Chemical transformations of biomass-Derived C6-furanic platform chemicals for sustainable energy research, materials science, and synthetic building blocks. *ACS Sustain. Chem. Eng., 6,* 8064-8092.

Kweon, K.E., Hwang, G.S., Kim, J., Kim, S., and Kim, S. (2015). Electron small polarons and their transport in bismuth vanadate: a first principles study. *Phys. Chem. Chem. Phys., 17,* 256-260.

Lei, D., Yu, K., Li, M.-R., Wang, Y., Wang, Q., Liu, T., Liu, P., Lou, L.-L., Wang, G., and Liu, S. (2016). Facet effect of single-crystalline Pd nanocrystals for aerobic oxidation of 5-hydroxymethyl-2-furfural. *ACS Catal., 7,* 421-432.

Li, and Zhang, Y. (2016). The conversion of 5-hydroxymethyl furfural (HMF) to maleic anhydride with vanadium-based heterogeneous catalysts. *Green Chem., 18,* 643-647.

Liao, X., Hou, J., Wang, Y., Zhang, H., Sun, Y., Li, X., Tang, S., Kato, K., Yamauchi, M., and Jiang, Z. (2019). An active, selective, and stable manganese oxide-supported atomic Pd catalyst for aerobic oxidation of 5-hydroxymethylfurfural. *Green Chem., 21,* 4194-4203.

Liu, Ma, H.-Y., Lei, D., Lou, L.-L., Liu, S., Zhou, W., Wang, G.-C., and Yu, K. (2019). Active oxygen species promoted catalytic oxidation of 5-hydroxymethyl-2-furfural on facet-specific Pt nanocrystals. *ACS Catal., 9,* 8306-8315.

Liu, X., Zhang, M., and Li, Z. (2020). CoO_x-MC (MC = Mesoporous Carbon) for Highly efficient oxidation of 5-hydroxymethylfurfural (5-HMF) to 2,5-furandicarboxylic acid (FDCA). *ACS Sustain. Chem. Eng., 8,* 4801-4808.

Megías-Sayago, C., Lolli, A., Ivanova, S., Albonetti, S., Cavani, F., and Odriozola, J.A. (2019). Au/Al$_2$O$_3$ – Efficient catalyst for 5-hydroxymethylfurfural oxidation to 2,5-furandicarboxylic acid. *Catal. Today., 333,* 169-175.

Mei, N., Liu, B., Zheng, J., Lv, K., Tang, D., and Zhang, Z. (2015). A novel magnetic palladium catalyst for the mild aerobic oxidation of 5-hydroxymethylfurfural into 2,5-furandicarboxylic acid in water. *Catal. Sci. Technol., 5,* 3194-3202.

Miao, Wu, T., Li, J., Yi, T., Zhang, Y., and Yang, X. (2015). Aerobic oxidation of 5-hydroxymethylfurfural (HMF) effectively catalyzed by a Ce$_{0.8}$Bi$_{0.2}$O$_2$–δ supported Pt catalyst at room temperature. *RSC Adv., 5,* 19823-19829.

Miao, Zhang, Y., Pan, X., Wu, T., Zhang, B., Li, J., Yi, T., Zhang, Z., and Yang, X. (2015). Superior catalytic performance of Ce$_{1-x}$Bi$_x$O$_2$–δ solid solution and Au/Ce$_{1-x}$Bi$_x$O$_2$–δ for 5-hydroxymethylfurfural conversion in alkaline aqueous solution. *Catal. Sci. Technol., 5,* 1314-1322.

Mishra, D.K., Lee, H.J., Kim, J., Lee, H.-S., Cho, J.K., Suh, Y.-W., Yi, Y., and Kim, Y.J. (2017). MnCo$_2$O$_4$ spinel supported ruthenium catalyst for air-oxidation of HMF to FDCA under aqueous phase and base-free conditions. *Green Chem., 19,* 1619-1623.

Pal, P., and Saravanamurugan, S. (2020). Heterostructured manganese catalysts for the selective oxidation of 5‐hydroxymethylfurfural to 2,5‐diformylfuran. *ChemCatChem., 12,* 2324-2332.

Pasini, T., Piccinini, M., Blosi, M., Bonelli, R., Albonetti, S., Dimitratos, N., Lopez-Sanchez, J.A., Sankar, M., He, Q., Kiely, C.J., Hutchings, G.J., and Cavani, F. (2011). Selective oxidation of 5-hydroxymethyl-2-furfural using supported gold–copper nanoparticles. *Green Chem., 13,* 2091-2099.

Ren, J., Song, K.-h., Li, Z., Wang, Q., Li, J., Wang, Y., Li, D., and Kim, C.K. (2018). Activation of formyl C-H and hydroxyl O-H bonds in HMF by the CuO(111) and Co$_3$O$_4$ (110) surfaces: A DFT study. *Appl. Surf. Sci., 456,* 174-183.

Saha, B., Gupta, D., Abu-Omar, M.M., Modak, A., and Bhaumik, A. (2013). Porphyrin-based porous organic polymer-supported iron(III) catalyst for efficient aerobic oxidation of 5-hydroxymethyl-furfural into 2,5-furandicarboxylic acid. *J. Catal., 299,* 316-320.

Siyo, B., Schneider, M., Radnik, J., Pohl, M.-M., Langer, P., and Steinfeldt, N. (2014). Influence of support on the aerobic oxidation of HMF into FDCA over preformed Pd nanoparticle based materials. *Appl Catal A Gen., 478,* 107-116.

Tong, X., Yu, L., Chen, H., Zhuang, X., Liao, S., and Cui, H. (2017). Highly efficient and selective oxidation of 5-hydroxymethylfurfural by molecular oxygen in the presence of Cu-MnO_2 catalyst. *Catal. Comm., 90,* 91-94.

Ventura, M., Nocito, F., de Giglio, E., Cometa, S., Altomare, A., and Dibenedetto, A. (2018). Tunable mixed oxides based on CeO_2 for the selective aerobic oxidation of 5-(hydroxymethyl)furfural to FDCA in water. *Green Chem., 20,* 3921-3926.

Verdeguer, P., Merat, N., and Gaset, A. (1993). Oxydation catalytique du HMF en acide 2,5-furane dicarboxylique. *J. Mol. Catal., 85,* 327-344.

Villa, A., Schiavoni, M., Campisi, S., Veith, G.M., and Prati, L. (2013). Pd-modified Au on carbon as an effective and durable catalyst for the direct oxidation of HMF to 2,5-furandicarboxylic acid. *ChemSusChem., 6,* 609-612.

Vinke, P., van Dam, H.E., and van Bekkum, H. (1990). Platinum catalyzed oxidation of 5-hydroxymethylfurfural. *Stud. Surf. Sci. Catal. 55,* 147-158.

Wan, X., Zhou, C., Chen, J., Deng, W., Zhang, Q., Yang, Y., and Wang, Y. (2014). Base-free aaerobic oxidation of 5-hydroxymethyl-furfural to 2,5-furandicarboxylic acid in water catalyzed by functionalized carbon nanotube-supported Au–Pd alloy nanoparticles. *ACS Catal., 4,* 2175-2185.

Wang, Yu, K., Lei, D., Si, W., Feng, Y., Lou, L.-L., and Liu, S. (2016). Basicity-tuned hydrotalcite-supported Pd catalysts for aerobic oxidation of 5-hydroxymethyl-2-furfural under mild conditions. *ACS Catal., 4,* 4752-4761.

Wang, Zhu, C., Li, D., Liu, Q., Tan, J., Wang, C., Cai, C., and Ma, L. (2019). Recent advances in catalytic conversion of biomass to 5-hydroxymethylfurfural and 2, 5-dimethylfuran. *Renew. Sustain. Energy Rev., 103,* 227-247.

Yamaguchi, Y., Aono, R., Hayashi, E., Kamata, K., and Hara, M. (2020). Template-free synthesis of mesoporous β-MnO_2 nanoparticles: structure, formation mechanism, and catalytic properties. *ACS Appl. Mater. Interfaces., 12,* 36004-36013.

Yan, Li, K., Zhao, J., Cai, W., Yang, Y., and Lee, J.-M. (2017). Nanobelt-arrayed vanadium oxide hierarchical microspheres as catalysts for selective oxidation of 5-hydroxymethylfurfural toward 2,5-diformylfuran. *Appl. Catal. B Environ., 207,* 358-365.

Yan, D., Xin, J., Zhao, Q., Gao, K., Lu, X., Wang, G., and Zhang, S. (2018). Fe–Zr–O catalyzed base-free aerobic oxidation of 5-HMF to 2,5-FDCA as a bio-based polyester monomer. *Catal. Sci. Technol., 8,* 164-175.

Yi, G., Teong, S.P., and Zhang, Y. (2016). Base-free conversion of 5-hydroxymethylfurfural to 2,5-furandicarboxylic acid over a Ru/C catalyst. *Green Chem., 18,* 979-983.

Yu, K., Liu, Y., Lei, D., Jiang, Y., Wang, Y., Feng, Y., Lou, L.-L., Liu, S., and Zhou, W. (2018). $M^{3+}O(-Mn^{4+})_2$ clusters in doped MnO_x catalysts as promoted active sites for the aerobic oxidation of 5-hydroxymethylfurfural. *Catal. Sci. Technol., 8,* 2299-2303.

Yuan, Z., Liu, B., Zhou, P., Zhang, Z., and Chi, Q. (2018). Aerobic oxidation of biomass-derived 5-hydroxymethylfurfural to 2,5-diformylfuran with cesium-doped manganese dioxide. *Catal. Sci. Technol., 8,* 4430-4439.

Zhang, Sun, X., Zheng, Z., and Zhang, L. (2018). Nanoscale center-hollowed hexagon $MnCo_2O_4$ spinel catalyzed aerobic oxidation of 5-hydroxymethylfurfural to 2,5-furandicarboxylic acid. *Catal. Comm., 113,* 19-22.

Zhang, S., Sun, X., Zheng, Z., and Zhang, L. (2018). Nanoscale center-hollowed hexagon $MnCo_2O_4$ Spinel catalyzed aerobic oxidation of 5-hydroxymethylfurfural to 2,5-furandicarboxylic acid. *Catal. Comm., 113,* 19-22.

Zhang, Z., Zhen, J., Liu, B., Lv, K., and Deng, K. (2015). Selective aerobic oxidation of the biomass-derived precursor 5-hydroxymethylfurfural to 2,5-furandicarboxylic acid under mild conditions over a magnetic palladium nanocatalyst. *Green Chem., 17,* 1308-1317.

Zhou, C., Deng, W., Wan, X., Zhang, Q., Yang, Y., and Wang, Y. (2015). Functionalized carbon nanotubes for biomass conversion: The base-free aerobic oxidation of 5-hydroxymethylfurfural to 2,5-furandicarboxylic acid over platinum supported on a carbon nanotube catalyst. *ChemCatChem., 7,* 2853-2863.

CHAPTER III

FIRST-PRINCIPLES METHODS BASED ON DENSITY FUNCTIONAL

THEORY (DFT) CALCULATION AND MICROKINETIC MODEL

Density functional theory (DFT) is a successful approach to finding solutions to the fundamental equation (the Schrö̈dinger equation) that describes the quantum behavior of atoms and molecules. Currently, there are many fields within the physical sciences and engineering used for understanding and controlling the properties at the level of atoms and molecules. The electronic structure calculation based on DFT calculations has been extensively studied to probe reaction mechanisms on catalyst surfaces because the calculations provide important information such as stabilities, geometries, and reactivities of adsorbed species on the surface. In this chapter, we will first introduce the fundamental equation of quantum mechanics with the Schrödinger equation (section 3.1). Secondly, DFT approach used for the exchange-correlation functional will be explained in section 3.2. Finally, section 3.3 describes the concepts in reaction microkinetic modeling.

3.1 The Schrödinger equation

The fundamental equation upon which the first principle calculations are based is the time-independent Schrödinger equation, which is familiar with is

$$\hat{H}\Psi = E\Psi \tag{3.1}$$

In this equation $\hat{H}$ denotes the Hamiltonian operator, Ψ is a wavefunction, E is the energy of system. The Hamiltonian operator for the many-body system consists of kinetic and potential energy terms, which can be written as

$$\hat{H} = \hat{T} + \hat{V}_{NN} + \hat{V}_{ee} + \hat{V}_{Ne} \tag{3.2}$$

where $\hat{T}$, $\hat{V}_{NN}$, $\hat{V}_{ee}$, and $\hat{V}_{Ne}$ are the kinetic operator, the potential operator of nucleus-nucleus interaction, the potential operator of electron-electron interaction, and the potential operator of nucleus-electrons interaction, respectively. From the equation (3.2), the kinetic energy operator can be described as the following

$$\hat{T} = -\sum_{I=1}^{M} \frac{\hbar^2}{2m_I} \nabla_{R_I}^2 - \sum_{i=1}^{N} \frac{\hbar^2}{2m_e} \nabla_{r_i}^2 \qquad (3.3)$$

where $\hbar = h/2\pi$ (h being the Planck's constant), and m_I is the mass of the partie, m_e is a mass of an electron with N particles in the system. For the potential energy, the first one is the potential operator of nucleus-nucleus interaction

$$\hat{V}_{NN} = \sum_{I>J} \frac{1}{4\pi\varepsilon_0} \frac{Z_I Z_J e^2}{|\vec{R}_I - \vec{R}_J|} \qquad (3.4)$$

where Z_I and Z_J are the atomic number of nuclei I and J, respectively. $\vec{R}_I$ and $\vec{R}_J$ are the position of nucleus I and J, respectively. For the potential operator of electron-electron interaction at positions $\vec{r}_i$ and $\vec{r}_j$, the equation is given by:

$$\hat{V}_{ee} = \sum_{i>j} \frac{1}{4\pi\varepsilon_0} \frac{e^2}{|\vec{r}_i - \vec{r}_j|} \qquad (3.5)$$

For the potential operator of nucleus-electrons interaction, which is the last term in Eq. (3.2), the equation may be represented as follows:

$$\hat{V}_{Ne} = \sum_{I=1}^{M} \sum_{i=1}^{N} \frac{1}{4\pi\varepsilon_0} \frac{Z_I e^2}{|\vec{R}_I - \vec{r}_i|} \qquad (3.6)$$

Although the time-independent Schrödinger equation is simplified, it is still complicated and difficult to solve the exact solution. Since most phenomena in catalysis and surface science involve on electronic effects more than nuclear contributions. In addition, the time scales associated with the motion of electrons and the atomic nuclei are significantly different. Therefore, the Born-Oppenheimer approximation (Born and Oppenheimer, 1927, Cederbaum, 2008, Shim, Hussein et al., 2009, Yu, Fu et al., 2013), which is the nuclear and electronic components separation, may be solved the electronic problem. Therefore, we can reduce the Hamiltonian operator becomes

$$\hat{H} = -\sum_{i=1}^{N} \frac{\hbar^2}{2m_e} \nabla_{r_i}^2 + \hat{V}_{ee} + \hat{V}_{Ne} \qquad (3.7)$$

or

$$\hat{H} = -\sum_{i=1}^{N} \frac{\hbar^2}{2m_e} \nabla_{r_i}^2 + \sum_{i>j} \frac{1}{4\pi\varepsilon_0} \frac{e^2}{|\vec{r}_i - \vec{r}_j|} + \sum_{I=1}^{M} \sum_{i=1}^{N} \frac{1}{4\pi\varepsilon_0} \frac{Z_I e^2}{|\vec{R}_I - \vec{r}_i|} \qquad (3.8)$$

An analytical solution to Eq. (3.1) is not possible for most systems. Therefore, several approximations and simplifying assumptions were further developed. Hartree Fock Self-Consistent Field (HFSCF) approach, and Quantum Monte Carlo methods are used for solving the Schrödinger equation (Jeff Greeley, Jens K. Nørskov et al., 2002). In the HFSCF approach, many-electron wavefunctions (Ψ) are written as a product of one-electron wavefunctions that contain adjustable parameters and the number of one-electron orbitals is equal to the number of electrons in the system.

3.2 Density functional theory

Density functional theory (DFT) is a quantum-mechanical (QM) method, which is basically used in chemistry and physics to calculate the electronic structure of atoms, molecules, and solids. In this theory, the properties of a many-electron system can be determined by using functionals. The main concept of the DFT is the electron density, which expresses the exchange-correlation energy from Hohenberg-Kohn theorems. This concept contributes to obtaining a simpler approximation of the Schrödinger equation than the Hartree-Fock approximation. The electron density can be written in terms of the wavefunction:

$$\rho(\vec{r}) = \sum_i |\psi_i(\vec{r})| \qquad (3.9)$$

where this electron density interaction $\rho(\vec{r})$ does not have the interaction with each other. Although DFT has its roots in the Thomas-Fermi model (Thomas, 1927, Lieb and Simon, 1977) for the electronic structure of materials. In 1964, Hohenberg and Kohn (Hohenberg and Kohn, 1964) proposed the theorems relate to any system

consisting of electrons moving under the influence of an external potential (the so-called Hohenberg–Kohn theorems).

3.2.1 The Hohenberg-Kohn theorems

DFT was first put on a firm theoretical footing by Hohenberg and Kohn in the framework of the two Hohenberg–Kohn theorems. They have proposed two theorems, that identified the character of electron density as an essential factor in the DFT approach, which involved the wavefunction, Hamiltonian, and external energy. The first Hohenberg–Kohn theorem mentioned that the external potential $V_{ext}(\vec{r})$ is determined within a trivial additive constant by a ground-state electron density $\rho(\vec{r})$. For the second Hohenberg–Kohn theorem defines an important property of the function and states that the electron density that minimizes the energy of the overall functional is the true electron density corresponding to the full solutions of the Schrödinger equation. the functional that delivers the ground-state energy of the system $E_0[\rho(\vec{r})]$ that is the functional of electron density can be calculated in terms of the dependent-internal energies $F_{HK}[\rho(\vec{r})]$ and the independent-external potential $E_{ext}[\rho(\vec{r})]$, as follows:

$$E_0[\rho(\vec{r})] = F_{HK}[\rho(\vec{r})] + E_{ext}[\rho(\vec{r})] \qquad (3.10)$$

Where the derivative of the total energy functional depended on $\rho(\vec{r})$ can be considered by variation principle

$$\frac{\delta E_0[\rho(\vec{r})]}{\delta N}\bigg|_{\rho=\rho_0} = 0 \quad \text{when} \quad N = \int \rho(\vec{r})d\vec{r} \qquad (3.11)$$

3.2.2 The Kohn-Sham equation

A useful way to write down the functional described by the Hohenberg–Kohn theorems is in terms of the single-electron wave function. Kohn and Sham (Kohn and Sham, 1965) assumes that each electron in the system moves liberally, where the average potential field is attributed to the interaction between electrons and nuclei in the system. The functional shown in Eq. (3.12) can be written as

$$F_{HK}[\rho(\vec{r})] = T_{non}[\rho(\vec{r})] + E_{ee}[\rho(\vec{r})] + E_{Ne}[\rho(\vec{r})] \qquad (3.12)$$

where $T_{non}[\rho(\vec{r})]$, $E_{ee}[\rho(\vec{r})]$, and $E_{Ne}[\rho(\vec{r})]$ are non-interacting kinetic energy, the energy of two-electron interaction, and the energy of the interaction between an electron and the present nucleus, respectively. The Eq. (3.12) can be written as a function of the electron density as

$$T_{non}[\rho(\vec{r})] = -\sum_{i=1}^{N} \frac{\hbar^2}{2m} \nabla^2$$

$$E_{ee}[\rho(\vec{r})] = \frac{1}{2}\frac{1}{4\pi\varepsilon_0} \iint \frac{\rho(\vec{r}_1)\rho(\vec{r}_2)e^2}{|\vec{r}_1 - \vec{r}_2|} d\vec{r}_1 d\vec{r}_2$$

and

$$E_{Ne}[\rho(\vec{r})] = \frac{1}{4\pi\varepsilon_0} \sum_{I=1}^{N} \frac{\rho(\vec{r})\, Z_I\, e^2}{|\vec{R}_I - \vec{r}|} \tag{3.13}$$

For the last term in the Eq. (3.10), the independent-external potential $E_{ext}[\rho(\vec{r})]$, the equation may be represented as follows:

$$E_{ext}[\rho(\vec{r})] = T_{int}[\rho(\vec{r})] + E_x[\rho(\vec{r})] + E_C[\rho(\vec{r})] \tag{3.14}$$

where $T_{int}[\rho(\vec{r})]$, $E_x[\rho(\vec{r})]$, and $E_C[\rho(\vec{r})]$ are the interacting kinetic energy, the exchange and correlation energy, respectively. In DFT, the external energy does not have an exact uniform, so we call all energy terms of the external energies as the exchange-correlation energy $E_{XC}[\rho(\vec{r})]$. Therefore, the total energy of ground state can be written as

$$E_0[\rho(\vec{r})] = T_{non}[\rho(\vec{r})] + E_{ee}[\rho(\vec{r})] + E_{Ne}[\rho(\vec{r})] + E_{XC}[\rho(\vec{r})] \tag{3.15}$$

In Eq. (3.15), we obtain the potential operator that corresponds to the ground-state total energy (the effective potential operator; $\hat{V}_{eff}[\rho(\vec{r})]$ depended on the electron density). Therefore, we can be written a simplified Schrödinger equation as

$$\left[\frac{\nabla_i^2}{2} + \hat{V}_{eff}[\rho(\vec{r})]\right] \Psi_i^{KS}(\vec{r}) = E_i \Psi_i^{KS}(\vec{r}) \tag{3.16}$$

We can call the Eq. (3.16) as Kohn-Sham equation, where $\Psi_i^{KS}(\vec{r})$ is Kohn-Sham orbital, E_i is the energy as an eigenvalue, corresponding to $\Psi_i^{KS}(\vec{r})$. The equation for the effective potential operator; $\hat{V}_{eff}[\rho(\vec{r})]$ as follows

$$\hat{V}_{eff}[\rho(\vec{r})] = \hat{V}_H[\rho(\vec{r})] + \hat{V}_{ext}[\rho(\vec{r})] + \hat{V}_{XC}[\rho(\vec{r})]$$

$$\hat{V}_{eff}[\rho(\vec{r})] = \frac{1}{2}\int \frac{\rho(\vec{r})}{|\vec{r}-\vec{r}'|}d\vec{r}' - \sum_{I=1}^{N} \frac{Z_I}{|\vec{R}_I-\vec{r}|} + \hat{V}_{XC}[\rho(\vec{r})] \qquad (3.17)$$

where $\hat{V}_H[\rho(\vec{r})]$ is the Hartree potential operator, $\hat{V}_{ext}[\rho(\vec{r})]$ is the external potential operator of the interaction between an electron and nucleus at position $\vec{r}$, and $\hat{V}_{XC}[\rho(\vec{r})]$ is the exchange-correlation potential operator. The exchange-correlation energy can be written as

$$V_{XC}[\rho(\vec{r})] = \frac{\delta E_{XC}[\rho(\vec{r})]}{\delta \rho(\vec{r})} \qquad (3.18)$$

3.2.3 Exchange-correlation functional

The exchange-correlation potential (XC) contains all the interactions including all the quantum mechanical effects which are not considered in the other potentials. The unknown term of the exchange-correlation (XC) operator is the main problem of this theorem. Even though the XC energy is less than 10% of the total energy but it involves identifying materials' properties. There are many attentions to propose the approximation of this functional, e.g., LDA (local density approximation) and GGA (generalized gradient approximation). The local XC energy per electron can be written as the following

$$\varepsilon_{XC}[\rho(\vec{r})] = \frac{1}{2}\int \frac{\rho_{XC}(\vec{r},\vec{r}')}{|\vec{r}-\vec{r}'|}d\vec{r}' \qquad (3.19)$$

Then

$$E_{XC}[\rho(\vec{r})] = \int \rho(\vec{r})\,\varepsilon_{XC}(\vec{r},\rho)d\vec{r} \qquad (3.20)$$

For the LDA, it can be the exact form for homogeneous electron gas. The XC energy of the LDA can be written as

$$E_{XC}^{LDA}[\rho(\vec{r})] = \int \rho(\vec{r})\,\varepsilon_{XC}^{LDA}[\rho(\vec{r})]d\vec{r} \qquad (3.21)$$

The inhomogeneous behavior is the problem of this XC energy functional for applying the real system. Therefore, GGA has been used to correct this inhomogeneous character with the general formula, and regarded the density gradient. The exchange and correlation energy for a GGA functional is formulated by

$$E_{XC}^{GGA}[\rho(\vec{r})] = \int \rho(\vec{r})\,\varepsilon_{XC}^{GGA}[\rho(\vec{r}),\nabla\rho(\vec{r})]d\vec{r} \qquad (3.22)$$

GGA functionals are suitable for weakly bonded systems and also for many other properties, like ground state energies, geometries, and covalent bonds (Santra, Knorr et al., 2010). Currently, there are many different forms of GGA functionals such as PW91 (Perdew and Wang, 1992), PBE (Ernzerhof and Scuseria, 1999, Hammer, Hansen et al., 1999, Wan, Wang et al., 2021). For most of the calculations mentioned in this work, the PBE functional is used.

$$\varepsilon_{XC}^{PBE}[\rho(\vec{r}),\nabla\rho(\vec{r})] = -\frac{3}{4}\left(\frac{3}{\pi}\right)^{\frac{1}{3}}n^{\frac{1}{3}}(\vec{r})F(x) \qquad (3.23)$$

where

$$F(x) = 1 + a - \frac{a}{1+bx^2}, \qquad x = \frac{|\nabla\rho(\vec{r})|}{n^{\frac{4}{3}}(\vec{r})}$$

where a and b are the constant. Eq. (3.23) can be substiuted in Eq. (3.22), so the corresponding XC potential of PBE is

$$V_{XC}^{PBE}[\rho(\vec{r})] = \frac{\delta E_{XC}^{PBE}[\rho(\vec{r})]}{\delta\rho(\vec{r})} \qquad (3.24)$$

3.2.4 Pseudopotential and wavefunction

Pseudopotential is an attempt or replaces the complicated effects of the motion of electrons. The pseudopotential approach is able to manage this problem by classifying electrons into groups, including core electrons and valence. The core electrons are generally the electrons in the inner shells close to the nucleus. Such core electrons stay in deep potential and static under all transitions. Normally, the bond formation and electronic properties involve the valence electrons, so the core electrons are frozen and considered together with the nuclei (frozen-core

approximation). This allows the pseudo-wavefunctions to be described and makes plane-wave basis sets practical to use.

3.2.5 Self-consistent field approach

Self-consistent field (SCF) methods are used to determine the energy of a many-body system in a stationary state. This method aims to identify the lowest-energy arrangement of atoms. **Figure 3.1** shows the flow chart of solving the Kohn-Sham equation.

- Construct the initial electron density $n(r)$ and calculate the exchangecorrelation energy.

- Calculate the effective potential operators to obtain Kohn-Sham Hamiltonian.

- Solve the Kohn-Sham equation (KS) by substituting the effective potential to obtain the Kohn-Sham orbitals and eigenvalues.

- Use the new Kohn-Sham orbitals to calculate the new electron densities.

- This process is kept calculating until self-consistently converging.
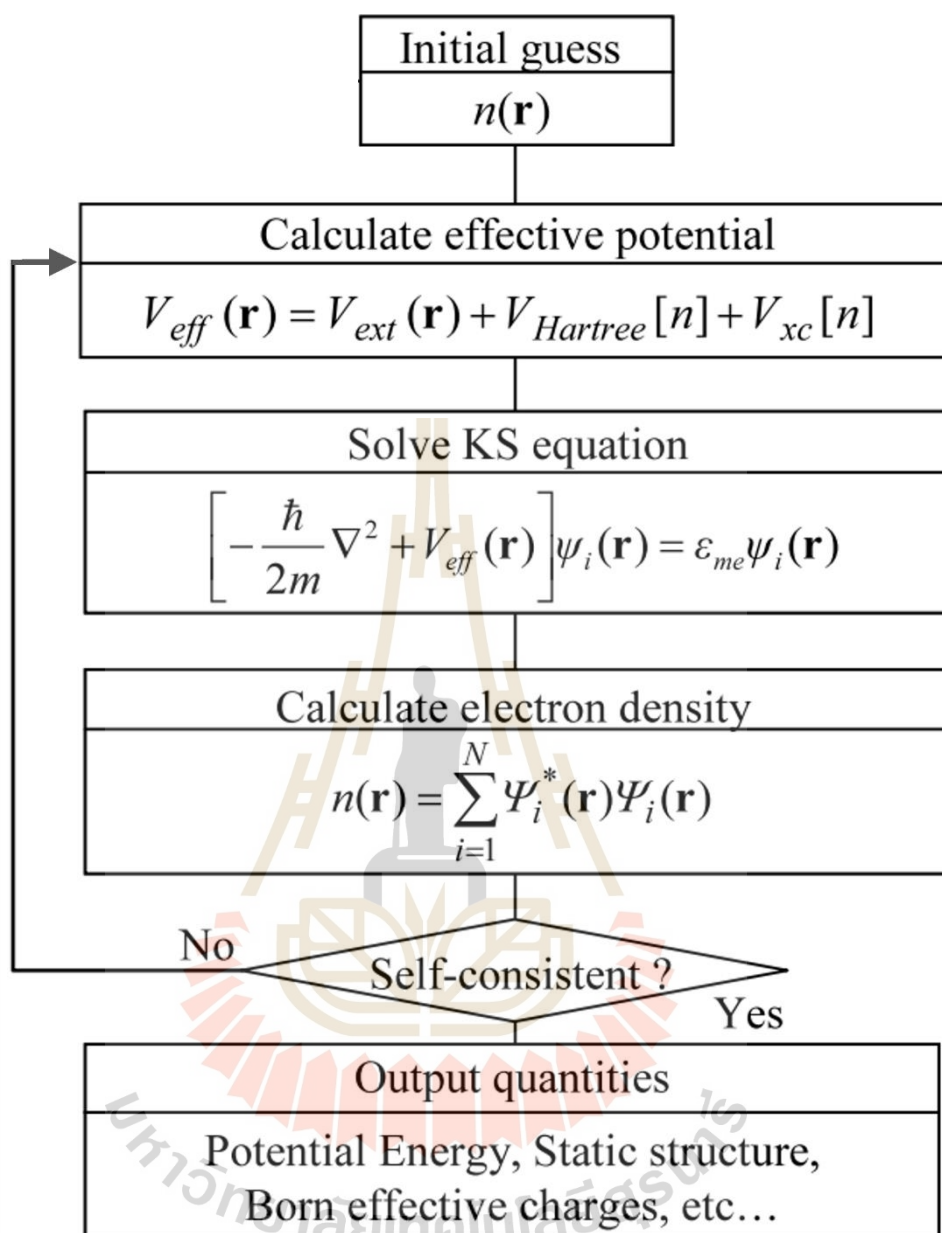
Figure 3.1 Flow chart of solving the Kohn-Sham equation (Modified from (Nakamachi, Uetsuji et al., 2013)).

3.3 Microkinetic modeling

     Microkinetic modeling (Neurock, 1994, Cortright and Dumesic, 2001) was carried out to predict information about surface coverage under reaction conditions and relative rates of various elementary steps. In addition, the microkinetic model is

used to assess whether the rate-determining step (RDS) exists and predict the reaction behavior under a variety of different conditions. In this section, we briefly describe some of the concepts in reaction modeling and show how insights from DFT studies may be used for a better description of a reaction mechanism.
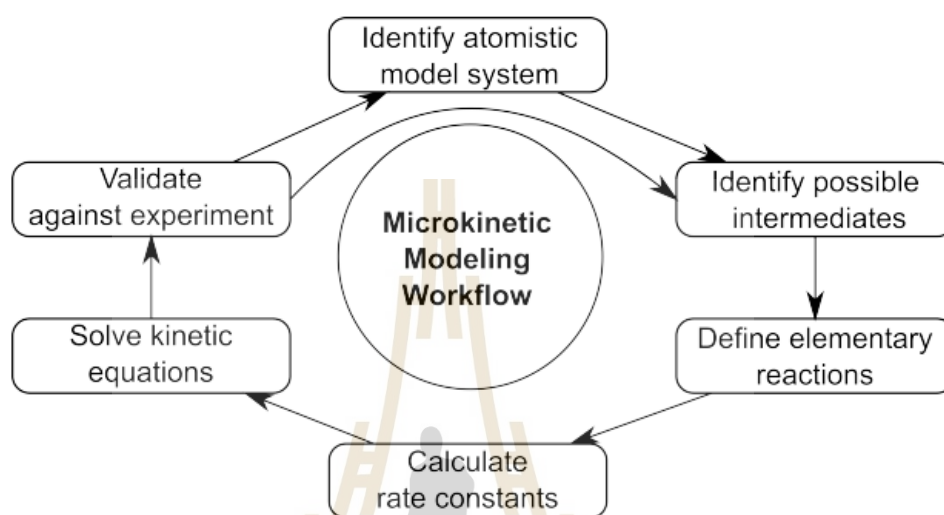
Figure 3.2 Schematic illustration for constructing a first principles microkinetic model.

Figure 3.2 shows the flowchart for the microkinetic model. This thesis begins with identifying an atomic model system of the catalyst β–MnO$_2$ catalyst. The next step is to identify all possible intermediates for HMF oxidation reaction. Then, these intermediates are connected by multiple elementary reaction steps, which together constitute the catalytic cycle. After the intermediates and elementary reactions have been identified, rate constants are calculated for the considered elementary steps and the kinetic equations are solved. For the final step, the computational results are compared to experimental data.

3.3.1 Equilibrium constants

Consider an elementary step A* + B* ⟶ C* + D*, where * denotes a surface species. The equilibrium constant for this elementary step is given as:

$$K = \exp\left(\frac{-\Delta G^o}{k_B T}\right) = exp\left(\frac{-\Delta S^o}{k_B}\right) exp\left(\frac{-\Delta H^o}{k_B T}\right) \qquad (3.25)$$

where k_B is the Boltzmann constant, T is the reaction temperature, and ΔG^o, ΔH^o, and ΔS^o denote the change in standard-state Gibb's free energy, enthalpy and entropy, respectively.

3.3.2 Rate constants

The rate constant for the reactions involving bond-making or bond-breaking is typically calculated using the transition state theory. On the other hand, the steps involving adsorption–desorption phenomena can be used in collision theory for calculating the rate constant.
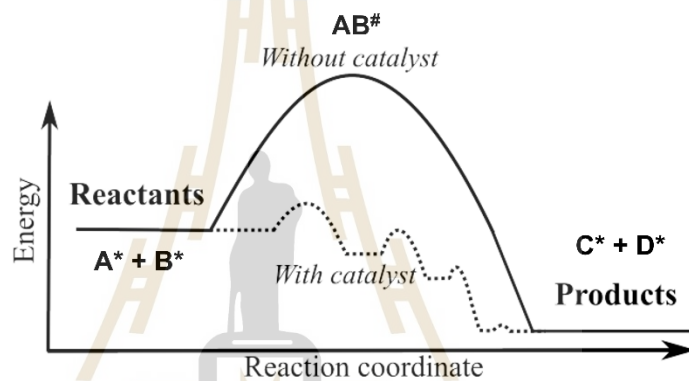
Figure 3.3 schematic illustration of a catalytic reaction.

Figure 3.3 show the reaction of an elementary step A* + B* $\longrightarrow$ C* + D* via transition state (AB#). The reactants are converted to products with lower energies as compared to the case without a catalyst. The conversion of reactants proceeds on the surface of the catalyst, which provides an alternative pathway for the reaction. According to the transition state theory, the elementary reaction may be represented as follows:

$$A^* + B^* \rightleftharpoons AB^\# \rightleftharpoons C^* + D^*$$

The rate of the reaction for this element step may now be given as

$$r = r_f - r_r = k_{for}\theta_A\theta_B - k_{rev}\theta_C\theta_D \qquad (3.26)$$

where r_f and r_r denote the rate of the forward and reverse reaction and θ_A, θ_B, θ_C and θ_D denote the surface coverages of the species A, B, C and D, respectively. k_{for}

and k_{rev} are the forward and the reverse rate constants. the equilibrium constant K are linked through the following relation:

$$K = \frac{k_{for}}{k_{rev}} \tag{3.27}$$

The forward rate constant rate constant k_{for} is given as:

$$k_{for} = A_o \exp\left(\frac{-E_f}{k_B T}\right) \tag{3.28}$$

where E_f is the activation energy for the forward reaction and A_o is the frequency factor. The frequency factor is given as:

$$A_o = \frac{k_b T}{h} \exp\left(\frac{-\Delta S_{for}^{o\#}}{k_B}\right) \tag{3.29}$$

where $\Delta S_{for}^{o\#} = S_{AB^\#}^o - (S_{A^*}^o + S_{B^*}^o)$, is the standard state entropy change accompanying the formation of the transition state $AB^\#$. For the adsorption processes, collision theory may be used to define rate constants as follows:

$$k_{ads} = \frac{\sigma^o(T,\theta) P_A}{\sqrt{2\pi m_A k_B T}} \exp\left(\frac{-E_f}{k_B T}\right) \tag{3.30}$$

where k_{ads} is the rate constant for adsorption processes, P_A is the partial pressure of the adsorbing species in the gas phase, m_A is the molecular weight of the species. $\sigma^o(T,\theta)$ denotes the sticking probability, which is a function of temperature T and coverage θ. Often, the adsorption processes are non-activated, i.e. the activation energy term E_f in Eq. (3.30) is zero. The rate constant in Eq. (3.30) is in units of molecules per unit surface area per time. To calculate turnover frequencies (TOF), the above rates are multiplied by the area occupied by an active site (typically 10^{-15} cm^2).

3.3.3 Gibbs free energy (G) calculation

Gibbs free energy (G) can be divided into enthalpy (H) and entropy (S) by

$$G = E_{elec} + E_{ZPE} - TS \tag{3.31}$$

All electronic energies, E_{elec}, are corrected by zero-point energy (ZPE).

$$ZPE = \sum_i \frac{hv_i}{2} \tag{3.32}$$

where, h is the Planck constant and v_i is the computed real frequencies of the system. The entropy (S) can be calculated as follows:

$$S = k_B lnQ \tag{3.33}$$

Q is the product of the partition function from the following equations.

$$Q = f_{trans}\, f_{vib} f_{rot} \tag{3.34}$$

where f_{trans}, f_{vib} and f_{rot} are the translational, vibrational, and rotational, respectively.

3.3.4 Partition functions

In Eq. (3.33) to calculate entropy, the partition function of an ideal-gas molecule can be split up into translations, rotation, and vibrations (Eq. 3.34). The translational part of the partition function of the free-gas molecule is given by

$$f_{trans} = V\left(\frac{2\pi M k_b T}{h^2}\right)^{3/2} \tag{3.35}$$

where V is the volume of the gas, and M is the mass. V is often substituted for the pressure using the ideal gas equation of state $PV = k_B T$. Note that Eq. (3.35) covers the full three-dimensional partition function, however, it is convenient to use translational partition function for a single dimension. In that case, the equation reduces to:

$$f_{trans} = \frac{L\sqrt{2\pi m k_b T}}{h} \tag{3.36}$$

The rotational partition function can be calculated in the rigid-rotor approximation:

$$f_{rot} = \frac{8\pi^2 I k_b T}{h^2} \tag{3.37}$$

Where I is the moment of inertia about an axis perpendicular to the molecular axis passing through the center of mass of the molecule. Eq. (3.37) is the rotational partition-function for a diatomic molecule. Finally, the vibrational partition function in the Harmonic Approximation has the following form:

$$f_{vib} = \frac{1}{1 - e^{-h\omega/k_b T}} \qquad (3.38)$$

3.3.5 Rate controlling steps and apparent activation energies

The degree of rate control ($X_{RC,i}$) for elementary step i and the thermodynamic rate control ($X_{TRC,n}$) as introduced by Campbell et al. (Campbell, 2017) was used to identify the rate-controlling step and key intermediates. Campbell has suggested the kinetic importance of a particular step in a chemical reaction, which is ascertaining and computing the relative energy change in the overall reaction rate upon changing the forward and reverse rate constants for that step. The degree of rate control ($X_{RC, i}$) for elementary step i is calculated by the equation as follows:

$$X_{RC,i} = \frac{k_i}{r}\left(\frac{\partial r}{\partial k_i}\right)_{k_{j \neq i}, K_i} = \left(\frac{\partial \ln r}{\partial \ln k_i}\right)_{k_{j \neq i}, K_i} \qquad (3.39)$$

where r is the net reaction rate of the elementary step, and k_i is the rate constant. Similarly, the degree of thermodynamic rate control of an intermediate, n, was calculated from

$$X_{TRC,n} = \frac{1}{r}\left(\frac{r}{\left(\frac{-G_n^0}{RT}\right)}\right)_{G_{m \neq n}^0, G_i^0 TS} \qquad (3.40)$$

where the Gibbs free energy of all other intermediates (m ≠ n) and all transition states (i) are held constant. The numeric values of X_{RC} and X_{TRC} represent the degree of influence of the transition state and intermediates on the overall reactions — the larger value indicates the greater the impact. The range of these values is between 0 and 1. The positive and negative values refer to X_{RC} and X_{TRC}, respectively. For the apparent activation energies, the equation is represented as follows:

$$E_{app} = RT^2 \left(\frac{d\, lnr_{overall}}{dT} \right)_{P,yi} \qquad (3.41)$$

where yi stands for the mole fraction of the species i in the reaction mixture.

3.4 References

Born, M., and Oppenheimer, R. (1927). Zur Quantentheorie der Molekeln. *Ann. Phys., 389,* 457-484.

Campbell, C.T. (2017). The degree of rate control: A powerful tool for catalysis research. *ACS Catal., 7,* 2770-2779.

Cederbaum, L.S. (2008). Born–Oppenheimer approximation and beyond for time-dependent electronic processes. *J. Chem. Phys., 128.*

Cortright, R.D., and Dumesic, J.A. (2001). Kinetics of heterogeneous catalytic reactions: Analysis of reaction schemes. *Adv. Catal., 46,* 161-264.

Ernzerhof, M., and Scuseria, G.E. (1999). Assessment of the Perdew–Burke–Ernzerhof exchange-correlation functional. *J. Chem. Phys., 110,* 5029-5036.

Hammer, B., Hansen, L.B., and Nørskov, J.K. (1999). Improved adsorption energetics within density-functional theory using revised Perdew-Burke-Ernzerhof functionals. *Phys. Rev. B., 59,* 7413-7421.

Hohenberg, P., and Kohn, W. (1964). Inhomogeneous electron gas. *Phys. Rev., 136,* B864-B871.

Jeff Greeley, Jens K. Nørskov, and Mavrikakis, M. (2002). Electronic structure and AND catalysis on metal surfaces. *Annu. Rev. Phys. Chem., 53,* 319-348.

Kohn, W., and Sham, L.J. (1965). Self-consistent equations including exchange and correlation effects. *Phys. Rev., 140,* A1133-A1138.

Lieb, E.H., and Simon, B. (1977). The thomas-fermi theory of atoms, molecules and solids. *Adv. Math., 23,* 22-116.

Nakamachi, E., Uetsuji, Y., Kuramae, H., Tsuchiya, K., and Hwang, H. (2013). Process crystallographic simulation for biocompatible piezoelectric material design and generation. *Arch. Comput. Methods Eng., 20,* 155-183.

Neurock, M. (1994). The microkinetics of heterogeneous catalysis. By J.A., Dumesic, D.F., Rudd, L.M., Aparicio, J.E., Rekoske, and A.A., Treviño, ACS Professional

Reference Book, American Chemical Society, Washington, DC, 1993, 315 pp. *AIChE J., 40,* 1085-1087.

Perdew, J.P., and Wang, Y. (1992). Accurate and simple analytic representation of the electron-gas correlation energy. *Phys. Rev. B Condens. Matter., 45,* 13244-13249.

Santra, B., Knorr, A., Scheffler, M., and Michaelides, A. (2010). Density-functional theory exchange-correlation functionals for hydrogen bonds in water. PhD thesis. technische Universität Berlin.

Shim, J.-B., Hussein, M.S., and Hentschel, M. (2009). Numerical test of Born–Oppenheimer approximation in chaotic systems. *Phys. Lett. A., 373,* 3536-3540.

Thomas, L.H. (1927). The calculation of atomic fields. *Math. Proc. Camb. Philos. Soc., 23,* 542-548.

Wan, Z., Wang, Q.-D., Liu, D., and Liang, J. (2021). Effectively improving the accuracy of PBE functional in calculating the solid band gap via machine learning. *Comput. Mater. Sci., 198,* 110699.

Yu, C., Fu, N., Dai, C., Wang, H., Zhang, G., and Yao, J. (2013). Time-dependent Born–Oppenheimer approximation approach for Schrödinger equation: Application to H_2^+. *Opt. Commun., 300,* 199-203.

CHAPTER IV

ROLES OF HYDROXYL AND SURFACE OXYGEN SPECIES ON THE AEROBIC OXIDATION OF 5-HYDROXYMETHYLFURFURAL TO 2,5-FURANDICARBOXYLIC ACID ON BETA-MANGANESE DIOXIDE CATALYSTS: A DFT, MICROKINETIC AND EXPERIMENTAL STUDIES

4.1 Introduction to HMF oxidation in MnO_2 and its significance

5-hydroxymethylfurfural (HMF), a versatile platform chemical derived from biomass, has been used as a precursor for synthesizing a variety of bio-chemicals, bio-fuels (van Putten, van der Waal et al., 2013), and value-added products (Tong, Ma et al., 2010, Yuan, Liu et al., 2020). 2,5-furandicarboxylic acid (FDCA) is one of the most attractive compounds derived from an aerobic oxidation of HMF. It is a monomer of polyethylene 2,5-furandicarboxylate (PEF), the well-known green polymers for replacing the oil derivative polyethylene terephthalate (PET) (Sajid, Zhao et al., 2018, Yang, Xu et al., 2021). The thermochemical HMF oxidation via the heterogeneous catalysis has potential for the large-scale FDCA production due to its less required steps for catalyst recovery and regeneration compared to the homogeneous catalysis. Until now, there are still many challenges for scaling up the FDCA production including development of highly efficient catalysts (Sajid, Zhao et al., 2018, Deshan, Atanda et al., 2020, Yang, Xu et al., 2021). Noble metal-based heterogeneous catalysts such as Au, (Casanova, Iborra et al., 2009, Cai, Ma et al., 2013, Megías-Sayago, Lolli et al., 2019) Pt, (Ait Rass, Essayem et al., 2013, Ait Rass, Essayem et al., 2015, Miao, Wu et al., 2015, Liu, Ma et al., 2019) Pd (Zhou, Deng et al., 2015, Wang, Yu et al., 2016), Ru(Yi, Teong et al., 2016) and their bi-metallic forms (i.e. Au-Pd (Villa, Schiavoni et al., 2013), Au-Cu (Pasini, Piccinini et al., 2011), Ag-Pd (Jin, Sarina et al., 2022), Pt-Au (Zhong, Yuan et al., 2022)) provided the high yield of FDCA (≥ 90 %), albeit their expensive prices are the major drawback for using in mass FDCA

production. Therefore, cheaper metal oxide catalysts such as MnO_2 (Saha, Gupta et al., 2013, Hayashi, Komanoya et al., 2017, Tong, Yu et al., 2017, Yu, Liu et al., 2018, Yamaguchi, Aono et al., 2020), CuO (Ren, Song et al., 2018), Co_3O_4 (Ren, Song et al., 2018), and $MnFe_2O_4$ (Zhang, Sun et al., 2018) have been developed and tested for this reaction. Among them, β-MnO_2 is one of the promising candidates having good catalytic activity, good stability, and good recyclability (Hayashi, Komanoya et al., 2017, Hayashi, Oba et al., 2019, Aono, Hayashi et al., 2020, Cheng, Guo et al., 2021).

For the HMF oxidation reaction ($2C_6H_6O_3 + 3O_2 \longrightarrow 2C_6H_4O_5 + 2H_2O$), HMF is oxidized to 5-formyl-2-furan carboxylic acid (FFCA) via 5-hydroxymethyl-2-furan carboxylic acid (HMFCA) or 2,5-diformylfuran (DFF) intermediates before further oxidizing to FDCA as a final product. Due to the complicated pathways, the full mechanism and the insight into the high catalytic performance, which are decisive for rational design highly efficient catalysts, are still limited. In experiment, DFF has been found as a key intermediate in the HMF-to-FFCA step (Gawade, Nakhate et al., 2018, Lin, Oh et al., 2021, Yu, Chen et al., 2021, Zhu, Cheng et al., 2022), and the FFCA to FDCA step is proposed as a rate determining step over Mn oxide and other oxide catalysts (Hayashi, Oba et al., 2019, Pal, Kumar et al., 2020, Wang, Lai et al., 2022). Most theoretical work focused on the FFCA to FDCA step or the oxygen vacancy formation in metal oxide-based catalysts (i.e. MnO_2, CuO_2 and Co_3O_4) (Ren, Song et al., 2018, Hayashi, Oba et al., 2019). Theoretical studies proposed that the low oxygen vacancy formation energy was proposed as the key factor beyond the higher catalytic performance of β-MnO_2 compared to other MnO_2 allotropes (Hayashi, Oba et al., 2019, Yao and Wang, 2021). The active lattice oxygen on the catalyst surface promotes the catalytic performance of MnO_2 by assisting the activation of C–H and O–H of intermediates (Yao and Wang, 2021).

To the best of our knowledge, many studies focus on the effect of lattice oxygen or superoxide species, however theoretical studies consider the effect of a hydroxyl group (OH), another possible active oxygen species on metal oxide-based catalysts, are scarce. Typically, a hydroxyl group is easily formed via hydroxylation or adding OH source to active metal oxides. In literature, some theoretical studies proposed that not only superoxide species, but hydroxyl group also plays a crucial

role in the HMF-to-FDCA reaction in metal catalysts such as Pt, Pt and Au (Davis, Zope et al., 2012, Liu, Ma et al., 2019, Chen, Wang et al., 2021). Likewise, hydroxide ions (OH⁻) from dissociated H_2O were suggested to play a significant role in the nucleophilic addition of OH– to the carbonyl group for this reaction in $Co_3O_4/Mn_{0.2}Co$ (Gao, Yin et al., 2020). The high acidity of the $Co_3O_4/Mn_{0.2}Co$ catalyst leads to the strong adsorption of HMF, including enhanced ability to form the carboxylic acid group of intermediate and FDCA. The experiment suggested that the availability of both Brønsted and Lewis acid sites on metal oxide surfaces is essential to achieve the high yield of FDCA (Mishra, Lee et al., 2017, Gao, Yin et al., 2020). However, clear explanation about the OH effect has not been investigated by theoretical study.

Herein, great catalytic performance of our synthesized MnO_2 was attested via retained high yield, greater than 85 mol% FDCA, in continuous flow. The role of hydroxyl group on the HMF oxidation in MnO_2 was assured by (i) comparing mechanism and kinetic properties between the non-hydroxylated and hydroxylated surfaces by plane-wave based density functional theory calculation (DFT) and microkinetic modeling and (ii) comparing reactions in water and dimethyl sulfoxide (DMSO) by experiment. Computational and experimental results successfully prove that both active surface oxygen and OH promote the aerobic oxidation of HMF to FDCA in β–MnO_2. This insight is necessary for development and design high performance metal oxide-based catalysts for this reaction.

4.2 Computational and experimental methods

4.2.1 Density Functional Theory

A planewave-based density functional theory (DFT) (Kohn and Sham, 1965) implemented in Vienna ab initio simulation package (VASP 5.4.4) was employed in this work (Kresse and Furthmüller, 1996, Kresse and Furthmüller, 1996). All electronic structure calculations used the Perdew-Burke-Ernzernhof functional (PBE) form of the generalized gradient approximation (GGA) (Perdew, Burke et al., 1996). The ultra-soft pseudopotential with projector augmented wave (PAW) method (Blöchl, 1994, Kresse and Joubert, 1999) was used to describe the nuclei and core electronic states. The

cutoff value for plane wave basis set was set to 500 eV. Van der Waals dispersion correction was applied using the DFT-D3 method as proposed by Grimme et al. (Grimme, Antony et al., 2010). The k-point grid of 2×2×1 was generated using the Monkhorst-Pack scheme (Monkhorst and Pack, 1976) for β–MnO_2(110). The convergence of electronic energy and force on each atom were set to 10^{-6} eV and 0.02 eV/Å and, respectively. For describing the strongly correlated d electrons of Mn in β–MnO_2, the DFT+U approach was used with a Hubbard-like terms U = 2.8 eV and J = 1.2 eV for Mn 3d electron, as suggested by Mellan, T. A., et al. (Liechtenstein, Anisimov et al., 1995, Mellan, Maenetja et al., 2013, Song, Yan et al., 2018). In this work, an antiferromagnetic state was used for the β–MnO_2 model as observed by previous work (Paik, Osegovic et al., 2001, Sato, Wakiya et al., 2001). The climbing image nudged elastic band (CINEB), (Smidstrup, Pedersen et al., 2014) and DIMER methods (Henkelman and Jónsson, 1999, Henkelman and Jónsson, 2001, Olsen, Kroes et al., 2004) were employed for finding the transition state (TS).

4.2.2 Surface model

The Mn $3d^64s^1$, O $2s^22p^4$, C $2s^22p^2$, and H $1s^1$ were treated as valence electrons. All gas-phase simulations were calculated in a cubic box of 15×15×15 Å³. A bulk structure of the rutile-type β–MnO_2 was optimized by the k-point grid of 7×7×11. A 4×2 β-MnO_2(110) slab with dimensions of 11.48 Å× 12.43 Å × 23.09 Å was cleaved from the optimized bulk structure. Three β–MnO_2 layers consisting of 48 Mn atoms and 96 O atoms were separated by 15 Å of vacuum region along the z-axis to avoid interactions between periodic images **(Figure 4.1a, 4.2b)**. The bottom layer was fixed to their bulk lattice positions, whereas the two top layers and adsorbed species were allowed to fully relax during the calculations. The possible active sites of the β–MnO_2(110) slab are atop site of four-fold-coordinate Mn (top-Mn_{4c}), atop site of five-fold-coordinate (top-Mn_{5c}), bridge site between two four-fold-coordinate Mn atoms (bridge-Mn_{4c}), and atop site of three-fold-coordinate O (top-O_{3c}) as presented in **Figure 4.1c**.
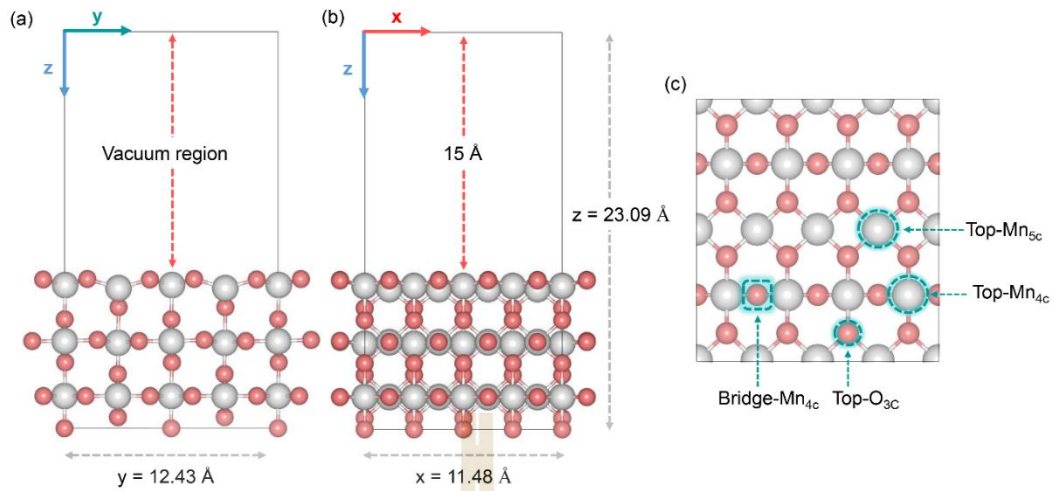
Figure 4.1 Structure of the β–MnO$_2$(110) slab projected along (a) the (010) direction (b) (100) the direction, and (c) possible active sites on the β–MnO$_2$(110) surface.

4.2.3 Microkinetic analysis

Microkinetic modeling was carried out to calculate reaction rate, apparent activation energies and identify rate-limiting steps. **Table 4.1** shows all the elementary steps for HMF oxidation reaction considered in this work. The transition state theory (TST) was used to calculate the rate constants for each elementary step i. The rate constant is calculated by the following equation:

$$k_i = \frac{k_B T}{h} \, e^{-\Delta G_i^{\neq}/k_B T} = A^{\circ} exp^{-\Delta H^{\neq}/k_b T} \qquad (4.1)$$

where k_B is the Boltzmann constant, h is Planck's constant, T is the temperature, and $\Delta G_i^{\neq}$ and $\Delta H^{\neq}$ are the change of Gibbs free energies and enthalpy between the TS and the initial state for step i, respectively. A° refers to the pre-exponential factor.

For an adsorption process, the rate constant of adsorption (or desorption) of X, X + * ⟶ X*, can be calculated using the collision theory.

$$k_{ads} = \frac{10^5}{\sqrt{2\pi m k_B T}} \, A \qquad (4.2)$$

where A is the area of the surface, which is equal to 1.43×10^{-18} m^2 in this work. m is the molecular mass of the adsorbed species X. The desorption rate constant (k$_{des}$) was obtained from the relation $K = k_{ads}/k_{des}$, where K is the equilibrium constant and

forward rate constants, respectively. Gibbs free energy (G) can be divided into enthalpy (H) and entropy (S) by

$$G = E_{elec} + E_{ZPE} - TS \qquad (4.3)$$

All electronic energies, E_{elec}, are corrected by zero-point energy (ZPE).

$$ZPE = \sum_i \frac{hv_i}{2} \qquad (4.4)$$

where, h is the Planck constant and v_i is the computed real frequencies of the system. The entropy (S) can be calculated as follows:

$$S = k_B lnQ \qquad (4.5)$$

Q is the product of the partition function from the following equations.

$$Q = f_{trans}f_{vib}f_{rot} \qquad (4.6)$$

Translations: $\qquad f_{trans} = \dfrac{L\sqrt{2\pi m k_b T}}{h}$

Vibrations: $\qquad f_{vib} = \dfrac{1}{1 - e^{-h\omega/k_b T}}$

Rotations: $\qquad f_{rot} = \dfrac{8\pi^2 I k_b T}{h^2}$

All coverage species on β–MnO_2(110) surface are considered occupying one active site. The ordinary differential equations (ODEs) were solved by the steady-state approximation. The ODEs equations were integrated over time until all the coverage changes of surface intermediates equate to zero. The ODEs equation is expressed as follow:

$$\frac{d\theta_i}{dt} = \sum_j v_{i,j} r_j = 0 \qquad (4.7)$$

where θ_i is the coverage of the intermediate i, $v_{i,j}$ is the stoichiometric coefficient of intermediate at elementary step j, and r_j is the reaction rate coefficient of intermediate at elementary step j. The rate equations and the ODEs for each elementary step at the steady-state for HMF oxidation reaction were listed in **Table 4.1** and **Table 4.2**, respectively.

The degree of rate control ($X_{RC,i}$) for elementary step i and the thermodynamic rate control ($X_{TRC,n}$) as introduced by Campbell et al. (Campbell, 2017) was used to identify the rate-controlling step and key intermediates. The degree of rate control ($X_{RC,\,i}$) for elementary step i is calculated by the equation as follows:

$$X_{RC,i} = \frac{k_i}{r}\left(\frac{\partial r}{\partial k_i}\right)_{k_{j\neq i},K_i} = \left(\frac{\partial lnr}{\partial lnk_i}\right)_{k_{j\neq i},K_i} \qquad (4.8)$$

where r is the net reaction rate of the elementary step, and k_i is the rate constant. Similarly, the degree of thermodynamic rate control of an intermediate, n, was calculated from

$$X_{TRC,n} = \frac{1}{r}\left(\frac{r}{\left(\frac{-G_n^0}{RT}\right)}\right)_{G_{m\neq n}^0,\,G_i^0 TS} \qquad (4.9)$$

where the Gibbs free energy of all other intermediates (m ≠ n) and all transition states (i) are held constant. The numeric values of X_{RC} and X_{TRC} represent the degree of influence of the transition state and intermediates on the overall reactions — the larger value indicates the greater the impact. The range of these values is between 0 and 1. The positive and negative values refer to X_{RC} and X_{TRC}, respectively.

4.2.4 Synthesis and characterization of β–MnO$_2$

The preparation and characterization of the β–MnO$_2$ catalyst were carried out by Dr. Kajornsak Faungnawakij et al., γ–MnO$_2$ (Wako Pure Chemical Industries, 99.5%) powder was mixed using a wet ball-milling apparatus and pulverized at 600 rpm for 8 h. The black mixture was filtered to separate the powder before being dried in an oven at 373 K overnight. The obtained powder was ground and calcined for 3 h at 773 K. The phase transformation analysis was carried out via powder X-ray diffraction (XRD; D8 ADVANCE, Bruker) using CuK$_\alpha$ radiation. The specific surface area of sample was determined by nitrogen adsorption-desorption isotherms measured at 77 K using a Quantachrome Autosorb-iQ3 surface area and pore size analyzer, and the Brunauer–Emmett–Teller (BET) surface area was estimated over the relative pressure (P/P0) range of 0.13-0.28. Sample moisture was removed by heating at 423 K

for 4 h under vacuum prior to its measurement. The morphology was characterized by field emission-scanning electron microscope (FE-SEM; SU8030, Hitachi).

4.2.5 Procedure for catalytic oxidation

The catalytic oxidation of HMF to FDCA over the as-synthesized $\beta-MnO_2$ was carried out using a continuous-flow reactor by Dr. Kajornsak Faungnawakij et al., The obtained $\beta-MnO_2$ powders were compressed into pellets before crushing and sieving to the granule size of 180-500 μm. A continuous system consists of a liquid feed unit, oxygen gas (O_2) feed unit, reactor unit, and a liquid product collection unit. To the reactor unit, a custom-made continuous-flow fixed-bed reactor made of the stainless steel 316, with an external diameter of 1.28 cm, internal diameter of 1 cm, and length of 70 cm was used. The catalyst bed was located at the middle of the fixed-bed reactor and held in position with quartz wool plugs. The temperature was controlled by using electrical furnace with two positions of temperature controller. A K-type thermocouple was inserted to contact the catalyst bed for temperature monitoring. The pressure of the reactor was manually controlled by using back pressure regulator for O_2 flow. High-performance liquid chromatography (HPLC) pump was used to control the flow rate of reaction solution feed.

In a typical run, 1-4 mL (ca. 1.5-6 g) of catalyst was loaded into a reactor. The reaction was performed at 393 K under 1 MPa of O_2 atmosphere, and liquid feed (i.e., 40 mM HMF under 3 equivalent $NaHCO_3$) was introduced into the reactor with liquid hourly space velocity (LHSV) of 1-4 h^{-1}. To study the HMF oxidation over bare $\beta-MnO_2$ surface, deionized (DI) water as a solvent used to prepare the HMF solution was replaced by dimethyl sulfoxide (DMSO) while the insoluble $NaHCO_3$ was removed by filtration. During the reaction, liquid product mixtures were collected in 4-24 h interval for 72 h time-on-stream. The collected solutions were filtered using 0.22 μm pore size membrane filter and the filtrate was diluted 10 times with fresh solvent. The formation of FDCA and their intermediates and the decreasing of HMF were investigated using the HPLC (Shimadzu), with a UV detector adjusted to 260 nm for analysis of FDCA and HMFCA and to 280 nm for analysis of HMF, FFCA and DFF, using an Aminex HPX-87H ion-exchange column (300 mm in length with a 7.8 mm

i.d.; Bio-Rad, Hercules, CA, USA). The column temperature was set at 318 K. The samples were eluted with 5 mM sulfuric acid solution in DI water at a flow rate of 0.6 mL/min.

Table 4.1 Elementary Steps and the rate equations of HMF oxidation reaction on β–MnO$_2$(110) surface used in the microkinetic modeling.

Reaction step	Elementary step	Rate equations
R1	$C_6H_6O_3(g) + * \rightleftharpoons C_6H_6O_3\text{-}I^*$	$r_1 = k_1 P_{C_6H_6O_3}\theta_* - k_{-1}\theta_{C_6H_6O_3-I^*}$
Pathway A-bare		
R2	$C_6H_6O_3\text{-}I^* \rightleftharpoons C_6H_6O_3\text{-}II^*$	$r_2 = k_2\theta_{C_6H_6O_3-I^*} - k_{-2}\theta_{C_6H_6O_3-II^*}$
R3	$C_6H_6O_3\text{-}II^* + O^* \rightleftharpoons C_5H_5O_2COO^* + H^* + V_O^*$	$r_3 = k_3\theta_{C_6H_6O_3-II^*} - k_{-3}\theta_{C_5H_5O_2COO*}\theta_{H*}\theta_{V_O*}$
R4	$C_5H_5O_2COO^* + H^* \rightleftharpoons C_6H_6O_4^*$	$r_4 = k_4\theta_{C_5H_5O_2COO*}\theta_{H*} - k_{-4}\theta_{C_6H_6O_4*}$
R5	$C_6H_6O_4^* \rightleftharpoons C_5H_3O_3CH_2O^* + H^*$	$r_5 = k_5\theta_{C_6H_6O_4*} - k_{-5}\theta_{C_5H_3O_3CH_2O*}\theta_{H*}$
R6	$C_5H_3O_3CH_2O^* \rightleftharpoons C_5H_2O_3CHO^* + 2H^*$	$r_6 = k_6\theta_{C_5H_3O_3CH_2O*} - k_{-6}\theta_{C_5H_2O_3CHO*}\theta_{H*}^2$
R7	$C_5H_2O_3CHO^* + H^* \rightleftharpoons C_6H_4O_4\text{-}I^*$	$r_7 = k_7\theta_{C_5H_2O_3CHO*}\theta_{H*} - k_{-7}\theta_{C_6H_4O_4*-I^*}$
Pathway B-bare		
R8	$C_6H_6O_3\text{-}I^* \rightleftharpoons C_5H_3O_2CH_2O^* + H^*$	$r_8 = k_8\theta_{C_6H_6O_3-I^*} - k_{-8}\theta_{C_5H_3O_2CH_2O*}\theta_{H*}$
R9	$C_5H_3O_2CH_2O^* \rightleftharpoons C_6H_4O_3^* + H^*$	$r_9 = k_9\theta_{C_5H_3O_2CH_2O*} - k_{-9}\theta_{C_6H_4O_3*}\theta_{H*}$
R10	$C_6H_4O_3^* + O^* \rightleftharpoons C_5H_3O_2COO^* + H^* + V_O^*$	$r_{10} = k_{10}\theta_{C_6H_4O_3*} - k_{-10}\theta_{C_5H_3O_2COO*}\theta_{H*}\theta_{V_O*}$
R11	$C_5H_3O_2COO^* + H^* \rightleftharpoons C_6H_4O_4\text{-}I^*$	$r_{11} = k_{11}\theta_{C_5H_3O_2COO*}\theta_{H*} - k_{-11}\theta_{C_6H_4O_4-I^*}$
Pathway C-bare		
R12	$C_6H_4O_4\text{-}I^* \rightleftharpoons C_6H_4O_4\text{-}II^*$	$r_{12} = k_{12}\theta_{C_6H_4O_4-I^*} - k_{-12}\theta_{C_6H_4O_4-II^*}$

Table 4.1 Elementary Steps and the rate equations of HMF oxidation reaction on β–MnO$_2$(110) surface used in the microkinetic modeling (Continued).

Reaction step	Elementary step	Rate equations
R13	FFCA-II* + H* ⇌ C$_5$H$_3$O$_3$CHOH*	$r_{13} = k_{13}\theta_{C_6H_4O_4-II^*}\theta_{H*} - k_{-13}\theta_{C_5H_3O_3CHOH*}$
R14	C$_5$H$_3$O$_3$CHOH* + O* ⇌ C$_6$H$_4$O$_5$* + V$_O$*	$r_{14} = k_{14}\theta_{C_5H_3O_3CHOH*} - k_{-14}\theta_{C_6H_4O_5*}\theta_{V_O*}$
R15	C$_6$H$_4$O$_5$* ⇌ C$_6$H$_4$O$_5$ (g) + *	$r_{15} = k_{15}\theta_{C_6H_4O_5*} - k_{-15}P_{C_6H_4O_5}\theta_*$
Pathway B-OH		
R16 (or R8)	C$_6$H$_6$O$_3$-I* ⇌ C$_5$H$_3$O$_2$CH$_2$O* + H*	$r_{16} = k_{16}\theta_{C_6H_6O_3-I^*} - k_{-16}\theta_{C_5H_3O_2CH_2O*}\theta_{H*}$
R17	C$_5$H$_3$O$_2$CH$_2$O* + *OH ⇌ DFF* + H$_2$O*	$r_{17} = k_{17}\theta_{C_5H_3O_2CH_2O*}\theta_{OH*} - k_{-17}\theta_{C_6H_4O_3*}\theta_{H_2O*}$
R18	DFF* + *OH ⇌ C$_5$H$_3$O$_2$CHOOH*	$r_{18} = k_{18}\theta_{C_6H_4O_3*}\theta_{OH*} - k_{-18}\theta_{C_5H_3O_2CHOOH*}$
R19	C$_5$H$_3$O$_2$CHOOH* + *OH ⇌ C$_6$H$_4$O$_4$* + H$_2$O*	$r_{19} = k_{19}\theta_{C_5H_3O_2CHOOH*}\theta_{OH*} - k_{-19}\theta_{C_6H_4O_4*}\theta_{H_2O*}$
Pathway CI-OH		
R20 (or R13)	C$_6$H$_4$O$_4$* + H* ⇌ C$_5$H$_3$O$_3$CHOH*	$r_{20} = k_{20}\theta_{C_6H_4O_4*}\theta_{H*} - k_{-20}\theta_{C_5H_3O_3CHOH*}$
R21	C$_5$H$_3$O$_3$CHOH* + *OH + O* ⇌ C$_6$H$_4$O$_5$* + H$_2$O* + V$_O$*	$r_{21} = k_{21}\theta_{C_5H_3O_3CHOH*}\theta_{H*} - k_{-21}\theta_{C_6H_4O_5*}\theta_{H_2O*}\theta_{V_O*}$
R22	C$_6$H$_4$O$_5$* + H$_2$O* ⇌ C$_6$H$_4$O$_5$ (g) + * + H$_2$O*	$r_{22} = k_{22}\theta_{C_6H_4O_5*}\theta_{H_2O*} - k_{-22}P_{C_6H_4O_5}\theta_*\theta_{H_2O*}$
Pathway CII-OH		
R23	C$_6$H$_4$O$_4$* + *OH ⇌ C$_5$H$_3$O$_3$CHOOH*	$r_{23} = k_{23}\theta_{C_6H_4O_4*}\theta_{OH*} - k_{-23}\theta_{C_5H_3O_3CHOOH*}$
R24	C$_5$H$_3$O$_3$CHOOH* + *OH ⇌ C$_6$H$_4$O$_5$* + H$_2$O*	$r_{24} = k_{24}\theta_{C_5H_3O_3CHOOH*}\theta_{OH*} - k_{-24}\theta_{C_6H_4O_5*}\theta_{H_2O*}$
R25	C$_6$H$_4$O$_5$* + H$_2$O* ⇌ C$_6$H$_4$O$_5$ (g) + * + H$_2$O*	$r_{25} = k_{25}\theta_{C_6H_4O_5*}\theta_{H_2O*} - k_{-25}P_{C_6H_4O_5}\theta_*\theta_{H_2O*}$

Table 4.2 The ODE for each elementary step at the steady state of HMF oxidation reaction on bare- and hydroxylated surfaces.

MKM-I	MKM-II
$\dfrac{d\theta_{C_6H_6O_3-I^*}}{dt} = r_1 - r_2 - r_8$	$\dfrac{d\theta_{C_6H_6O_3-I^*}}{dt} = r_1 - r_2 - r_{16}$
$\dfrac{d\theta_{C_6H_6O_3-II^*}}{dt} = r_2 - r_3$	$\dfrac{d\theta_{C_6H_6O_3-II^*}}{dt} = r_2 - r_3$
$\dfrac{d\theta_{C_5H_5O_2COO*}}{dt} = r_3 - r_4$	$\dfrac{d\theta_{C_5H_5O_2COO*}}{dt} = r_3 - r_4$
$\dfrac{d\theta_{C_6H_6O_4*}}{dt} = r_4 - r_5$	$\dfrac{d\theta_{C_6H_6O_4*}}{dt} = r_4 - r_5$
$\dfrac{d\theta_{C_5H_3O_3CH_2O*}}{dt} = r_5 - r_6$	$\dfrac{d\theta_{C_5H_3O_3CH_2O*}}{dt} = r_5 - r_6$
$\dfrac{d\theta_{C_5H_2O_3CHO*}}{dt} = r_6 - r_7$	$\dfrac{d\theta_{C_5H_2O_3CHO*}}{dt} = r_6 - r_7$
$\dfrac{d\theta_{C_6H_4O_4-I*}}{dt} = r_7 + r_{11} - r_{12}$	$\dfrac{d\theta_{C_6H_4O_4*}}{dt} = r_7 + r_{19} - r_{13}$
$\dfrac{d\theta_{C_5H_3O_2CH_2O*}}{dt} = r_8 - r_9$	$\dfrac{d\theta_{C_5H_3O_2CH_2O*}}{dt} = r_{16} - r_{17}$
$\dfrac{d\theta_{C_6H_4O_3*}}{dt} = r_9 - r_{10}$	$\dfrac{d\theta_{C_6H_4O_3*}}{dt} = r_{17} - r_{18}$
$\dfrac{d\theta_{C_5H_3O_2COO*}}{dt} = r_{10} - r_{11}$	$\dfrac{d\theta_{C_5H_3O_2CHOOH*}}{dt} = r_{18} - r_{19}$
$\dfrac{d\theta_{C_6H_4O_4-II*}}{dt} = r_{12} - r_{13}$	$\dfrac{d\theta_{C_5H_3O_3CHOH*}}{dt} = r_{13} - r_{14}$
$\dfrac{d\theta_{C_5H_3O_3CHOH*}}{dt} = r_{13} - r_{14}$	$\dfrac{d\theta_{C_6H_4O_5*}}{dt} = r_{14} - r_{15}$
$\dfrac{d\theta_{C_6H_4O_5*}}{dt} = r_{14} - r_{15}$	

Table 4.2 The ODE for each elementary step at the steady state of HMF oxidation reaction on bare- and hydroxylated surfaces (Continued).

MKM-III	MKM-IV
$\dfrac{d\theta_{C_6H_6O_3-I^*}}{dt} = r_1 - r_2 - r_{16}$	$\dfrac{d\theta_{C_6H_6O_3-I^*}}{dt} = r_1 - r_2 - r_{16}$
$\dfrac{d\theta_{C_6H_6O_3-II^*}}{dt} = r_2 - r_3$	$\dfrac{d\theta_{C_6H_6O_3-II^*}}{dt} = r_2 - r_3$
$\dfrac{d\theta_{C_5H_5O_2COO*}}{dt} = r_3 - r_4$	$\dfrac{d\theta_{C_5H_5O_2COO*}}{dt} = r_3 - r_4$
$\dfrac{d\theta_{C_6H_6O_4*}}{dt} = r_4 - r_5$	$\dfrac{d\theta_{C_6H_6O_4*}}{dt} = r_4 - r_5$
$\dfrac{d\theta_{C_5H_3O_3CH_2O*}}{dt} = r_5 - r_6$	$\dfrac{d\theta_{C_5H_3O_3CH_2O*}}{dt} = r_5 - r_6$
$\dfrac{d\theta_{C_5H_2O_3CHO*}}{dt} = r_6 - r_7$	$\dfrac{d\theta_{C_5H_2O_3CHO*}}{dt} = r_6 - r_7$
$\dfrac{d\theta_{C_6H_4O_4}}{dt} = r_7 + r_{19} - r_{20}$	$\dfrac{d\theta_{C_6H_4O_4}}{dt} = r_7 + r_{19} - r_{23}$
$\dfrac{d\theta_{C_5H_3O_2CH_2O*}}{dt} = r_{16} - r_{17}$	$\dfrac{d\theta_{C_5H_3O_2CH_2O*}}{dt} = r_{16} - r_{17}$
$\dfrac{d\theta_{C_6H_4O_3*}}{dt} = r_{17} - r_{18}$	$\dfrac{d\theta_{C_6H_4O_3*}}{dt} = r_{17} - r_{18}$
$\dfrac{d\theta_{C_5H_3O_2CHOOH*}}{dt} = r_{18} - r_{19}$	$\dfrac{d\theta_{C_5H_3O_2CHOOH*}}{dt} = r_{18} - r_{19}$
$\dfrac{d\theta_{C_5H_3O_3CHOH*}}{dt} = r_{20} - r_{21}$	$\dfrac{d\theta_{C_5H_3O_3CHOOH*}}{dt} = r_{23} - r_{24}$
$\dfrac{d\theta_{C_6H_4O_5*}}{dt} = r_{21} - r_{22}$	$\dfrac{d\theta_{C_6H_4O_5*}}{dt} = r_{24} - r_{25}$

4.3 Results and discussion

4.3.1 HMF adsorption on β–MnO$_2$(110) surface

The possible adsorption modes of HMF on the β–MnO$_2$(110) surface were carried out in this part. The HMF molecule possibly attaches the oxygen of hydroxyl group and/or the oxygen of formyl group with the surface forming a bridge-like configuration or end-on configurations as illustrated in **Figure 4.2.**
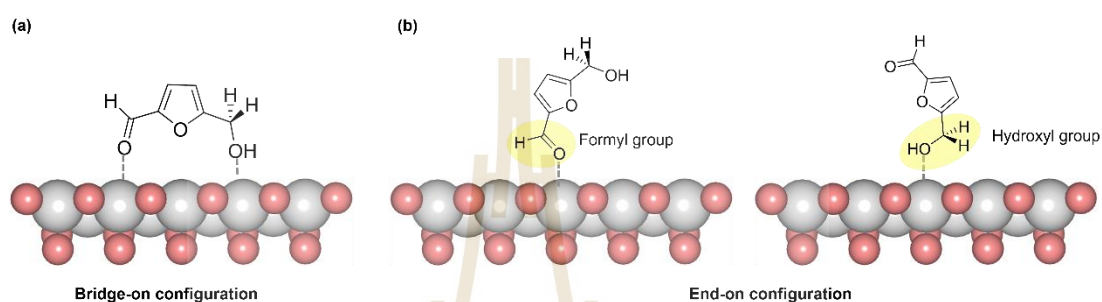
Figure 4.2 The HMF adsorption modes on the β–MnO$_2$(110) surface (a) bridge-on configuration, and (b) end-on configurations.

The adsorption energy (E$_{ads}$) of HMF molecule on β–MnO$_2$(110) surface was calculated as follows:

$$E_{ads} = E_{HMF/MnO2} - E_{MnO2} - E_{HMF}$$

where E$_{HMF/MnO2}$ is the total energy of the adsorbate molecule-substrate complex, E$_{MnO2}$ is the total energy of a bare β–MnO$_2$(110) surface, and E$_{HMF}$ is the total energy of an isolated HMF molecule in a vacuum. A negative E$_{ads}$ indicates energetically favorable adsorption.

The calculated adsorption energy (E$_{ads}$) and bond lengths between selected atoms of all possible adsorption configurations of HMF molecule on β–MnO$_2$(110) surface are summarized in **Table 4.3. Figure 4.3** shows the most stable adsorption configurations in each group including formyl-end on, hydroxyl-end on, vertical-bridge-on, and parallel-bridge on. Due to the unsaturated coordination of Mn$_{4c}$ sites enable them to act as active sites assisting the nucleophilic attack from both functional groups of HMF in the oxidation process. The formyl and hydroxyl groups of HMF molecule interact with the bridge-Mn$_{4c}$ site.

Table 4.3 The calculated E_{ads} (in eV), and bond distances (in Å) of selected atoms of all possible adsorption configurations of HMF molecules on β–MnO$_2$ surface.
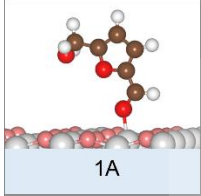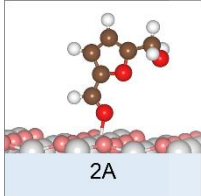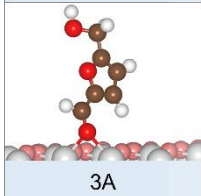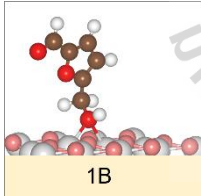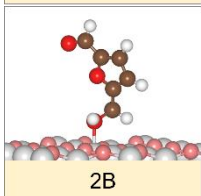
Configurations	Favored sites	ΔE_{ads} (eV)	$O_{(OH)}$–Mn (Å)	$O_{(c=o)}$–Mn (Å)	$H_{(OH)}$–O (Å)
Formyl-End-on adsorption modes					
1A	top-Mn$_{4C}$	−0.13	–	2.02	–
2A	top-Mn$_{5C}$	−0.06	–	2.08	–
3A	bridge-Mn$_{4C}$	0.53	–	2.18, 2.06	–
Hydroxyl-End-on adsorption modes					
1B	bridge-Mn$_{4C}$	−0.82	2.20, 2.33	–	2.36, 2.47
2B	top-Mn$_{5C}$	−0.53	2.13	–	2.23, 2.80

Table 4.3 The calculated E_{ads} (in eV), and bond distances (in Å) of selected atoms of all possible adsorption configurations of HMF molecules on β–MnO$_2$ surface (Continued).
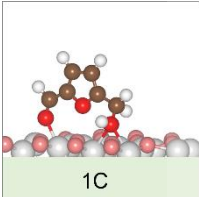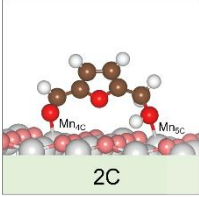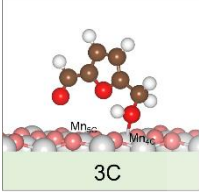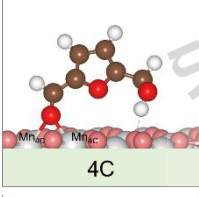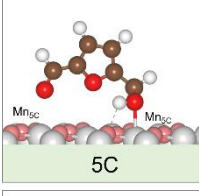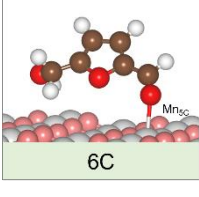
Configurations	Favored sites	ΔE_{ads} (eV)	$O_{(OH)}$_Mn (Å)	$O_{(c=o)}$_Mn (Å)	$H_{(OH)}$_O (Å)
Vertical-Bridge-on adsorption modes					
1C	bridge-Mn$_{4C}$	−0.34	2.26, 2.34	2.13, 2.91	2.22, 2.29
2C	Mn$_{4C}$ -Mn$_{5C}$	−0.19	2.27	2.27	1.78
3C	Mn$_{4C}$ -Hollow	−0.08	2.27, 2.53	-	2.29, 2.38
4C	O$_{(c=o)}$ -bridge	−0.25	-	2.05, 2.30	1.74
5C	Mn$_{5C}$ -Mn$_{5C}$	0.32	-	2.21	2.03
6C	Mn$_{5C}$ - Hollow	0.14	3.42	2.38	2.57

Table 4.3 The calculated E_{ads} (in eV), and bond distances (in Å) of selected atoms of all possible adsorption configurations of HMF molecules on β–MnO$_2$ surface (Continued).
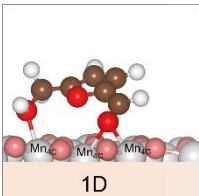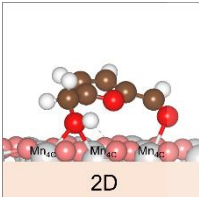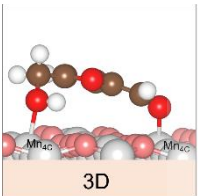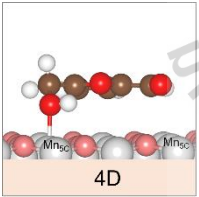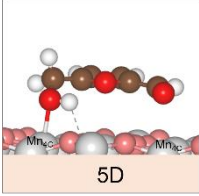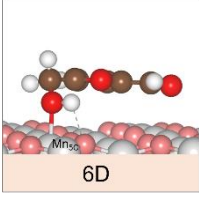
Configurations	Favored sites	ΔE_{ads} (eV)	O$_{(OH)}$_Mn (Å)	O$_{(c=o)}$_Mn (Å)	H$_{(OH)}$_O (Å)
Parallel-Bridge-on adsorption modes					
1D	O$_{(c=o)}$ bridge/ O$_{(OH)}$ Mn$_{4C}$	−1.44	2.24, 3.26	2.19, 2.33	2.24
2D	O$_{(OH)}$ bridge /O$_{(c=o)}$ Mn$_{4C}$	−1.25	2.29, 2.31	2.26, 2.83	1.94
3D	O$_{(OH)}$ top-Mn$_{4C}$ /O$_{(c=o)}$ bridge-Mn$_{4C}$	−1.14	2.30	2.32, 2.59	2.46
4D	top-Mn$_{5C}$/top-Mn$_{5C}$	−1.08	2.21	3.11	2.17
5D	O$_{(OH)}$ top-Mn$_{4C}$	−1.11	2.29	–	2.09
6D	O$_{(OH)}$ top-Mn$_{5C}$	−1.13	2.23	–	2.10

Table 4.3 The calculated E_{ads} (in eV), and bond distances (in Å) of selected atoms of all possible adsorption configurations of HMF molecules on β–MnO$_2$ surface (Continued).
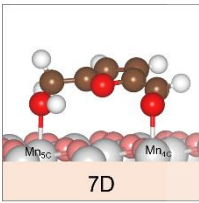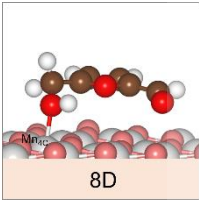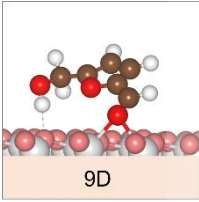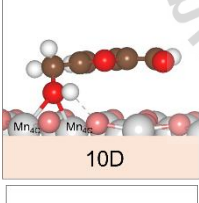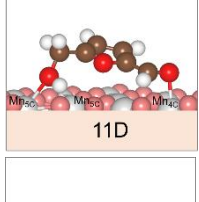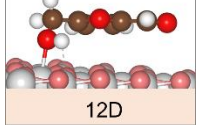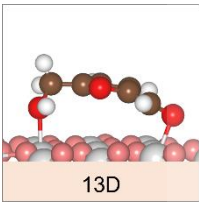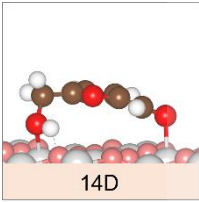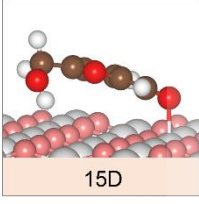
Configurations	Favored sites	ΔE_{ads} (eV)	$O_{(OH)}$_Mn (Å)	$O_{(c=o)}$_Mn (Å)	$H_{(OH)}$_O (Å)
7D	$O_{(OH)}$ top-Mn$_{5C}$/ $O_{(c=o)}$ top-Mn$_{4C}$	0.10	2.29	2.20	2.25
8D	$O_{(OH)}$ top-Mn$_{4C}$ /$O_{(c=o)}$ top-Mn$_{5C}$	−0.36	2.16	2.25	2.16
9D	$O_{(c=o)}$ bridge-Mn$_{4C}$	−0.72	–	2.29, 2.25	1.18
10D	$O_{(OH)}$ bridge-Mn$_{4C}$	−0.19	2.33, 2.23	–	1.93
11D	$O_{(OH)}$ Hollow-Mn$_{5C}$ /$O_{(c=o)}$ top-Mn$_{4C}$	0.34	2.29, 2.27	2.13	1.15
12D	$O_{(OH)}$ top-Mn$_{4C}$ /$O_{(c=o)}$ Parallel-Hollow	−1.27	2.15	–	1.95

Parallel-Bridge-on adsorption modes

Table 4.3 The calculated E_{ads} (in eV), and bond distances (in Å) of selected atoms of all possible adsorption configurations of HMF molecules on β–MnO$_2$ surface (Continued).

Configurations	Favored sites	ΔE_{ads} (eV)	$O_{(OH)}$_Mn (Å)	$O_{(c=o)}$_Mn (Å)	$H_{(OH)}$_O (Å)
Parallel-Bridge-on adsorption modes					
13D	$O_{(OH)}$ top-Mn$_{5C}$ /$O_{(c=o)}$ top-Mn$_{4C}$	−0.82	2.32	2.19	–
14D	$O_{(OH)}$ bridge-Mn$_{4C}$ /$O_{(c=o)}$ bridge-Mn$_{4C}$	−0.24	2.30, 2.59	2.33, 3.26	1.79
15D	$O_{(c=o)}$ top-Mn$_{5C}$	−0.50	–	2.30	1.91

The HMF molecule points oxygen atoms of hydroxyl toward the Mn$_{4c}$ site and formyl groups toward the on-bridge site called a 1D parallel configuration (see **Figure 4.3**). The most stable is the 1D configuration with an adsorption energy of −1.44 eV. This indicates chemisorption and quite strong binding of HMF on β–MnO$_2$(110). Similarly, 2D and 3D parallel configurations show the E_{ads} of −1.25 eV and −1.14 eV, respectively. The bridge-on configurations are preferable than the end-on configurations, which agrees well with the result of HMF adsorption on β–MnO$_2$(110) reported previously (Ren, Song et al., 2018). The calculated E_{ads} in this work is similar to the HMF adsorption on Pd/α–MnO$_2$(110) (−3.34 eV),(Liao, Hou et al., 2019) Pd$_{13}$/α–MnO$_2$(110) (−2.79 eV), (Liao, Hou et al., 2019) which are more energetically

stable than that of Co$_3$O$_4$(110) (−1.56 eV) (Ren, Song et al., 2018), and CuO(111) (−0.79 eV). (Ren, Song et al., 2018)

It is to be noted that the 2D configuration was used as the initial structure to study the reaction mechanism of the HMF oxidation to FDCA. Its E$_{ads}$ value is slightly higher than that of the 1D configuration and its structure is more suitable for the oxidation reaction. The hydrogen bond between H of hydroxyl group and the oxygen active site on the surface with the distance of 1.94 Å leading to the O−H bond elongation from 0.97 Å to 0.99 Å.
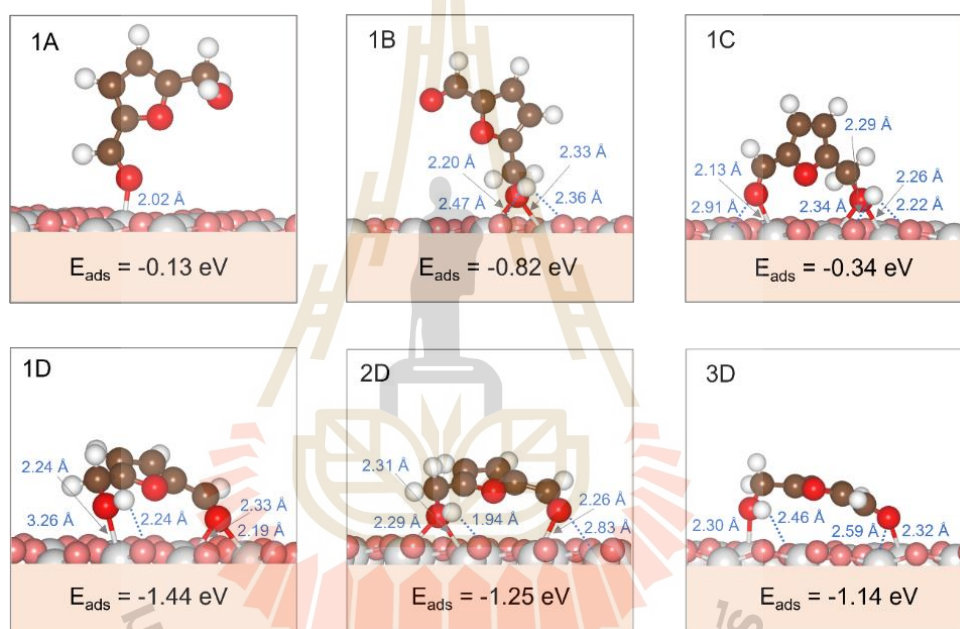
Figure 4.3 The possible adsorption configurations of HMF on the β−MnO$_2$(110) surface.

4.3.2 Mechanistic study of the HMF oxidation reaction on bare β−MnO$_2$(110) surface using DFT

The simplified mechanism of the HMF-to-FDCA reaction over β−MnO$_2$ is illustrated in **Figure 4.4.** The main reaction can proceed via two possible pathways: (i) an aldehyde group is firstly oxidized to produce HMFCA as a key intermediate (or pathway A), and (ii) an alcohol group is oxidized to produce DFF as a key

intermediate (or pathway B). Both paths further produce FFCA as another key intermediate, then converts to FDCA as a final product via pathway C.
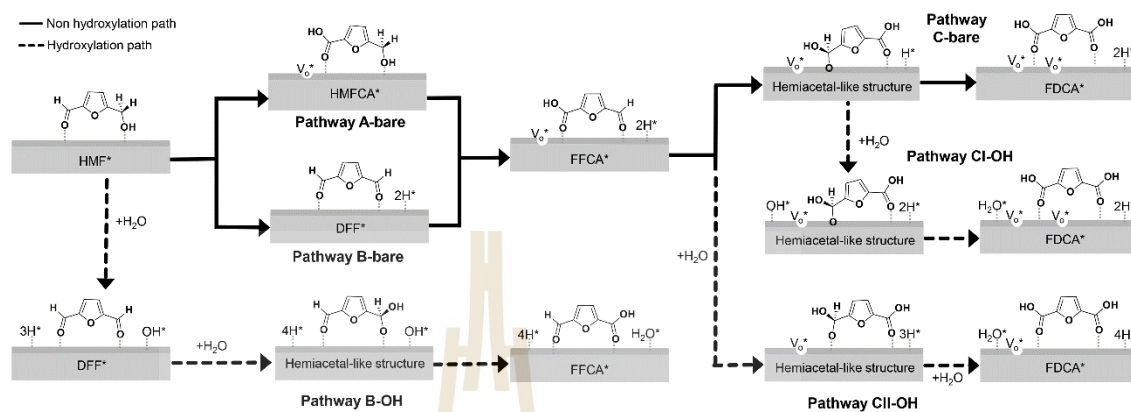
Figure 4.4 Simplified pathways of HMF oxidation to produce FDCA on the bare surface (black solid line) and hydroxylated surface (black dash line) and microkinetic models (color lines).

This part investigates possible reaction pathways of HMF oxidation to FDCA on bare β–MnO_2(110) using DFT calculations. The mechanism of the HMF-to-FDCA reaction on bare β–MnO_2(110) surface was carried out according to the simplified pathways in **Figure 4.4.** Over the non-hydroxylated surface, HMF can be initially oxidized via two possible intermediates, HMFCA in pathway A-bare or DFF in pathway B-bare, to form FFCA. Then, FFCA intermediate is further oxidized into FDCA as the final product in pathway C-bare. The elementary steps and their calculated energy barriers of the reaction on bare surface, elementary steps R1 to R15, are given in **Table 4.1.** The energy profile of HMF oxidation on bare β–MnO_2(110) surface at 0 K, 393 K and the relevant configurations are given in **Figure 4.5a, 4.5b, and 4.8**, respectively.
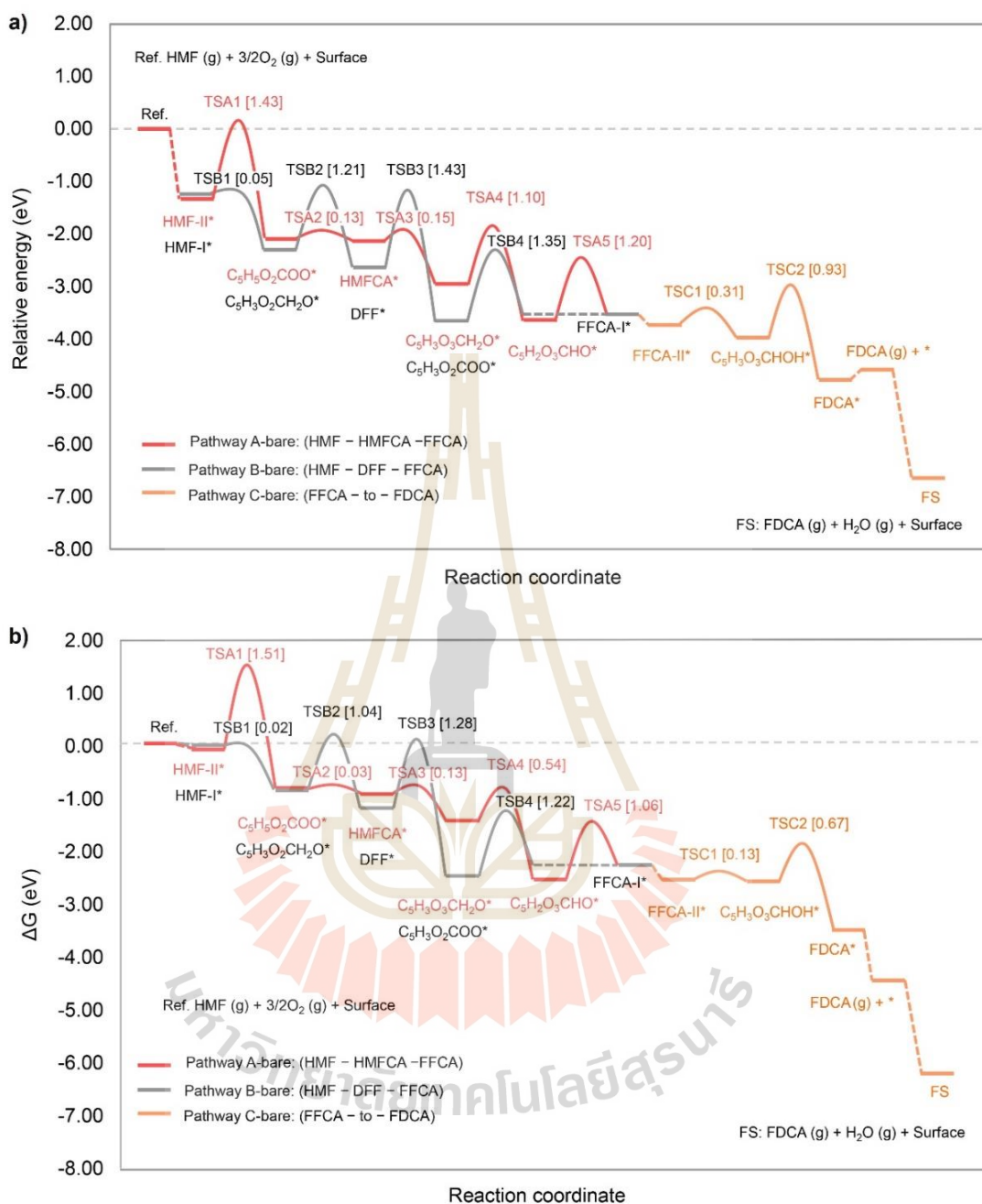
Figure 4.5 a) Energy profile at 0 K and b) Gibbs free energy profile (ΔG) of HMF oxidation on bare β–MnO$_2$(110) surface at 393 K.

After the HMF adsorption, C$_6$H$_6$O$_3$-I* rearranges to C$_6$H$_6$O$_3$-II*, the reaction step R2. As depicted in **Figure 4.5**, pathway A-bare starts from breaking the C–H bond at the formyl group of HMF to form the carboxylate intermediate, C$_5$H$_5$O$_2$COO* represented

by the reaction step R3. In **Figure 4.5b**, the first activation step requires the $\Delta G^{\neq}$ of 1.51 eV to surmount TSA1 and further forms $C_6H_6O_4$*, HMFCA, via the step R4. Then, the -CH_2OH group of HMFCA is further oxidized to $C_6H_4O_4$*, FFCA, via the reaction steps R5 to R7. The highest barrier of the HMFCA to FFCA path is the TSA5 state with the $\Delta G^{\neq}$ of 1.06 eV. Note that the formation of oxygen vacancy (V_O*) occurs at TSA1 leading to the highest energy barrier in the HMF-HMFCA-FFCA route.

For the second possible pathway, pathway B-bare proceeds through the elementary steps R8 to R11 represented by the configurations in **Figure 4.8.** The O–H bond of the hydroxyl group is dissociated first followed by the C-H dissociation of -CH_2O at TSB2 to form DFF or $C_6H_4O_3$*. Then, DFF is further oxidized to FFCA via TSB3 and TSB4 in the reaction steps R10 and R11, respectively. According to the $\Delta G^{\neq}$ values of pathway B-bare, the HMF-to-DFF process is easier than the DFF-to-FFCA process. The highest barrier of this pathway is located at TSB3 with the $\Delta G^{\neq}$ of 1.28 eV that the oxygen vacancy forms to yield the carboxylate intermediate.

For pathway C-bare, FFCA is oxidized to FDCA as depicted by the orange path in **Figure 4.5b.** As shown in **Figure 4.8**, the adsorbed FFCA molecule (or $C_6H_4O_4$-I*) rearranges to the C_6H_4O-II* configuration in which the C of carbonyl group binds with the surface oxygen. The reaction surmounts the TSC1 and TSC2 states to form FDCA with the barriers of 0.13 and 0.67 eV, respectively. For the reaction step R14, the $C_5H_3O_3CHOH$* intermediates and TSC2 reveal the hemiacetal-like form, in which C of the molecule forms a chemical bond with the surface oxygen. This hemiacetal compound was also proposed as one intermediate of the HMF to FDCA in other catalysts such as Co_3O_4-NPs-MnCoO and CeO_2-supported Au (Kim, Su et al., 2018, Wei, Zhang et al., 2022).

The mechanistic study of the HMF oxidation over non-hydroxylated surface can be summarized as follows. First, the reaction is an exothermic process with the ΔG_r of −6.21 eV. Second, oxidation of the formyl group to the carboxylate intermediate is the most difficult step in pathways A-bare and B-bare due to the oxygen vacancy formation. Although, the oxygen vacancy formation is also involved in pathway C-bare, the energy barrier is lower than those in pathway A-bare and B-

bare due to the different form of intermediates (i.e. hemiacetal-like form, carboxylate form). Our results correspond well with the suggestion from other studies that the oxygen vacancy formation influences on the HMF oxidation in MnO_2 (Hayashi, Oba et al., 2019, Yao and Wang, 2021). The oxygen vacancy formation energy on the β–MnO2 (110) surface calculated in this work is 0.57 eV. The detail about oxygen vacancy formation energy on β–MnO_2 (110) surface is explained in the next part (4.3.3).

4.3.3 Mechanistic study of HMF oxidation reaction on hydroxylated β–MnO₂(110) surface using DFT

As mentioned earlier, the hydroxylation on the metal oxide surface is possible when using water as a solvent and tend to play a role on the HMF oxidation reaction. To understand hydroxylation over the β–MnO_2(110) surface, H_2O adsorption and dissociation in different coverage (θ) are investigated in this part. We found that water can adsorb and dissociates on the surface with the energy barrier of 0.12 eV indicating the facile dissociative adsorption. As shown in **Figure 4.6a** and **4.6b**, the E_{ads} increases (or less stability) when the coverage increases. **Figure 4.6c** and **4.6d** reveal the free energy increases when the temperature increases. The free energies of hydroxylated models with respect to the temperature indicate that the partial hydroxylation coverage (θ) in range of 0.06 to 0.13 is thermodynamically stable at 393K. Therefore, the role of hydroxyl group on the HMF oxidation was determined and discussed in this part. The favored pathway, the HMF-DFF-FDCA path, is focused herein. Each dissociated H_2O produces two hydroxyl groups near the active site at each elementary step. Each elementary step was corrected by the calculated activation- and reaction-free energy with its initial state.
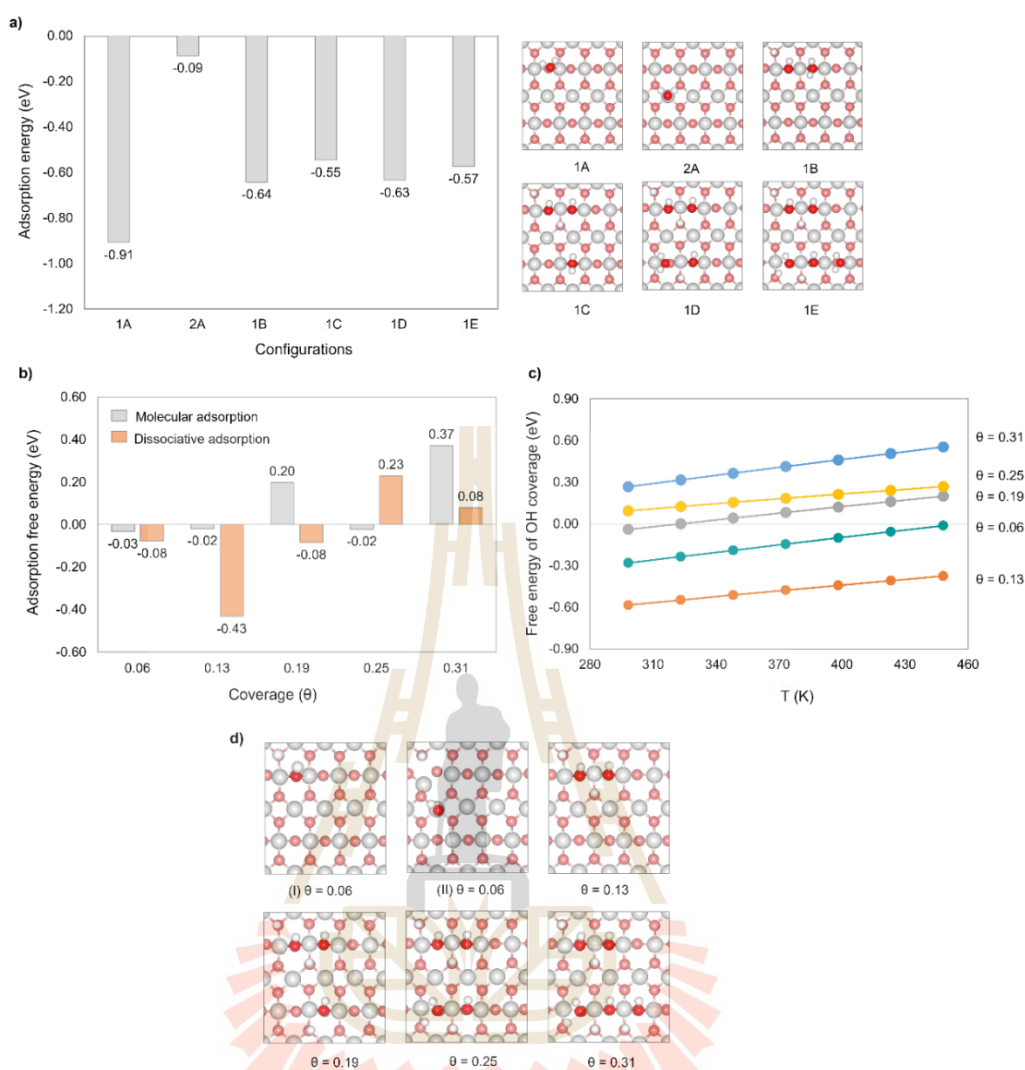
Figure 4.6 (a) Adsorption energy (E_{ads}) of H_2O on the bare-surfaces (1A and 2A) and hydroxylated surfaces (1B, 1C, 1D, and 1E). (b) Adsorption free energy (G_{ads}) of molecular and dissociated H_2O over β–MnO_2 at 393 K. (c) Free energy of OH coverage on β–MnO_2 versus temperature (T) and (d) the most stable structure of each OH coverage model.

Initially, the O-H dissociation of the adsorbed HMF is facile follows the reaction step R8. Then, the hydroxyl group starts to play a role in the latter steps. As a results, the energy profiles of the hydroxylated system at 0 K and 393 K, denoted as pathways B-OH, CI-OH and CII-OH, are compared with the favorable pathways of the bare surface, pathways B-bare and C-bare, in **Figure 4.7a** and **4.7b**, respectively. The

calculated results of elementary steps R17 to R22 and the relevant configurations are given in **Table 4.4** and **Figure 4.8**, respectively. On the hydroxylated surface, the nearby -OH facilitates the dehydrogenation of -CH_2=O* at TSB6 ($\Delta G^{\neq}$ of 0.28 eV) to form DFF, $C_6H_4O_3$*. Then, the OH insertion occurs at the TSB7 state of the reaction step R18 with the $\Delta G^{\neq}$ of 0.24 eV. The hemiacetal intermediate, $C_5H_3O_2CHOOH$*, is formed. Note that this process consumes lower energy than TSB3 of the step R10 from the non-hydroxylated surface, approximately 1.04 eV. The H abstraction from -CHOOH is also facilitated by the hydroxyl group at TSB8 ($\Delta G^{\neq}$ of 0.40 eV) to form FFCA and water.

The FFCA to FDCA reaction involves two possible pathways. First, pathway CI-OH is described by the reaction steps R20 and R21. The C atom of the carbonyl group binds with the surface oxygen then the hydrogenation process occurs at TSC3 of the reaction step R20 or R13 of pathway C-bare, $\Delta G^{\neq}$ of 0.13 eV. Next, the hydroxyl group abstract H from *CHOH. Meanwhile, the surface oxygen involves in the -COOH formation and the oxygen vacancy occurs in the reaction step R21 as depicted in Figure 4.7. It is noteworthy that the H abstraction from formyl group via TSC2 of the bare surface (0.67 eV) is preferable than TSC4 of the hydroxylated surface (1.01 eV).

For another possibility, pathway CII-OH proceeds through the elementary steps R23 to R25 represented by the configurations in **Figure 4.8** and the yellow profile in **Figure 4.7.** The OH insertion at the C atom of FFCA occurs to form hemiacetal-like intermediate, $C_5H_3O_3CHOOH$*, via TSC5 of the reaction step R23. This step is facile which consumes the 0.17 eV of $\Delta G^{\neq}$. Then, the hydroxyl group abstracts H from -CHOOH via TSC6 of the reaction step R24 with the $\Delta G^{\neq}$ of 0.49 eV. It is observed that the H abstraction from the formyl group by hydroxy via TSC6 is preferable than TSC2 and TSC4 in which the oxygen vacancy formation is required. In addition, the Bader charge properties of selected steps were further conducted. As shown in **Figure 4.10** in electronic charge analysis section (4.4.5), the hydroxyl groups pose negative charges in range of -0.6 to -0.5|e-|, which attract the positively charged H of the formyl group and C3 of the intermediate.

In summary, the hydroxyl group can promote the HMF oxidation by facilitating the C-H bond activation and OH insertion processes in the HMF-DFF-FFCA reaction

through pathway B-OH and FFCA-to-FDCA via pathway CII-OH. On the other hand, the OH group does not promote the FFCA oxidation through pathway CI-OH, since the C-H breaking by the active oxygen surface in TSC2 consumes lower activation energy. Therefore, in the presence of OH, FFCA to FDCA is very likely to be the rate limiting step as it possesses highest barriers on the hydroxylated surface. This theoretical finding is in good agreement with our experiment and other work.
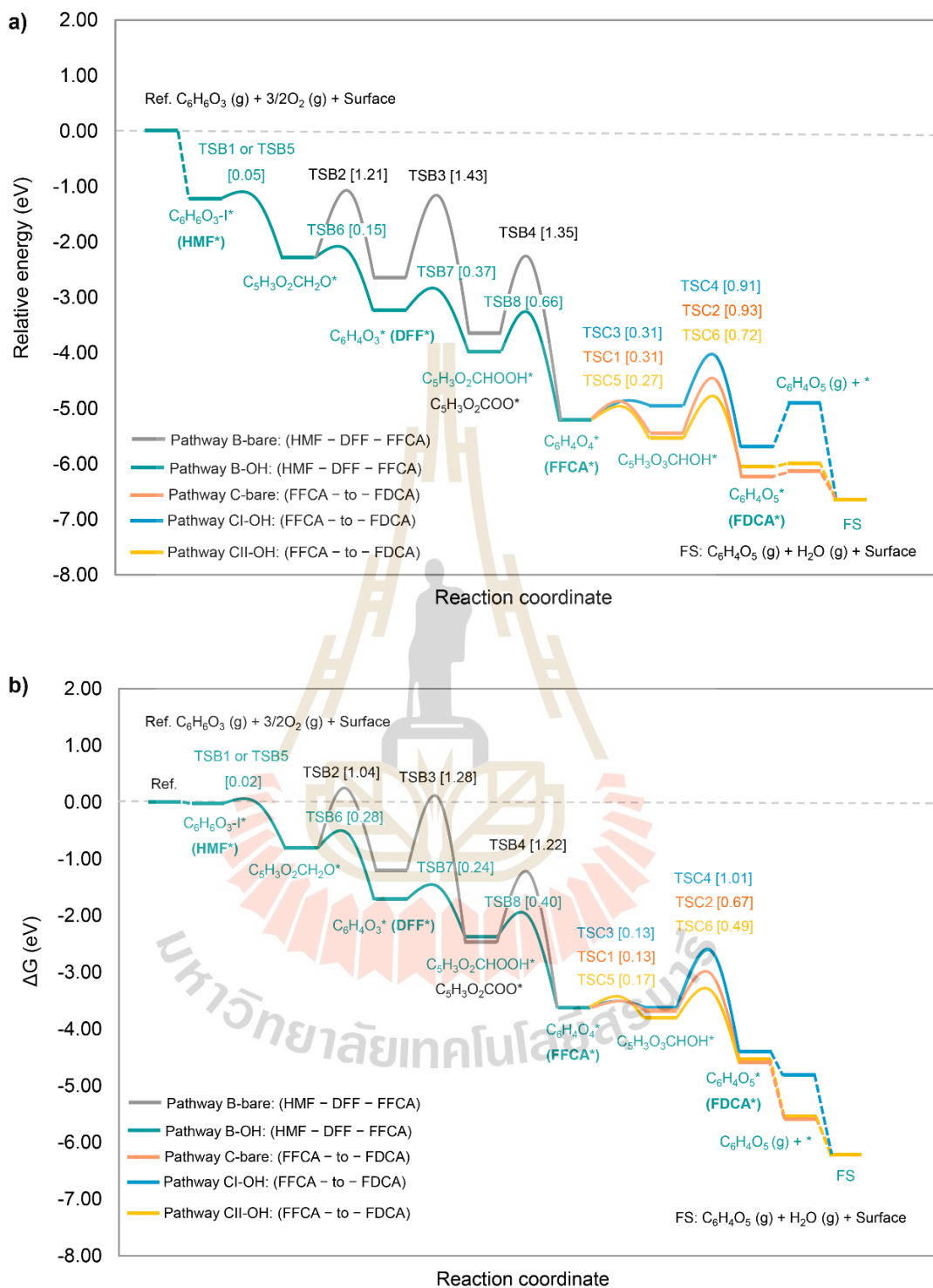
Figure 4.7 a) Energy profile at 0 K and b) Gibbs free energy profile (ΔG) of HMF oxidation on hydroxylated β–MnO$_2$(110) surface (green and yellow line) at 393 K.
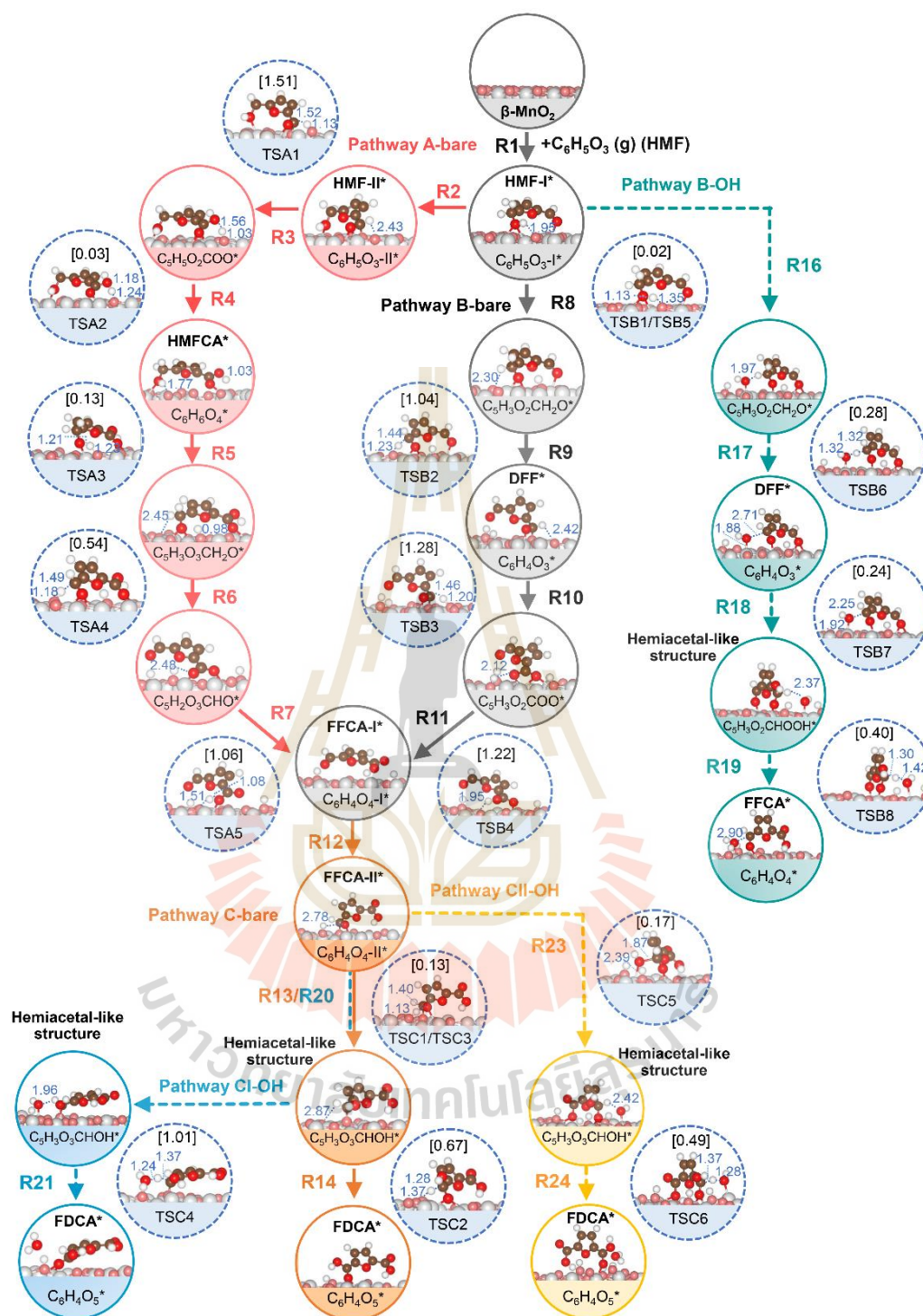
Figure 4.8 Geometries of the transition states (TS), intermediates for HMF oxidation on a bare surface (pathway A-bare, B-bare, and C-bare), and hydroxylated surface (pathway B-OH, CI-OH, and CII-OH). The $\Delta G^{\neq}$ barriers in eV are displayed in square brackets and the bond distance in Å is displayed as a blue value.

Table 4.4 The calculated activation free energy ($\Delta G^{\neq}$) and reaction free energy (ΔG_r) at 393 K, the calculated activation energy (E_a) and reaction energy (ΔE_r) at 0K, the forward rate constant (k_f) and equilibrium constant (K) for each elementary step of HMF oxidation on bare and hydroxylated β–MnO_2(110) surfaces.

Reaction step	Elementary step	$\Delta G^{\neq}$ (eV)	ΔG_r (eV)	E_a (eV)	ΔE_r (eV)	k_f (s^{-1})	K
R1	$C_6H_6O_3(g) + {}^* \rightleftharpoons C_6H_6O_3\text{-I}^*$		-0.03		-1.25	1.69×10^9	2.31×10^0
Pathway A-bare							
R2	$C_6H_6O_3\text{-I}^* \rightleftharpoons C_6H_6O_3\text{-II}^*$		-0.05		-0.06	8.19×10^{12}	4.22×10^0
R3	$C_6H_6O_3\text{-II}^* + O^* \rightleftharpoons C_5H_5O_2COO^* + H^* + V_O{}^*$	1.51	-0.74	1.43	-0.79	3.11×10^{-7}	3.32×10^9
R4	$C_5H_5O_2COO^* + H^* \rightleftharpoons C_6H_6O_4{}^*$	0.03	-0.12	0.13	-0.05	3.39×10^{12}	3.76×10^1
R5	$C_6H_6O_4{}^* \rightleftharpoons C_5H_3O_3CH_2O^* + H^*$	0.13	-0.51	0.15	-0.81	1.69×10^{11}	2.97×10^6
R6	$C_5H_3O_3CH_2O^* \rightleftharpoons C_5H_2O_3CHO^* + 2H^*$	0.54	-1.10	1.10	-0.69	1.06×10^6	1.34×10^{14}
R7	$C_5H_2O_3CHO^* + H^* \rightleftharpoons C_6H_4O_4\text{ -I}^*$	1.06	0.25	1.20	0.15	1.99×10^{-1}	7.27×10^{-4}
Pathway B-bare							
R8	$C_6H_6O_3\text{-I}^* \rightleftharpoons C_5H_3O_2CH_2O^* + H^*$	0.02	-0.81	0.05	-1.06	5.14×10^{12}	2.11×10^{10}
R9	$C_5H_3O_2CH_2O^* \rightleftharpoons C_6H_4O_3{}^* + H^*$	1.04	-0.37	1.21	-0.33	3.96×10^{-1}	5.98×10^4
R10	$C_6H_4O_3{}^* + O^* \rightleftharpoons C_5H_3O_2COO^* + H^* + V_{O^*}$	1.28	-1.27	1.43	-1.03	3.51×10^{-4}	1.95×10^{16}
R11	$C_5H_3O_2COO^* + H^* \rightleftharpoons C_6H_4O_4\text{ -I}^*$	1.22	0.17	1.35	0.16	1.91×10^{-3}	6.20×10^{-3}

Table 4.4 The calculated activation free energy ($\Delta G^{\neq}$) and reaction free energy (ΔG_r) at 393 K, the calculated activation energy (E_a) and reaction energy (ΔE_r) at 0K, the forward rate constant (k_f) and equilibrium constant (K) for each elementary step of HMF oxidation on bare and hydroxylated β–MnO$_2$(110) surfaces (Continued).

Reaction step	Elementary step	$\Delta G^{\neq}$ (eV)	ΔG_r (eV)	E_a (eV)	ΔE_r (eV)	k_f (s^{-1})	K
Pathway C-bare							
R12	$C_6H_4O_4$ -I* $\rightleftharpoons C_6H_4O_4$ -II*		-0.23		-0.24	8.19×10^{12}	9.93×10^{2}
R13	$C_6H_4O_4$ -II* + H* $\rightleftharpoons C_5H_3O_3CHOH^*$	0.13	-0.05	0.31	-0.22	1.84×10^{11}	3.98×10^{0}
R14	$C_5H_3O_3CHOH^*$ + O* $\rightleftharpoons C_6H_4O_5^*$ + V$_{O^*}$	0.67	-0.91	0.93	-0.79	2.28×10^{4}	4.49×10^{11}
R15	$C_6H_4O_5^*$ $\rightleftharpoons C_6H_4O_5$ (g) + *		-0.97		0.12	4.02×10^{21}	2.64×10^{12}
Pathway B-OH							
R16 (or R8)	$C_6H_6O_3$-I* $\rightleftharpoons C_5H_3O_2CH_2O^*$ + H*	0.02	-0.81	0.05	-1.06	5.14×10^{12}	2.11×10^{10}
R17	$C_5H_3O_2CH_2O^*$ + *OH $\rightleftharpoons C_6H_4O_3^*$ + H$_2$O*	0.28	-0.89	0.15	-0.94	2.33×10^{9}	2.25×10^{11}
R18	$C_6H_4O_3^*$ + *OH $\rightleftharpoons C_5H_3O_2CHOOH^*$	0.24	-0.69	0.37	-0.74	7.51×10^{9}	7.13×10^{8}
R19	$C_5H_3O_2CHOOH^*$ + *OH $\rightleftharpoons C_6H_4O_4^*$ + H$_2$O*	0.40	-1.23	0.66	-1.24	5.98×10^{7}	5.59×10^{15}
Pathway CI-OH							
R20 (or R13)	$C_6H_4O_4^*$ + H* $\rightleftharpoons C_5H_3O_3CHOH^*$	0.13	-0.01	0.31	0.27	1.84×10^{11}	1.31×10^{0}
R21	$C_5H_3O_3CHOH^*$ + *OH + O* $\rightleftharpoons C_6H_4O_5^*$ + H$_2$O* + V$_O^*$	1.01	-0.79	0.91	-0.76	8.50×10^{-1}	1.48×10^{10}

Table 4.4 The calculated activation free energy ($\Delta G^{\neq}$) and reaction free energy (ΔG_r) at 393 K, the calculated activation energy (E_a) and reaction energy (ΔE_r) at 0K, the forward rate constant (k_f) and equilibrium constant (K) for each elementary step of HMF oxidation on bare and hydroxylated β–MnO_2(110) surfaces (Continued).

Reaction step	Elementary step	$\Delta G^{\neq}$ (eV)	ΔG_r (eV)	E_a (eV)	ΔE_r (eV)	k_f (s^{-1})	K
R22	$C_6H_4O_5^* + H_2O^* \rightleftharpoons C_6H_4O_5$ (g) $+ * + H_2O^*$		-0.38		0.78	1.11×10^{14}	7.30×10^4
Pathway CII-OH							
R23	$C_6H_4O_4^* + {}^*OH \rightleftharpoons C_5H_3O_3CHOOH^*$	0.17	-0.19	0.27	-0.29	5.99×10^{10}	2.34×10^2
R24	$C_5H_3O_3CHOOH^* + {}^*OH \rightleftharpoons C_6H_4O_5^* + H_2O^*$	0.49	-0.74	0.72	-0.53	4.78×10^6	2.66×10^9
R25	$C_6H_4O_5^* + H_2O^* \rightleftharpoons C_6H_4O_5$ (g) $+ * + H_2O^*$		-1.01		0.02	1.55×10^{22}	1.02×10^{13}
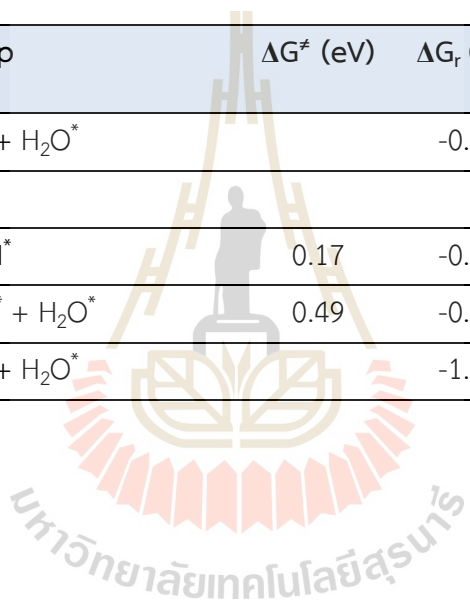
4.3.4 Oxygen vacancy formation energy on β–MnO$_2$ (110) surface

Active surface oxygen is essential in the HMF oxidation if the catalyst surface has low hydroxyl group coverage. We found that the C-H bond breaking of acetal and hemiacetal-like structures has an oxygen vacancy (V$_O$*) formation simultaneously occurring on the surface (R3, R10, R14, and R21). The low oxygen vacancy formation energy results in a strong oxidizing ability and facilitates the detachment of oxygen atoms from the surface of the catalyst. Therefore, we have calculated the oxygen vacancy formation energy on the bare and hydroxylated surface. The energy of oxygen vacancy formation, E$_{VO}$, can be calculated from the following equation.

$$E_{VO} = E_{O-vacancy} + \frac{1}{2}E_{O_2} - E_{perfect}$$

where $E_{O-vacancy}$ and $E_{perfect}$ are the calculated total energies of the surface with one oxygen vacancy and the perfect surface, respectively. E_{O_2} is the total energy of an isolated O$_2$ molecule.
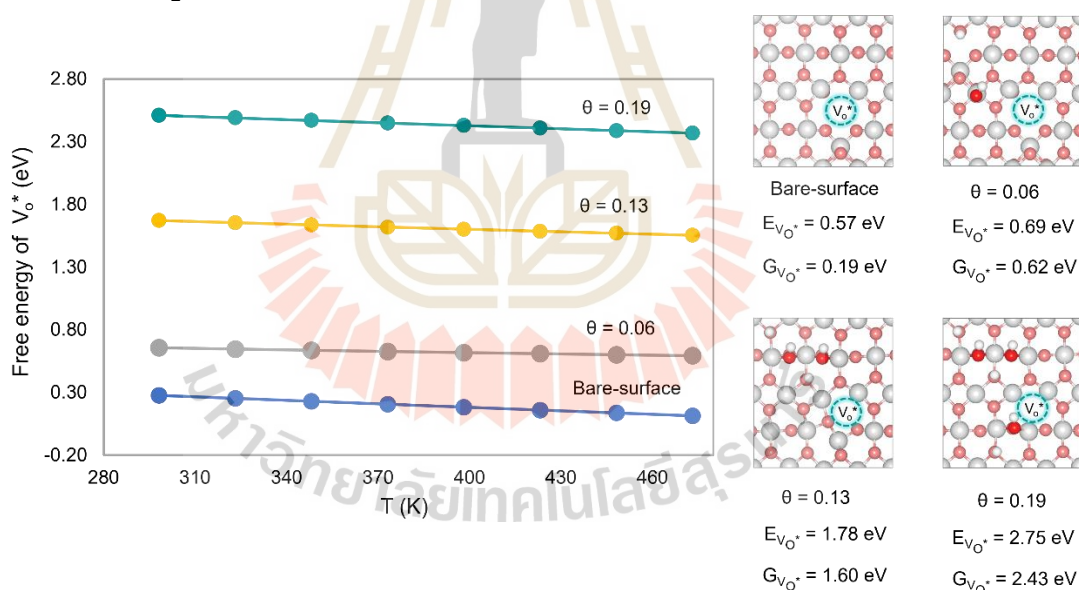
Figure 4.9 Free energy of oxygen vacancy formation (G$_{VO}$*) versus temperature (T) and the most stable structure of each vacancy formation model on bare- and hydroxylated β–MnO$_2$ (110) surfaces (G$_{VO}$* at 393 K).

The result reveals that the oxygen vacancy formation energy on a bare surface (G$_{VO*}$ = 0.19 eV) is lower than on a hydroxylated surface. Increasing OH coverage on the surface (0.06 to 0.19) leads to the increase of V$_O$* energy. Moreover, the free energy of V$_O$* slightly decreases at elevated temperatures, as shown in

Figure 4.9. This result indicates oxygen vacancy formation on the bare surface is easier than that on a hydroxylated surface. The C-H bond breaking of hemiacetal-like structure at TSC4 ($\Delta G^{\neq}$=1.01 eV) via R21 has an energy barrier higher than the TSC2 ($\Delta G^{\neq}$=0.67 eV) via R14. TSC4 of pathway Cl-OH associates surface oxygen formation near the OH site resulting in the higher $\Delta G^{\neq}$ value than TSC2 of pathway C, that the surface oxygen formation is easier.

The result agrees well with oxygen vacancy formation energy of the β–MnO_2 lattice, approximately 0.6 eV, reported in the previous theoretical work (Yao and Wang, 2021) indicating good oxidative ability of this catalyst. Third, the HMF* oxidation through DFF* is favorable on bare β–MnO_2(110) surface. This result agrees well with our experimental part that DFF is the main product when using -OH free solvent such as DMSO. Finally, oxidizing DFF to FFCA in the R10 step is likely to be the rate determining step due its high energy barrier. This aspect is controversial with our experimental results in latter session and other work that the FFCA to FDCA is the most difficult step of the reaction in aqueous solution. The mechanistic study over bare surface can describe the systems with no hydroxyl group on the catalysts' surface such as -OH free solvent or -OH free base, as evidenced in our experiments.

4.3.5 Electronic charge analysis

Bader charges (Henkelman, Arnaldsson et al. 2006) of selected configurations were calculated to understand the local charge properties around the active sites as shown in **Figure 4.10**. The negative and positive values represent the partial negative charge via electron incretion and the partial positive charge via electron depletion, respectively. The C-H bond breaking at the formyl group is difficult for HMF oxidation. We found that the C-H bond breaking of DFF (acetal form) is the rate-limiting step on a bare surface. Bader charges analysis reveals that the carbon atom (C6) of TSB3 has a positive charge (+0.85) higher than TSA1 (+0.73) through pathway A-bare, as shown in **Figure 4.10**. It means that at the transition state of C-H bond breaking via TSB3 (1.28 eV) (pathway B-bare) is easier than TSA1 (1.51 eV), leading to prefer pathway B-bare more than pathway A-bare. The C3 of hemiacetal-like on a hydroxylated surface via TSB8 (0.40 eV) (pathway B-OH) has a net atomic charge (+1.02) higher than C6

(+0.85) of acetal form via TSB3 on a bare surface. The result suggests that a C-H bond breaking of hemiacetal-like on a hydroxylated surface (TSB8: 0.40 eV) is easier than breaking acetal on bare surfaces (TSB3: 1.28 eV), promoting the HMF-DFF-FFCA path.

       For FFCA oxidation, the C-H bond breaking of hemiacetal-like at TSC2 via the C-bare path has a charge at C3 (+1.01), which is higher than C3 (+0.97) at TSC4 via CI-OH pathway. In addition, surface oxygen is a strong active species (net atomic charge: -0.96), promoting the dehydrogenation process. This result reveals that a C-H bond breaks of hemiacetal structure and simultaneous occurrence of oxygen vacancy on the surface prefer the C-bare path (TSC2: 0.67 eV) more than the CI-OH path (TSC4: 1.01 eV). Note that the net atomic charge at C3 of the hemiacetal intermediate ($C_5H_3O_3CHOH^*$) via the CII-OH path is +0.98 more than at C3 of $C_5H_3O_3CHOH^*$ at C-bare (+0.87) and CI-OH path (+0.88). This result suggests that hemiacetal-like without V_O^* promotes FFCA oxidation on a high OH coverage surface. The occurrence of oxygen vacancy on a high hydroxylated surface may be unfavorable for FFCA oxidation. As we suggest, the oxygen vacancy formation energy on the hydroxylated surface is 2.10 eV, higher than the bare surface (0.57 eV).
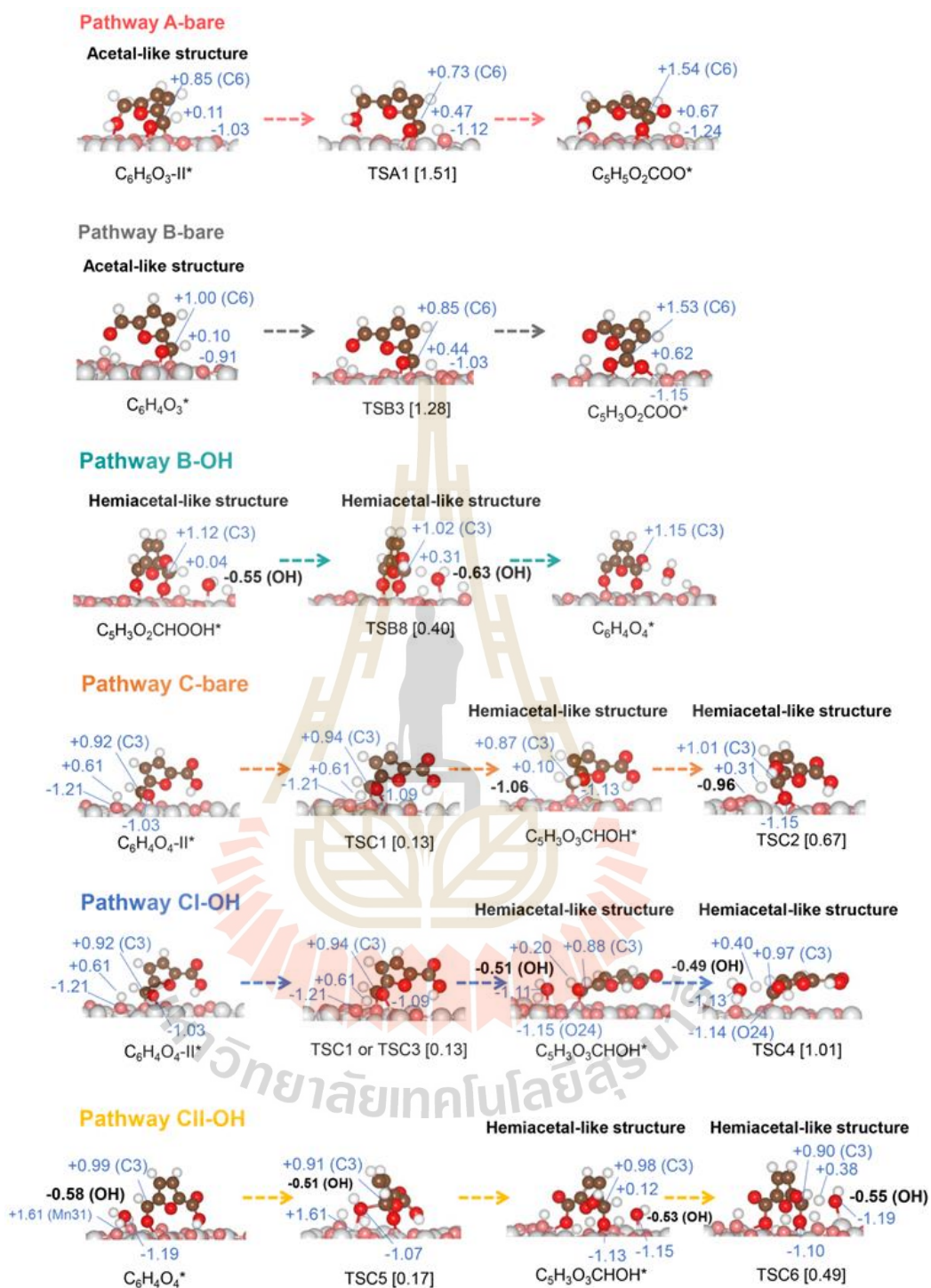
Figure 4.10 Bader charge analyses of selected steps of HMF oxidation on bare and hydroxylated surfaces. The activation barriers (in eV) are given in square brackets.

4.3.6 Microkinetic analysis

The free energy profiles obtained from DFT calculations provide thermochemical data and suggest the favorable pathway by comparing the energy barriers and the stability of the intermediates. Our results from the previous section (section 4.4.2 and 4.4.3) suggest that the HMF oxidation on β–MnO_2(110) prefers the DFF intermediate pathway, and the hydroxyl group plays the decisive role on the reaction. However, we cannot deduce the most active surface from DFT energies alone since the relative rates on these surfaces depends on the reaction conditions. Therefore, we used microkinetic models to predict the reaction rate, apparent activation energy (E_{app}), and rate-determining steps under applied temperature of reactant molecules.

Here, we comparatively conduct microkinetic simulation of the HMF oxidation on bare surface and hydroxylated surface to understand the kinetics of the overall reaction and also elementary reaction steps. All considered elementary steps of HMF oxidation and corresponding rate equations are listed in **Table 4.1** The simulations are performed at the steady-state approximation. The calculation results of four microkinetic models via particular pathways, which are MKM-I, MKM-II, MKM-III and MKM-IV, are given in **Table 4.5** The simplified scheme of catalyst surface evolution in each model is **Figure 4.4** MKM-I presents the HMF oxidation on the bare surface considering the elementary steps of pathways A-bare, B-bare and C-bare. Other three models compare the hydroxylation effect by varying the possible pathways of the HMF-DFF-FFCA and FFCA-to-FDCA steps of the hydroxylated surfaces. MKM-II consisted of pathways B-OH and C-bare can represent low OH coverage model. MKM-III consisted of pathways B-OH and CI-OH, and MKM-IV consisted of pathways B-OH and CII-OH represent the high OH coverage. On the other hand, MKM-II and MKM-IV can also describe the important role of active surface oxygen in FFCA oxidation via C-bare and CI-OH paths, respectively.

As a result, the calculated the reaction rate of each kinetic model is given **Table 4.5** MKM-I reveals that the rate of HMF oxidation through the HMF-DFF-FFCA path (2.96×10^{-4} s^{-1}) is significantly higher than the HMF-HMFCA-FFCA path (4.74×10^{-20} s^{-1}) on a bare surface. We further calculated the degree of rate control ($X_{RC, i}$) and the

thermodynamic rate control ($X_{TRC, i}$) to reveal the rate-determining step of HMF oxidation on the bare surface. According to our calculation, the dehydrogenation at the formyl group of DFF* has the highest degree of rate control ($X_{RC, R10}$ = 0.84), noticeably higher than the following hydrogenation step ($X_{RC, R11}$ = 0.16). **Figure 4.11a** shows the $X_{RC, R10}$ value slightly increases with the temperature rising (280 K – 480 K), while $X_{RC, R11}$ slightly decreases. However, the value of $X_{RC, R10}$ and $X_{RC, R11}$ is not significantly increase or decrease. We can infer that the C–H bond breaking at the formyl group of DFF* is the rate-limiting step with the E_{app} of 1.27 eV on a bare surface. Graph the natural logarithm of the reaction rate (in s^{-1}) of HMF oxidation as a function of 1/T (in K^{-1}) and the calculated apparent activation energy (E_{app}) of each microkinetic model, as shown in **Figure 4.12**. This corresponds well with the degrees of thermodynamic rate control ($X_{TRC, DFF*}$ = -0.84, $X_{TRC, C5H3O2COO*}$ = -0.16) and the coverages of DFF* (0.84 ML) and $C_3H_3O_2COO*$ (0.16 ML) that predominate the surface (**Figure 4.11b and 4.11c**). DFF is the This result reveals that DFF oxidation to FFCA is the most difficult step and DFF intermediate can be observed as the majority on the non-hydroxylated surface. This result agrees with our experiment that predominant product when using DMSO as a solvent (see **Table 4.6**).

Next, MKM-II considers the effects of both hydroxyl group and surface oxygen toward the HMF-DFF-FFCA and FFCA-to-FDCA, respectively. Such mechanisms may occur at low OH coverages where the HMF-to-FFCA oxidation takes place with the help of hydroxyl group while the oxidation of FFCA to FDCA occurs via surface oxygen. The rate-determining step changes from the oxidation of DFF to the oxidation of FFCA when the hydroxyl group presents – the $X_{RC, R14}$ of C–H bond breaking via TSC2 is equal to 1, as shown in **Table 4.5** and **Figure 4.11d.** The key intermediates are those in the FFCA-to-FDCA pathways – $X_{TRC, FFCA*}$ = -0.20, $X_{TRC, C5H3O3CHOH*}$ = -0.80. In **Figure 4.11e**, $X_{TRC, FFCA*}$ decreases with the temperature rising, and $X_{TRC, C5H3O3CHOH*}$ gradually increases. **Figure 4.11f**, the most catalytic site is occupied by FFCA* specie at high temperatures. This result suggests that the oxidation of FFCA to FDCA is a difficult step at low OH coverages. The overall rate of this model increases to 1.82×10^4 s^{-1}, while the E_{app} value decreases to 0.76 eV

compared to those of MKM-I suggesting that the presence of OH even at low coverages improves kinetics of HMF-to-FDCA reaction.

At high OH coverages, the reaction could take place via MKM-III or MKM-IV models. Both microkinetic models consider the effect of OH on HMF-DFF-FFCA oxidation (pathways B-OH); where MKM-III deals with surface oxygen at late oxidation of FFCA to FDCA (pathway CI-OH) while MKM-IV only focuses on the OH as oxidizing species through the mechanism (pathway CII-OH). Computations reveal that MKM-III exhibits significantly lower rate than that of MKM-II (4.83×10^{-1} vs 1.82×10^{4} s^{-1}) with greater apparent activation energies (0.94 vs 0.76 eV). This indicates that the reaction is quite sluggish when the oxidation involves surface oxygen at high OH coverages with the rate-limiting step at the C–H bond activation of hemiacetal-like intermediate ($X_{RC, R21} = 1$) similar to that of MKM-II model. **Figure 4.11g** shows the $X_{RC, R21}$ is not changed with the temperature rising from 280 K to 480 K. These intermediates also predominate the catalytic process with the degree of thermodynamic rate control of FFCA* and $C_5H_3O_2CHOH^*$ equal to -0.44 and -0.56, respectively. We found that the value of $X_{TRC, FFCA*}$ increases and $X_{TRC, C5H3O2CHOH*}$ decreases at high temperatures, as shown in **Figure 4.11h**. In **Figure 4.11i**, the surface is occupied by FFCA* at low temperature, and then the coverage of FFCA* rapidly reduces at high temperature due to the increase of hemiacetal-like species. The results suggests that the concentrations of hemiacetal-like species are dominant on a hydroxylated surface at a high temperature.

The kinetics becomes much faster when the oxidizing species is solely OH on the surface. As presented by MKM-IV, the overall rate is hastened by 7 orders of magnitude when compared with that of MKM-III with the same rate-limiting step of C–H bond breaking ($X_{RC, R24} = 0.87$) to form hemiacetal-like intermediate ($X_{TRC, C5H3O3CHOH*} = -0.88$). The apparent activation energy is consistently reduced to 0.50 eV when the oxidation of FFCA to FDCA is assisted by OH species. **Figure 4.11j** shows the trend of $X_{RC, R24}$ value decreases rapidly above 400 K while $X_{RC, R1}$ quickly increases. This result suggests that the HMF adsorption step (R1) plays a more role, and it becomes the eventual rate-limiting step at high temperatures. In addition, $X_{TRC, C5H3O3CHOH*}$ value increases rapidly above 400 K, as shown in **Figure 4.11k**. **Figure 4.11l**

displays the coverages of hemiacetal-like species ($C_5H_3O_3CHOH^*$) decrease with the temperature increasing. In addition, we found that the number of empty sites (*) increases at high temperatures, which occurs from getting less adsorption of the HMF molecule.

In summary, our kinetics analyses assure that the DFF path is preferable than the HMFCA path. The DFF-to-FFCA and FFCA-to-FDCA are the rate determining steps on the bare and hydroxylated surface, respectively. These aspects are consistent with the results in **Table 4.6** in the experiment section. The kinetic properties clearly suggest that OH promotes HMF oxidation, while the surface oxygen also plays a role in the low OH coverage. Both active oxygen species (i.e. OH and surface oxygen) are crucial to promote the FFCA oxidation reaction.
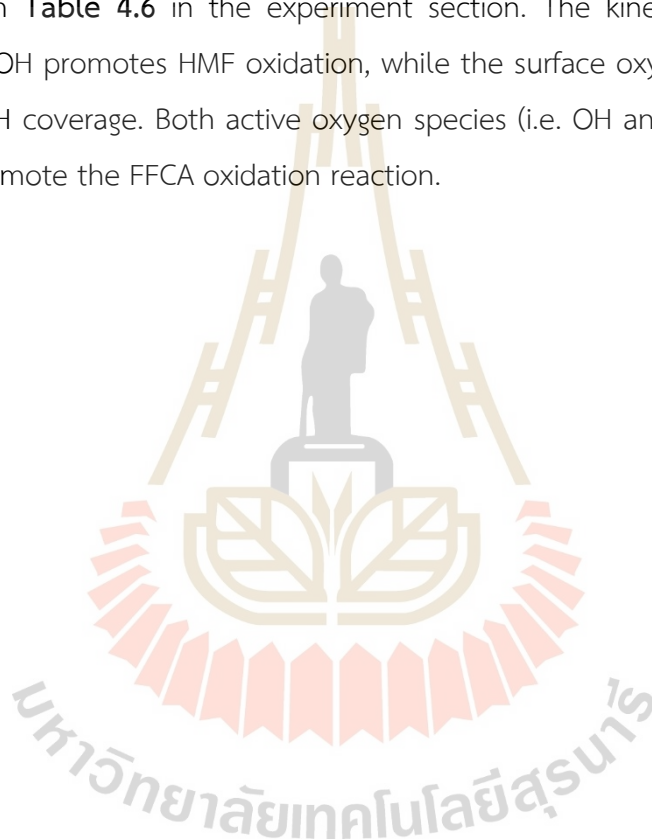
Table 4.5 Calculated the reaction rate (s^{-1}), apparent activation energy (E_{app}), degree of rate control (X_{RC}), and degree of thermodynamic rate control (X_{TRC}) for HMF oxidation on bare and hydroxylated β–MnO$_2$(110) surfaces obtained from microkinetic analysis at 393 K.

MKM	OH coverage	Rate (s^{-1})				E_{app} (eV)	X_{RC}	X_{TRC}	
		HMFCA path	DFF path	FFCA path	Overall rate				
I	no	4.74×10^{-20}	2.96×10^{-4}	2.96×10^{-4}	2.96×10^{-4}	1.27	DFF→FFCA (R10=0.84, R11=0.16)	DFF* $C_5H_3O_2COO^*$	= −0.84 = −0.16
II	low	4.66×10^{-15}	1.82×10^{4}	1.82×10^{4}	1.82×10^{4}	0.76	FFCA→FDCA (R14=1.00)	FFCA* $C_5H_3O_3CHOH^*$	= −0.20 = −0.80
III	high	1.24×10^{-19}	4.83×10^{-1}	4.83×10^{-1}	4.83×10^{-1}	0.94	FFCA→FDCA (R21=1.00)	FFCA* $C_5H_3O_2CHOH^*$	= −0.44 = −0.56
IV	high	1.06×10^{-12}	4.13×10^{6}	4.13×10^{6}	4.13×10^{6}	0.54	HMF-Ads (R1=0.06) DFF→FFCA (R19=0.07) FFCA→FDCA (R24=0.87)	$C_5H_3O_2CHOOH^*$ $C_5H_3O_3CHOH^*$	= −0.06 = −0.88
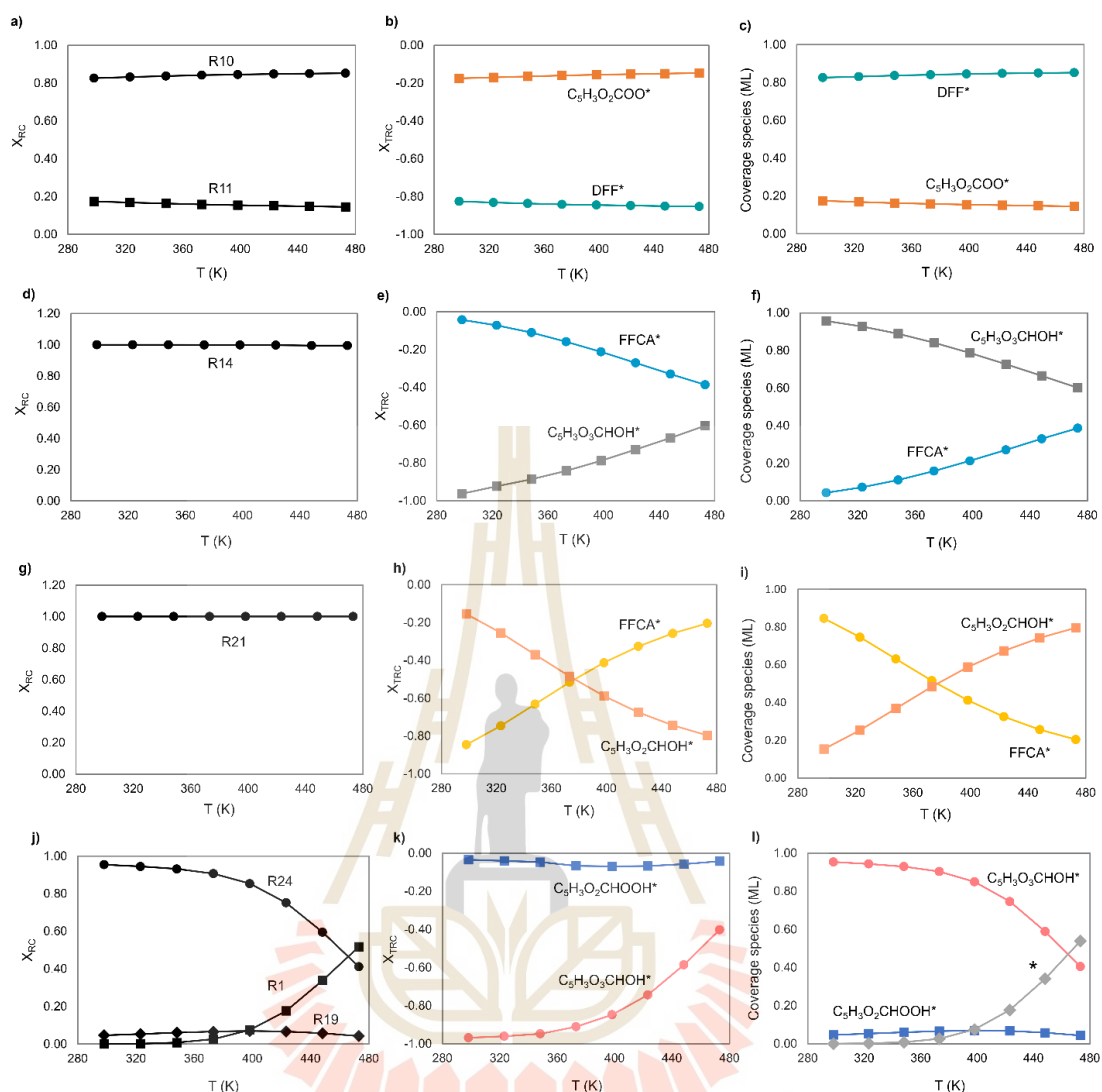
Figure 4.11 The primary Campbell's degree of rate control ($X_{RC, i}$), the degree of thermodynamic rate control ($X_{TRC, i}$), and the primary intermediate coverage versus temperature (in K) of HMF oxidation in MKM-I (a, b, and c), MKM-II (d, e, and f), MKM-III (g, h, and i), and MKM-IV (j, k, and l), respectively.
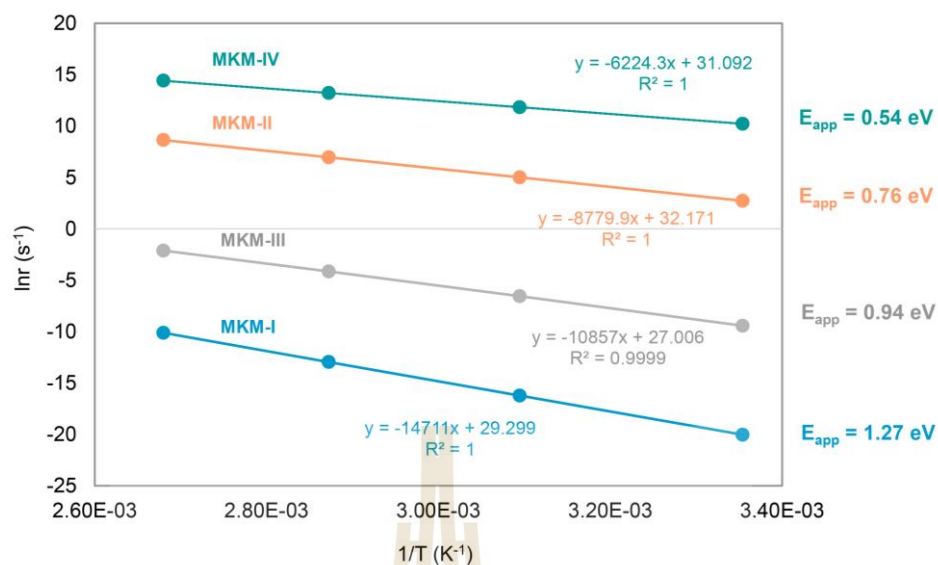
Figure 4.12 The natural logarithm of reaction rate (in s^{-1}) of HMF oxidation as a function of $1/T$ (in K^{-1}) and the calculated apparent activation energy (E_{app}) of each microkinetic model.

4.3.7 Catalytic performance of the synthesized catalyst

In this section, Dr. Kajornsak Faungnawakij et al., have studied the aerobic oxidation of HMF on the synthesized β–MnO_2 catalyst, which was conducted by experiment to understand the factors that influence the catalytic performance of this catalyst. First, the synthesized MnO_2 catalyst was characterized to confirm the β–MnO_2 phase formation. Phase transformation of the manganese (IV) oxide was revealed by XRD results as shown in **Figure 4.13a**. It is seen that the β–MnO_2 powder (crystallite size ~7 nm) was successfully obtained by ball-milling and calcination of the commercially available γ–MnO_2 powder. The morphology of the as-synthesized β–MnO_2 is presented by SEM image as shown in **Figure 4.13b** with flake-like and rod-like particles. The specific surface area and pore volume of the β–MnO_2 sample were 50 m^2/g and 0.19 mL/g, respectively.
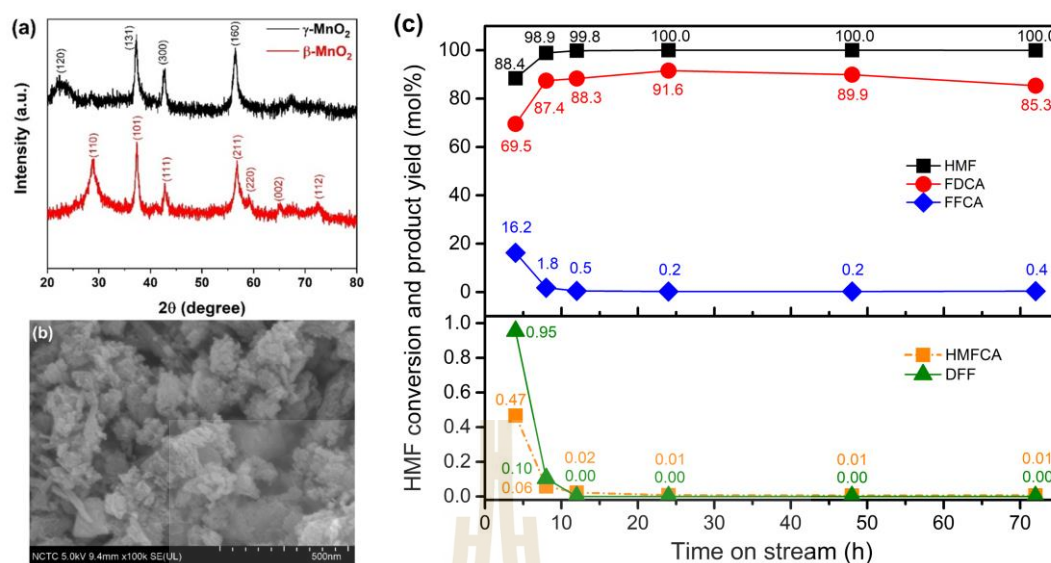
Figure 4.13 (a) XRD patterns of the synthesized β–MnO$_2$ powder compared with that of the commercially available γ–MnO$_2$ powder (starting material), (b) SEM image of β–MnO$_2$, and (c) continuous flow oxidation of HMF over β–MnO$_2$ catalyst. Reaction conditions: β–MnO$_2$ (4 mL), HMF in DI water (40 mM), NaHCO$_3$ (3 equity with respect to HMF), pO_2 (1 MPa), 393 K and LHSV of 1 h^{-1}.

Next, the catalytic performance of the synthesized catalyst was investigated. **Figure 4.13c** shows the representative data of continuous flow oxidation reaction of HMF over β–MnO$_2$ catalyst under LHSV of 1 h^{-1} regarding the changes of HMF, HMFCA, DFF, FFCA and FDCA for 72 h time-on-stream. Since 8 h time-on-stream, the conversion of HMF is stable with ≥ 99 mol% while 85.3-91.6 mol % FDCA yield could be retained until 3 days reaction time, showing an excellent stability of this catalyst under certain conditions.

4.3.8 Continuous flow oxidation of HMF over the synthesized β–MnO$_2$ catalyst

Dr. Kajornsak Faungnawakij et al., have studied the reproducibility test (**Figure 4.14**) was also accomplished to ensure that an above 85% yield of FDCA could be achieved under the current reaction system. With the LHSV of 1 h^{-1}, traces of DFF and HMFCA intermediates (<1% yield) are found since 4 h time-on-stream with higher

rate of DFF production and rapidly consumed over time. It is anticipated that the pathway with DFF as the intermediate is more dominant than the HMFCA route in the current system. Subsequently, much slower consumption of FFCA into FDCA indicates that FFCA oxidation is the rate-determining step in HMF oxidation reaction.
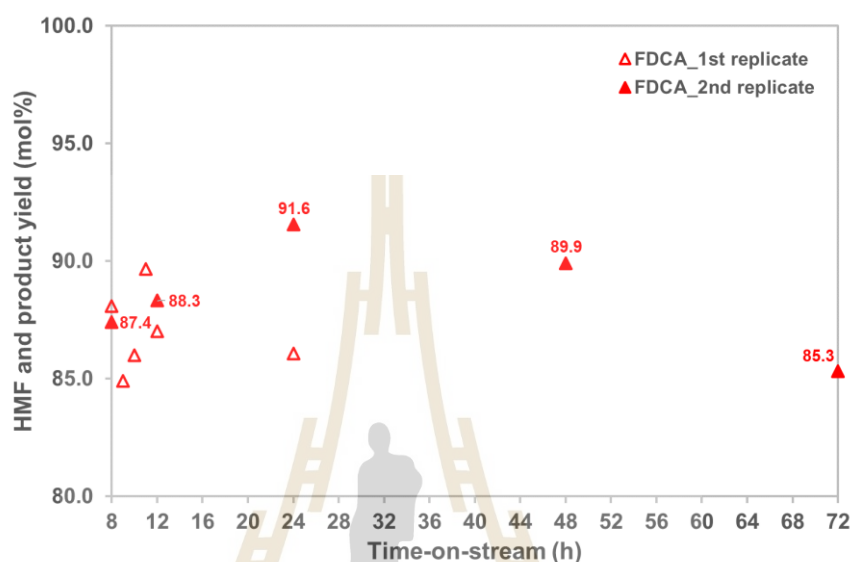
Figure 4.14 Continuous flow oxidation of HMF over β–MnO$_2$ catalyst: reproducibility test. Reaction conditions: β–MnO$_2$ (4 mL), HMF in DI water (40 mM), NaHCO$_3$ (3 equiv with respect to HMF), pO_2 (1 MPa), 393 K and LHSV of 1 h^{-1}.

Liguori et al. (Liguori, Barbaro et al., 2019) demonstrated that the progression of those intermediates is more obvious when the residence time of substrate is decreased (i.e., LHSV is increased) since lower conversion of HMF is in general observed at higher LHSV. Thus, we increased the LHSV from 1 to 4 h^{-1} and found that DFF yield at steady state is clearly higher than that of HMFCA. FFCA appears as the main intermediate, confirming the rate-determining step in accordance with those experiments performed with LHSV of 1 h^{-1} (**Figure 4.15**).
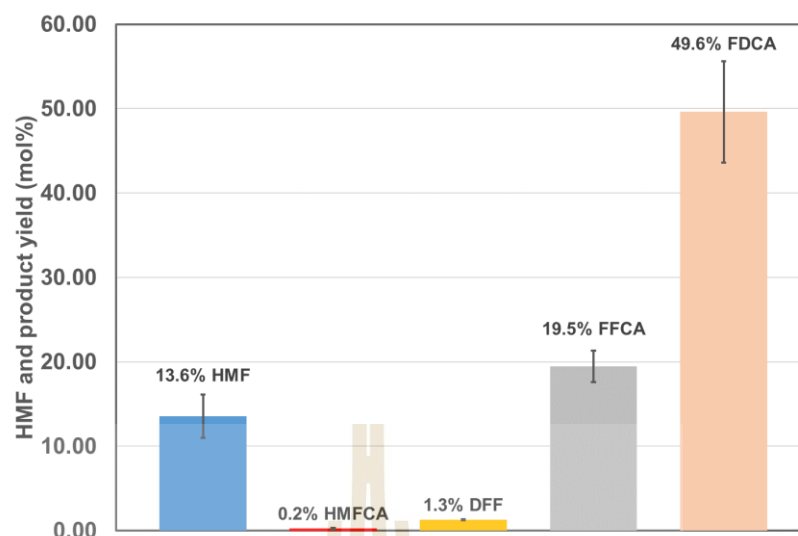
Figure 4.15 Continuous flow oxidation of HMF over β–MnO$_2$ catalyst: Reaction conditions: β–MnO$_2$ (1 mL), HMF in DI water (40 mM), NaHCO$_3$ (3 equiv with respect to HMF), pO$_2$ (1 MPa), 393 K and LHSV of 4 h^{-1}. Average value over 6-10 h time-on-stream (steady state).

4.3.9 Oxidation of HMF using a batch reactor over the synthesized β–MnO$_2$ catalyst

In this section, Dr. Kajornsak Faungnawakij et al., have studied the catalytic oxidation of HMF to FDCA over the as-synthesized β–MnO$_2$ powder investigated using a batch reactor also provide similar observation to that of continuous flow system (**Figure 4.16**). The procedure for catalytic efficiency testing of the obtained β–MnO$_2$ was adapted from Hayashi et al.(Hayashi, Yamaguchi et al., 2019) The HMF oxidation was carried out in a 100 mL stainless steel autoclave reactor with a 30 mL Teflon liner containing a magnetic stirring bar. Typically, HMF (1.2 mmol), β–MnO$_2$ powder (300 mg), NaHCO$_3$ (3.6 mmol), water (30 mL), and O$_2$ (2 MPa) were charged into the autoclave reactor. The reaction solution was heated to 393 K. The solution sampling was started at which the temperature reached set point and collected continually to monitor the progress of reaction. The sampled solution was filtered using 0.22 uM pore size membrane filter and the filtrate was diluted 10 times with water. The formation of FDCA and their intermediates and the decreasing of HMF were investigated using the high-performance liquid chromatography (HPLC, Shimadzu),

with a UV detector adjusted to 260 nm for analysis of FDCA and HMFCA and to 280 nm for analysis of HMF, FFCA and DFF, using an Aminex HPX-87H ion-exchange column (300 mm in length with a 7.8 mm i.d.; Bio-Rad, Hercules, CA, USA). The column temperature was set at 318 $^{\circ}$C. The samples were eluted with 5 mM sulfuric acid solution in DI water at a flow rate of 0.6 mL/min.

Figure 4.16 shows the progress of reaction regarding the changes of HMF, HMFCA, DFF, FFCA and FDCA over time. It is seen that DFF and HMFCA intermediates were occurred since 0 hour (i.e., when the temperature reached set point), indicating that reaction pathway from HMF to FFCA occurred through both DFF and HMFCA in the current system. The yields of those intermediates reach their maxima at 4 h for DFF (~3.7%) and 8 h for HMFCA (~3.3%), showing higher rate of DFF production at the beginning. Additionally, DFF which was subsequently oxidized into FFCA are completely consumed before HMFCA, indicating that the pathway with DFF as the intermediate is more dominant than the HMFCA route in the current system. The produced FFCA is gradually increased against reaction time with an increasing of FDCA. After 24 h, the decreasing of FFCA is observed with continuous increasing of FDCA until 45 h at which the FFCA is almost used up whereas the FDCA yield reaches its maximum at ~60%, suggesting that the oxidation of FFCA to FDCA is the rate-determining step.
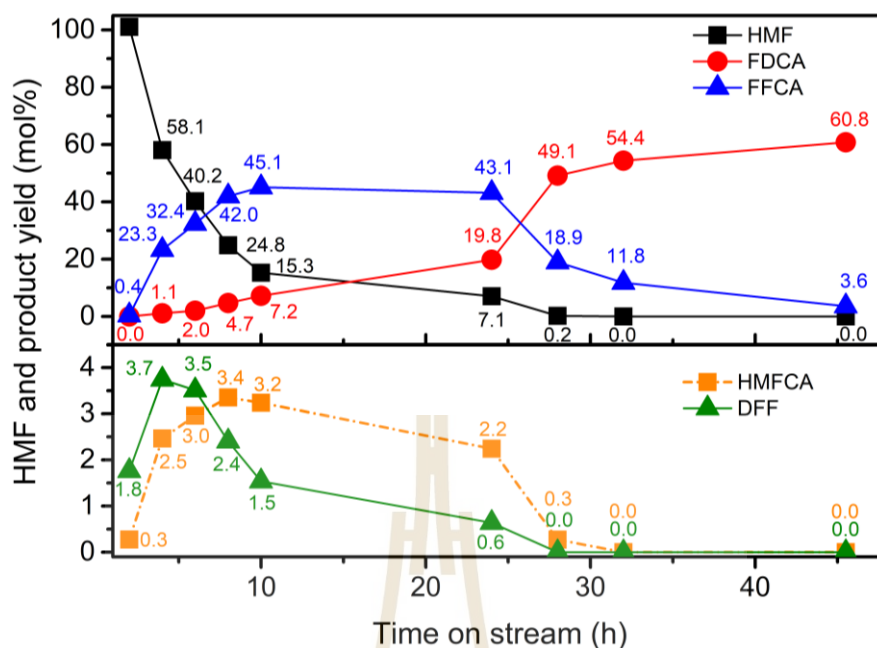
Figure 4.16 Time course for the oxidation of HMF into FDCA catalyzed by β–MnO$_2$. Reaction conditions: HMF (1.2 mmol), β–MnO$_2$ powder (300 mg), NaHCO$_3$ (3.6 mmol), water (30 mL), and pO$_2$ (2 MPa), 393 K. The dash lines in the figure are only to guide the eye.

4.3.10 The role of hydroxyl group for HMF oxidation reaction

To understand the role of hydroxyl group proposed in our simulation part, Dr. Kajornsak Faungnawakij et al., was studied the HMF oxidation over bare β–MnO$_2$ surface by changing the solvent from DI water to DMSO. As shown in **Table 4.6**, the HMF conversion of ≥99 mol% is obtained both in water and DMSO systems. The selectivity of FDCA is highest (~89 mol%) in case of water while DFF is preference in DMSO with ~51% selectivity under the same reaction conditions. By using DMSO, the HMFCA intermediate is not detected. These results are in good agreement with our computational investigation that the HMF oxidation reaction prefers the DFF route than the HMFCA route and DFF becomes the main product on the non-hydroxylated β–MnO$_2$(110) surface. In addition, comparing the FDCA yield of the HMF oxidation reaction in water and DMSO reveal that HMF oxidation in water has more FDCA yield than DMSO. This aspect supports our DFT and microkinetic results that the OH group might promote the HMF oxidation reaction. To confirm that the aerobic oxidation

reaction of HMF prefers the DFF path more than HMFCA and suggest that the hydroxyl group is vital to increase FDCA yield.

Table 4.6 Effect of solvents on the selective oxidation of HMF into FDCA.

Solvent	HMF conversion (%)	Selectivity (%)				FDCA yield (%)	DFF yield (%)
		FDCA	FFCA	HMFCA	DFF		
Water	99.4	89.3	0.5	< 0.1	< 0.1	89.8	< 0.1
DMSO	99.0	1.2	22.9	N/A	51.3	1.2	51.7

Reaction conditions: β–MnO_2 (4 mL), HMF in DI water (40 mM), $NaHCO_3$ (3 equiv. with respect to HMF), pO_2 (1 MPa), 393 K, LHSV of 1 h^{-1}, and 8 h time-on-stream.

4.4 Conclusions

In summary, theoretical and experimental results in this work help clarify the role of hydroxyl group on the HMF oxidation in β–MnO_2. Our findings reveal that the DFF path is preferable than the HMFCA path in β–MnO_2. The calculations signify that both OH and surface oxygen play decisive roles on the HMF oxidation process over the β–MnO_2 surface. Third, the calculations suggest that the C–H bond breaking at the formyl group of DFF by the surface oxygen is the rate-determining step on non-hydroxylated surface. DFF is more selective than FFCA and FDCA in this catalytic model. The calculated results agree well with the key product found from the HMF oxidation in DMSO in experiment, which represents the non-hydroxylated model. Finally, the hydroxyl group from water and other sources (i.e. bases or solvents) can promote the FDCA production from HMF via facilitating the C–H activation and OH insertion. The FFCA oxidation becomes the rate-limiting step over the hydroxylated β–MnO_2 surface which is consistent with our experiment. These insights provide a good guidance for enhancing catalytic performances of metal oxides and other catalysts for the HMF to FDCA reaction

4.5 References

Ait Rass, H., Essayem, N., and Besson, M. (2013). Selective aqueous phase oxidation of 5-hydroxymethylfurfural to 2,5-furandicarboxylic acid over Pt/C catalysts: influence of the base and effect of bismuth promotion. *Green Chem., 15,* 2240-2251.

Ait Rass, H., Essayem, N., and Besson, M. (2015). Selective aerobic oxidation of 5-HMF into 2,5-furandicarboxylic acid with Pt catalysts supported on TiO_2- and ZrO_2-based supports. *ChemSusChem., 8,* 1206-1217.

Aono, R., Hayashi, E., Yamaguchi, Y., Kamata, K., and Hara, M. (2020). Template-free synthesis of mesoporous beta-MnO_2 nanoparticles: Structure, formation mechanism, and catalytic properties. *ACS Appl. Mater. Interfaces., 12,* 36004-36013.

Blöchl, P.E. (1994). Projector augmented-wave method. *Phys. Rev. B., 50,* 17953-17979.

Cai, Ma, H., Zhang, J., Song, Q., Du, Z., Huang, Y., and Xu, J. (2013). Gold nanoclusters confined in a supercage of Y zeolite for aerobic oxidation of HMF under mild conditions. *Chem. Eur. J., 19,* 14215-14223.

Campbell, C.T. (2017). The degree of rate control: A powerful tool for catalysis research. *ACS Catal., 7,* 2770-2779.

Casanova, Iborra, S., and Corma, A. (2009). Biomass into chemicals: Aerobic oxidation of 5-hydroxymethyl-2-furfural into 2,5-furandicarboxylic acid with gold nanoparticle catalysts. *ChemSusChem., 2,* 1138-1144.

Chen, C., Wang, L., Zhu, B., Zhou, Z., El-Hout, S.I., Yang, J., and Zhang, J. (2021). 2,5-Furandicarboxylic acid production via catalytic oxidation of 5-hydroxymethylfurfural: Catalysts, processes and reaction mechanism. *J. Energy Chem., 54,* 528-554.

Cheng, F., Guo, D., Lai, J., Long, M., Zhao, W., Liu, X., and Yin, D. (2021). Efficient base-free oxidation of 5-hydroxymethylfurfural to 2,5-furandicarboxylic acid over copper-doped manganese oxide nanorods with tert-butanol as solvent. *Front. Chem. Sci. Eng., 15,* 960–968.

Davis, S.E., Zope, B.N., and Davis, R.J. (2012). On the mechanism of selective oxidation of 5-hydroxymethylfurfural to 2,5-furandicarboxylic acid over supported Pt and Au catalysts. *Green Chem., 14,* 143-147.

Deshan, A.D.K., Atanda, L., Moghaddam, L., Rackemann, D.W., Beltramini, J., and Doherty, W.O.S. (2020). Heterogeneous catalytic conversion of sugars Into 2,5-furandicarboxylic acid. *Front. Chem., 8,* 659.

Gao, T., Yin, Y., Zhu, G., Cao, Q., and Fang, W. (2020). Co_3O_4 NPs decorated Mn-Co-O solid solution as highly selective catalyst for aerobic base-free oxidation of 5-HMF to 2,5-FDCA in water. *Catal. Today., 355,* 252-262.

Gawade, A.B., Nakhate, A.V., and Yadav, G.D. (2018). Selective synthesis of 2, 5-furandicarboxylic acid by oxidation of 5-hydroxymethylfurfural over $MnFe_2O_4$ catalyst. *Catal. Today., 309,* 119-125.

Grimme, S., Antony, J., Ehrlich, S., and Krieg, H. (2010). A consistent and accurate ab initio parametrization of density functional dispersion correction (DFT-D) for the 94 elements H-Pu. *J. Chem. Phys.,* 132, 154104.

Hayashi, E., Komanoya, T., Kamata, K., and Hara, M. (2017). Heterogeneously-catalyzed aerobic oxidation of 5-hydroxymethylfurfural to 2,5-furandicarboxylic acid with MnO_2. *ChemSusChem., 10,* 654-658.

Hayashi, E., Oba, F., Yamaguchi, Y., Kamata, K., Tsunoda, N., Kumagai, Y., and Hara, M. (2019). Effect of MnO_2 crystal structure on aerobic oxidation of 5-hydroxymethylfurfural to 2,5-furandicarboxylic acid. *J. Am. Chem. Soc., 141,* 890-900.

Hayashi, E., Yamaguchi, Y., Kamata, K., Tsunoda, N., Kumagai, Y., Oba, F., and Hara, M. (2019). Effect of MnO_2 crystal structure on aerobic oxidation of 5-hydroxymethylfurfural to 2,5-furandicarboxylic acid. *J. Am. Chem. Soc., 141,* 890-900.

Henkelman, G., Arnaldsson, A., and Jónsson, H. (2006). A fast and robust algorithm for Bader decomposition of charge density. *Comput. Mater. Sci., 36,* 354-360.

Henkelman, G., and Jónsson, H. (1999). A dimer method for finding saddle points on high dimensional potential surfaces using only first derivatives. *J. Chem. Phys., 111,* 7010-7022.

Henkelman, G., and Jónsson, H. (2001). Long time scale kinetic Monte Carlo simulations without lattice approximation and predefined event table. *J. Chem. Phys., 115,* 9657-9666.

Jin, Y., Sarina, S., Liu, H., Martens, W., Waclawik, E.R., Peiris, E., Jia, J., Shang, J., Kou, L., Guo, C., and Zhu, H.-Y. (2022). Aerobic oxidation of 5-hydroxymethyl-furfural to 2,5-furandicarboxylic acid at 20 °C by optimizing adsorption on AgPd alloy nanoparticle catalysts. *ACS Catal., 12,* 11226-11238.

Kim, M., Su, Y., Fukuoka, A., Hensen, E.J.M., and Nakajima, K. (2018). Aerobic oxidation of 5-(hydroxymethyl)furfural cyclic acetal enables selective furan-2,5-dicarboxylic acid formation with CeO_2-supported gold catalyst. *Angew. Chem. Int. Ed., 57,* 8235-8239.

Kohn, W., and Sham, L.J. (1965). Self-consistent equations including exchange and correlation effects. *Phys. Rev., 140,* A1133-A1138.

Kresse, G., and Furthmüller, J. (1996). Efficiency of ab-initio total energy calculations for metals and semiconductors using a plane-wave basis set. *Comput. Mater. Sci., 6,* 15-50.

Kresse, G., and Furthmüller, J. (1996). Efficient iterative schemes for ab initio total-energy calculations using a plane-wave basis set. *Phys. Rev. B., 54,* 11169-11186.

Kresse, G., and Joubert, D. (1999). From ultrasoft pseudopotentials to the projector augmented-wave method. *Phys. Rev. B., 59,* 1758-1775.

Liao, X., Hou, J., Wang, Y., Zhang, H., Sun, Y., Li, X., Tang, S., Kato, K., Yamauchi, M., and Jiang, Z. (2019). An active, selective, and stable manganese oxide-supported atomic Pd catalyst for aerobic oxidation of 5-hydroxymethylfurfural. *Green Chem., 21,* 4194-4203.

Liechtenstein, A.I., Anisimov, V.I., and Zaanen, J. (1995). Density-functional theory and strong interactions: Orbital ordering in Mott-Hubbard insulators. *Phys. Rev. B., 52,* R5467-R5470.

Liguori, F., Barbaro, P., and Calisi, N. (2019). Continuous-flow oxidation of HMF to FDCA by resin-supported platinum catalysts in neat water. *ChemSusChem., 12,* 2558-2563.

Lin, K.A., Oh, W.D., Zheng, M.W., Kwon, E., Lee, J., Lin, J.Y., Duan, X., and Ghanbari, F. (2021). Aerobic oxidation of 5-hydroxymethylfurfural into 2,5-diformylfuran using manganese dioxide with different crystal structures: A comparative study. *J. Colloid Interface Sci., 592,* 416-429.

Liu, Ma, H.-Y., Lei, D., Lou, L.-L., Liu, S., Zhou, W., Wang, G.-C., and Yu, K. (2019). Active oxygen species promoted catalytic oxidation of 5-hydroxymethyl-2-furfural on facet-specific Pt nanocrystals. *ACS Catal., 9,* 8306-8315.

Megías-Sayago, C., Lolli, A., Ivanova, S., Albonetti, S., Cavani, F., and Odriozola, J.A. (2019). Au/Al_2O_3 – Efficient catalyst for 5-hydroxymethylfurfural oxidation to 2,5-furandicarboxylic acid. *Catal Today., 333,* 169-175.

Mellan, T.A., Maenetja, K.P., Ngoepe, P.E., Woodley, S.M., Catlow, C.R.A., and Grau-Crespo, R. (2013). Lithium and oxygen adsorption at the **β**-MnO_2 (110) surface. *J. Mater. Chem. A, 1,* 14879-14887.

Miao, Wu, T., Li, J., Yi, T., Zhang, Y., and Yang, X. (2015). Aerobic oxidation of 5-hydroxymethylfurfural (HMF) effectively catalyzed by a $Ce_{0.8}Bi_{0.2}O_2-δ$ supported Pt catalyst at room temperature. *RSC Adv., 5,* 19823-19829.

Mishra, D.K., Lee, H.J., Kim, J., Lee, H.-S., Cho, J.K., Suh, Y.-W., Yi, Y., and Kim, Y.J. (2017). $MnCo_2O_4$ spinel supported ruthenium catalyst for air-oxidation of HMF to FDCA under aqueous phase and base-free conditions. *Green Chem., 19,* 1619-1623.

Monkhorst, H.J., and Pack, J.D. (1976). Special points for Brillouin-zone integrations. *Phys. Rev. B., 13,* 5188-5192.

Olsen, R.A., Kroes, G.J., Henkelman, G., Arnaldsson, A., and Jónsson, H. (2004). Comparison of methods for finding saddle points without knowledge of the final states. *J. Chem. Phys., 121,* 9776-9792.

Paik, Y., Osegovic, J.P., Wang, F., Bowden, W., and Grey, C.P. (2001). ^{2}H MAS NMR studies of the manganese dioxide tunnel structures and hydroxides used as cathode materials in primary batteries. *J. Am. Chem. Soc.,* 123, 9367-9377.

Pal, P., Kumar, S., Devi, M.M., and Saravanamurugan, S. (2020). Oxidation of 5-hydroxymethylfurfural to 5-formyl furan-2-carboxylic acid by non-precious transition metal oxide-based catalyst. *J Supercritical Fluids., 160,* 104812.

Pasini, T., Piccinini, M., Blosi, M., Bonelli, R., Albonetti, S., Dimitratos, N., Lopez-Sanchez, J.A., Sankar, M., He, Q., Kiely, C.J., Hutchings, G.J., and Cavani, F. (2011). Selective oxidation of 5-hydroxymethyl-2-furfural using supported gold–copper nanoparticles. *Green Chem., 13,* 2091-2099.

Perdew, J.P., Burke, K., and Ernzerhof, M. (1996). Generalized gradient approximation made simple. *Phys. Rev. Lett., 77,* 3865-3868.

Ren, J., Song, K.-h., Li, Z., Wang, Q., Li, J., Wang, Y., Li, D., and Kim, C.K. (2018). Activation of formyl C-H and hydroxyl O-H bonds in HMF by the CuO(111) and Co_3O_4 (110) surfaces: A DFT study. *Appl. Surf. Sci., 456,* 174-183.

Saha, B., Gupta, D., Abu-Omar, M.M., Modak, A., and Bhaumik, A. (2013). Porphyrin-based porous organic polymer-supported iron(III) catalyst for efficient aerobic oxidation of 5-hydroxymethyl-furfural into 2,5-furandicarboxylic acid. *J. Catal., 299,* 316-320.

Sajid, M., Zhao, X., and Liu, D. (2018). Production of 2,5-furandicarboxylic acid (FDCA) from 5-hydroxymethylfurfural (HMF): Recent progress focusing on the chemical-catalytic routes. *Green Chem., 20,* 5427-5453.

Sato, H., Wakiya, K., Enoki, T., Kiyama, T., Wakabayashi, Y., Nakao, H., and Murakami, Y. (2001). Magnetic structure of β-MnO_2 x-ray magnetic scattering study. *J. Phys. Soc. Jpn., 70,* 37-40.

Smidstrup, S., Pedersen, A., Stokbro, K., and Jonsson, H. (2014). Improved initial guess for minimum energy path calculations. *J. Chem. Phys., 140,* 214106.

Song, Z., Yan, Z., Yang, X., Bai, H., Duan, Y., Yang, B., and Leng, L. (2018). First principles density functional theory study of Pb doped α-MnO_2 catalytic materials. *Chem. Phys. Lett., 695,* 216-221.

Tong, X., Ma, Y., and Li, Y. (2010). Biomass into chemicals: Conversion of sugars to furan derivatives by catalytic processes. *Appl. Catal. A: Gen., 385,* 1-13.

Tong, X., Yu, L., Chen, H., Zhuang, X., Liao, S., and Cui, H. (2017). Highly efficient and selective oxidation of 5-hydroxymethylfurfural by molecular oxygen in the presence of Cu-MnO_2 catalyst. *Catal. Comm., 90,* 91-94.

van Putten, R.-J., van der Waal, J.C., de Jong, E., Rasrendra, C.B., Heeres, H.J., and de Vries, J.G. (2013). Hydroxymethylfurfural, a versatile platform chemical made from renewable resources. *Chem. Rev., 113,* 1499-1597.

Villa, A., Schiavoni, M., Campisi, S., Veith, G.M., and Prati, L. (2013). Pd-modified Au on carbon as an effective and durable catalyst for the direct oxidation of HMF to 2,5-furandicarboxylic acid. *ChemSusChem., 6,* 609-612.

Wang, Yu, K., Lei, D., Si, W., Feng, Y., Lou, L.-L., and Liu, S. (2016). Basicity-tuned hydrotalcite-supported Pd catalysts for aerobic oxidation of 5-hydroxymethyl-2-furfural under mild conditions. *ACS Catal., 4,* 4752-4761.

Wang, F., Lai, J., Liu, Z., Wen, S., and Liu, X. (2022). Copper-manganese oxide for highly selective oxidation of 5-hydroxymethylfurfural to bio-monomer 2, 5-furandicarboxylic acid. *Biomass Conv. Bioref., 13,* 1-12.

Wei, Y., Zhang, Y., Chen, Y., Wang, F., Cao, Y., Guan, W., and Li, X. (2022). Crystal Faces-Tailored Oxygen Vacancy in Au/CeO$_2$ Catalysts for Efficient Oxidation of HMF to FDCA. *ChemSusChem, 15,* e202101983.

Yamaguchi, Y., Aono, R., Hayashi, E., Kamata, K., and Hara, M. (2020). Template-free synthesis of mesoporous β-MnO$_2$ nanoparticles: Structure, formation mechanism, and catalytic properties. *ACS Appl. Mater. Interfaces, 12,* 36004-36013.

Yang, Y., Xu, D., Zhang, B., Xue, Z., and Mu, T. (2021). Substrate molecule adsorption energy: An activity descriptor for electrochemical oxidation of 5-hydroxymethylfurfural (HMF). *Chem. Eng. J., 433,* 133842.

Yao, Y.-F., and Wang, G.-C. (2021). Mechanism insights into the aerobic oxidation of 5-hydroxymethylfurfural to 2,5-furandicarboxylic acid over MnO$_2$ catalysts. *J. Phys. Chem. C., 125,* 3818-3826.

Yi, G., Teong, S.P., and Zhang, Y. (2016). Base-free conversion of 5-hydroxymethylfurfural to 2,5-furandicarboxylic acid over a Ru/C catalyst. *Green Chem., 18,* 979-983.

Yu, K., Liu, Y., Lei, D., Jiang, Y., Wang, Y., Feng, Y., Lou, L.-L., Liu, S., and Zhou, W. (2018). M^{3+}O(–Mn^{4+})$_2$ clusters in doped MnO$_x$ catalysts as promoted active

sites for the aerobic oxidation of 5-hydroxymethylfurfural. *Catal. Sci. Technol.*, *8,* 2299-2303.

Yu, L., Chen, H., Wen, Z., Jin, M., Ma, Z., Ma, X., Sang, Y., Chen, M., and Li, Y. (2021). Highly selective oxidation of 5-hydroxymethylfurfural to 2,5-diformylfuran over an α-MnO$_2$ catalyst. *Catal. Today.*, *367,* 9-15.

Yuan, H., Liu, H., Du, J., Liu, K., Wang, T., and Liu, L. (2020). Biocatalytic production of 2,5-furandicarboxylic acid: recent advances and future perspectives. *Appl. Microbiol. Biotechnol.*, *104,* 527-543.

Zhang, S., Sun, X., Zheng, Z., and Zhang, L. (2018). Nanoscale center-hollowed hexagon MnCo$_2$O$_4$ spinel catalyzed aerobic oxidation of 5-hydroxymethylfurfural to 2,5-furandicarboxylic acid. *Catal. Comm.*, *113,* 19-22.

Zhong, X., Yuan, P., Wei, Y., Liu, D., Losic, D., and Li, M. (2022). Coupling natural halloysite nanotubes and bimetallic Pt–Au alloy nanoparticles for highly efficient and selective oxidation of 5-hydroxymethylfurfural to 2,5-furandicarboxylic acid. *ACS Appl. Mater. Interfaces.*, *14,* 3949-3960.

Zhou, C., Deng, W., Wan, X., Zhang, Q., Yang, Y., and Wang, Y. (2015). Functionalized carbon nanotubes for biomass conversion: The base-free aerobic oxidation of 5-hydroxymethylfurfural to 2,5-furandicarboxylic acid over platinum supported on a carbon nanotube catalyst. *ChemCatChem.*, *7,* 2853-2863.

Zhu, J., Cheng, F., Wang, F., Wen, S., and Liu, X. (2022). Selective oxidation of 5-hydroxymethylfurfural to 2, 5-diformylfuran over a vanadium manganese oxide catalyst. *Catal. Lett.*, *152,* 2280-2287.

CHAPTER V

CONCLUSIONS

This thesis presents a complete mechanistic study of HMF to FDCA over the β–MnO$_2$(110) surface investigated by the density functional theory (DFT) method, microkinetic analysis, and compared with experiment studies. We explored the most stable structure of the HMF molecule adsorption and all possible reaction pathways for HMF oxidation on the β–MnO$_2$(110) surface. In addition, we have compared the mechanism and kinetic properties of HMF oxidation on non-hydroxylated and hydroxylated surfaces to understand the role of a hydroxyl group the HMF oxidation in MnO$_2$. For the experiment part, the reactions were conducted and compared in water and dimethyl sulfoxide (DMSO) to understand the influence of active species on the catalytic performance of this catalyst.

The calculated adsorption energy (E$_{ads}$) of HMF molecules on the catalyst surface reveals that the most stable is the bridge-on configurations (1D) with an adsorption energy of −1.44 eV. This indicates chemisorption and quite strong binding of HMF on β–MnO$_2$(110). In addition, we found that the HMF molecule prefers to point two oxygen atoms of hydroxyl and formyl group toward Mn$_{4c}$ active site to form chemisorption with the surface. The suitable adsorption structure of HFM on the surface promotes the reaction mechanism.

The reaction mechanism and kinetic studies reveal that the HMF oxidation on β–MnO$_2$(110) prefers the 2,5-diformylfuran (DFF) route over the 5-hydroxymethyl-2-furan carboxylic acid (HMFCA) before proceeding to 5-formyl-2-furan carboxylic acid (FFCA) and FDCA on both surfaces (non-hydroxylated and hydroxylated surfaces). This result indicates that DFF is more selective than HMFCA in this catalytic model. In addition, we found that the C−H bond breaking at the formyl group of DFF by the surface oxygen is the rate-determining step on a non-hydroxylated surface. While the C-H bond breaking of FFCA (Hemiacetal-like structure) is the rate-determining step on a hydroxylated surface. Therefore, we conclude that the DFF-to-FFCA and FFCA-to-

FDCA are the rate-determining steps on the bare and hydroxylated surface, respectively.

Experimental studies carried out by Dr. Kajornsak Faungnawakij reveal a high HMF conversion of ≥99 mol% under using water and DMSO as the solvent. The selectivity result reveals that the HMF oxidation reaction prefers the DFF route over the HMFCA route and DFF becomes the main product on the non-hydroxylated β–MnO_2(110) surface. In addition, comparing the FDCA yield of the HMF oxidation reaction in water and DMSO reveal that HMF oxidation in water has more FDCA yield than DMSO. The computational and experiment clearly suggest that OH promotes HMF oxidation, while surface oxygen also plays a role in the low OH coverage. Therefore, we can conclude that both active oxygen species (i.e. OH and surface oxygen) are crucial to promote the FFCA oxidation reaction.

This thesis not only reveals the molecular-scale phenomena of the surface reaction, but the outputs also guide the way to improve the activity and designs of reusable, low-cost, and effective metal oxide-based catalysts for the HMF to FDCA reaction.
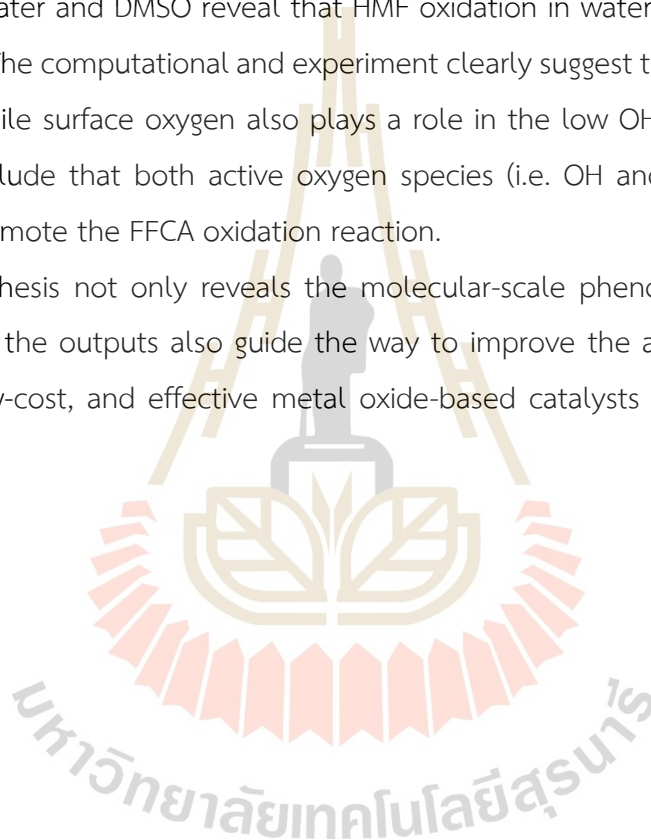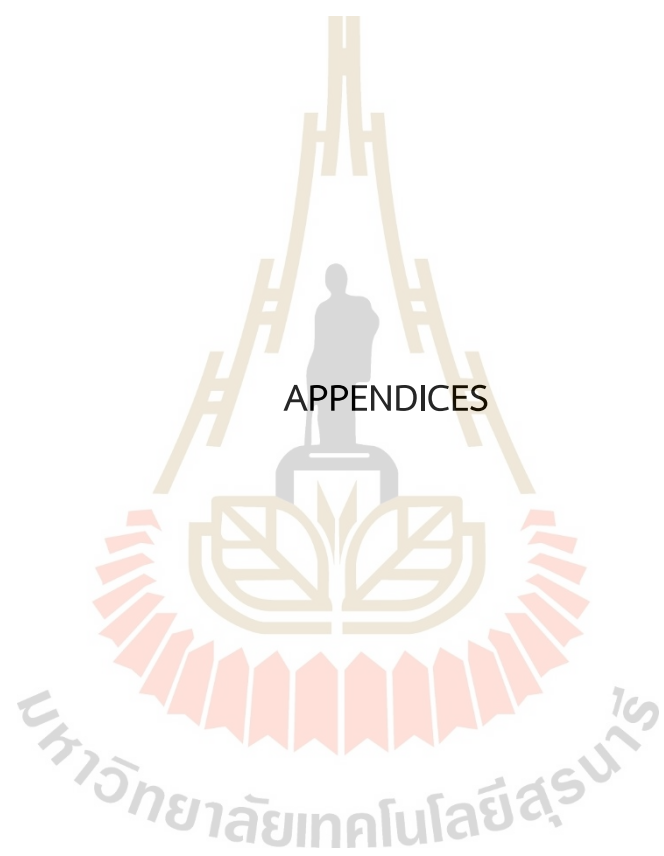
APPENDICES

APPENDIX A

ANTIFERROMAGNETIC MODELS FOR β-MnO$_2$(110) SURFACE

A.1   Optimization of different magnetization for β-MnO$_2$(110) surface

Table A1 Optimization of antiferromagnetic (AFM) models for β-MnO$_2$(110) surface.

AFM modes	Ground state energy (eV)	Relative energy (eV)
AFM-1	-1065.36	0.01
AFM-2	-1065.37	0.00
AFM-3	-1063.31	2.06
AFM-4	-1064.52	0.85
AFM-5	-1064.18	1.19
AFM-6	-1064.53	0.84
AFM-7	-1064.90	0.47
AFM-8	-1064.37	1.00
AFM-9	-1065.31	0.06

This thesis has considered the magnetic properties of β-MnO$_2$(110) surface. According to the literature β-MnO$_2$ has a screw-type magnetic structure with helically ordered moments (Paik, Osegovic et al., 2001, Franchini, Podloucky et al., 2007). MnO$_2$ was studied in its experimental antiferromagnetic (AFM) arrangement. Other magnetic orderings were found to be significantly less stable than AFM. In addition, the antiferromagnetic (AFM) properties have spin magnetic moments closer to the experiment values (Paik, Osegovic et al., 2001). Therefore, this thesis takes an antiferromagnetic state arrangement as the calculations' beginning. **Tabel A1 and Figure A1** shown the relative energy and structure optimization in different AFM models for β-MnO$_2$(110) surface. The results shown that AFM-2 were the most stable magnetic moments structure.
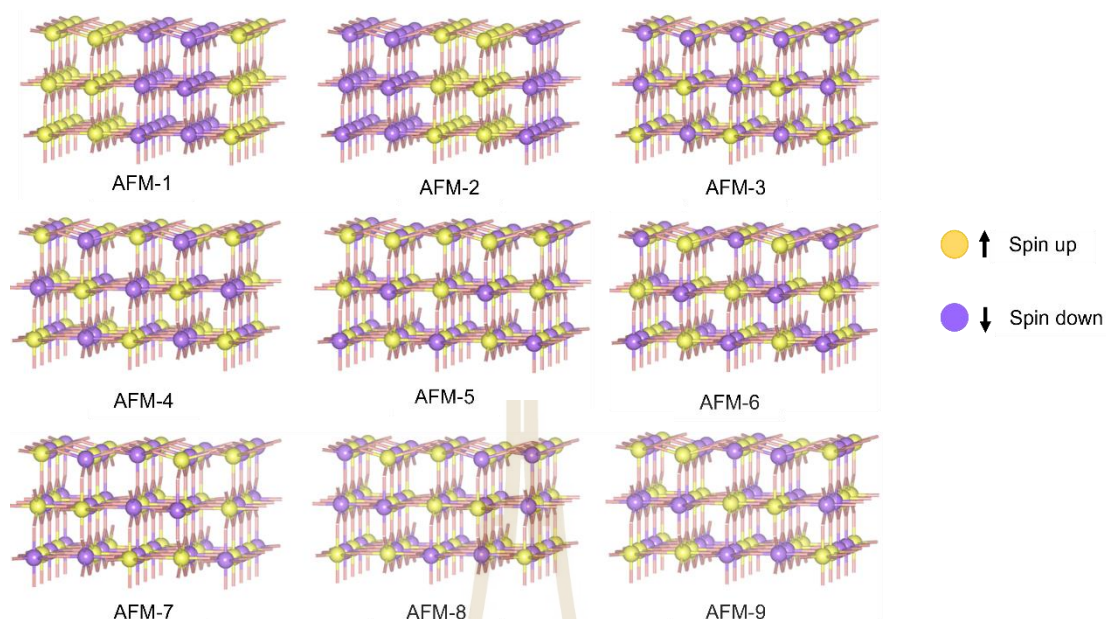
Figure A1 Structure optimization for antiferromagnetic (AFM) models of β-MnO$_2$(110) surface, the yellow and purple atoms presented with the position of spin up and spin down, respectively.

Reference

Franchini, C., Podloucky, R., Paier, J., Marsman, M., and Kresse, G. (2007). Ground-state properties of multivalent manganese oxides: Density functional and hybrid density functional calculations. *Phys. Rev. B, 75,* 195128.

Paik, Y., Osegovic, J.P., Wang, F., Bowden, W., and Grey, C.P. (2001). ^{2}H MAS NMR studies of the manganese dioxide tunnel structures and hydroxides used as cathode materials in primary batteries. *J. Am. Chem. Soc., 123,* 9367-9377.

APPENDIX B

MICROKINETIC CODE

Most of the reaction mechanisms are too complicated to solve analytically. Therefore, this thesis uses an ODE solver like Python to solve the kinetic equation to calculate reaction rates, apparent activation energies, and degree of rate control.

B.1   Microkinetic code for HMF oxidation on of β-MnO$_2$(110) surface

Calculations of thermodynamic parameters

Reaction: HMF-oxidation

```
In [1]: import numpy as np
        import pandas as pd
```

```
In [2]: ### Define physical constants and conversion factors
        J2eV    = 6.24150974E18       # eV/J
        Jmol2eV = 1.03642723013e-5 # eV/J.mol-1
        h_J     = 6.62607004e-34      # J/K
        h       = h_J * J2eV          # eV*s
        kB_J    = 1.380650E-23        # J/K
        kB      = kB_J * J2eV         # eV/K
        R       = 8.3144598           # J/mol/K
        NA      = 6.0221415E23        # mol-1
        c       = 29979245800         # cm/s (speed of light)
        P0      = 1e5                 # bar2Pa
```

Part 1: Thermodynamic parameters

Define reaction conditions

```
In [3]: ##### <edit value of T>
        T    = 298.15              # in K (approximate from 120 degree C = 393 K)
        ##### <edit value of T>
        kbT  = kB * T
        A    = 1.4285E-18          # in m^2
        m    = [126.032, 124.016, 142.027, 140.011, 156.006, 2.016, 31.990, 18.015]        # molecular mass in amu
```

Calculate thermodynamic parameters of gas species

```
In [4]:   ### Ther modynamic parameter of gases
          # Read gas data from excel
          filename = 'HMF-thermodata.xlsx'
          df_gas_energy = pd.read_excel(filename, sheet_name='gas')
          df_gas_vib   = pd.read_excel(filename, sheet_name='gas_vib')
          df_gas_trans = pd.read_excel(filename, sheet_name='gas_trans')
          df_gas_rot   = pd.read_excel(filename, sheet_name='gas_rot')

          gas_name = df_gas_energy['Name'].dropna().to_numpy()
          gas_num  = len(gas_name)

          # Calculate ZPE and qvib
          gas_ZPE  = np.zeros(gas_num)
          gas_lnqvib = np.zeros(gas_num)
          for i in range(gas_num):
              gas = gas_name[i]
              try:
                  freq = df_gas_vib[gas].dropna().to_numpy()
              except:
                  print('Data of gas %s not found.' %gas)
              freqc = freq * c
              tmp_ZPE = 0
              tmp_qvib = 1
              for fq in freqc:
                  if (fq > 0) and not(np.isnan(fq)):
                      tmp_ZPE += (0.5 * h * fq)
                      tmp_qvib *= (1/(1.0-np.exp(-h*fq/kbT)))
              gas_ZPE[i] = tmp_ZPE
              gas_lnqvib[i] = np.log(tmp_qvib)

          T_list = df_gas_trans['T(K)'].dropna().to_numpy()
          T_ind = np.where(T_list == T)[0][0]        # finding T_index in the T_list, T_ind = np.where(T_list == T)[0][0]
```

```
          # Read qtrans and qrot
          gas_lnqtrans = np.zeros(gas_num)
          gas_lnqrot   = np.zeros(gas_num)
          for i in range(gas_num):
              gas = gas_name[i]
              tmp_qtrans = df_gas_trans[gas]
              gas_lnqtrans[i] = tmp_qtrans[T_ind]
              tmp_qrot = df_gas_rot[gas]
              gas_lnqrot[i] = tmp_qrot[T_ind]

          # Calculate qtotal
          gas_lnq = gas_lnqvib + gas_lnqtrans + gas_lnqrot

          # Calculate zero-point corrected energy
          gas_E  = df_gas_energy['Energy'].dropna().to_numpy()
          gas_E0 = gas_E + gas_ZPE
          S_gas  = kB*gas_lnq
          gas_G  = gas_E0 - T*S_gas

          # Show data in table (short version)
          data = {'gas':gas_name, 'E0(eV)':gas_E,'ln(qvib)':gas_lnqvib, 'ln(qtrans)':gas_lnqtrans, 'ln(qrot)':gas_lnqrot,
                  'ZPE(eV)':gas_ZPE, 'ln(q)':gas_lnq, 'H(eV)':gas_E0, 'S(eV)':S_gas, 'G(eV)':gas_G}

          # Show data in table (short version)
          pd.options.display.float_format = '{:.4f}'.format # round to two decimal places in pandas
          df_gas = pd.DataFrame(data)
          df_gas
```

Calculate thermodynamic parameters of adsorbate species

```python
In [5]: ### Thermodynamic parameter of surface
        # Read surface data from excel
        filename = 'HMF-thermodata.xlsx'
        df_ads_energy = pd.read_excel(filename, sheet_name='adsorbate')
        df_ads_vib    = pd.read_excel(filename, sheet_name='adsorbate_vib')

        ads_name = df_ads_energy['Name'].dropna().to_numpy()
        ads_num  = len(ads_name)

        # Calculate ZPE and qvib
        ads_ZPE   = np.zeros(ads_num)
        ads_lnqvib = np.zeros(ads_num)
        for i in range(ads_num):
            ads = ads_name[i]
            try:
                freq = df_ads_vib[ads].dropna().to_numpy()
            except:
                print('Data of adsorbate %s not found.' %ads)
            freqc = freq * c
            tmp_ZPE = 0
            tmp_qvib = 1
            for fq in freqc:
                if (fq > 0) and not(np.isnan(fq)):
                    tmp_ZPE += (0.5 * h * fq)
                    tmp_qvib *= (1/(1.0-np.exp(-h*fq/kbT)))
            ads_ZPE[i] = tmp_ZPE
            ads_lnqvib[i] = np.log(tmp_qvib)

        # Calculate qtotal
        ads_lnq = ads_lnqvib

        ads_E  = df_ads_energy['Energy'].dropna().to_numpy()
        ads_E0 = ads_E + ads_ZPE
        S      = kB * ads_lnq
        G_ads  = ads_E0 - T*S

        ####################### E Relative ##########################################
        ads_Eint = np.zeros(ads_num)
        for i in range(ads_num):
            E_relative = ads_E[0] + gas_E[0] + 1.5*gas_E[6]
            ads_Eint[0] = (ads_E[0] + gas_E[0] + 1.5*gas_E[6]) - E_relative
            ads_Eint[i] = (ads_E[i] + 1.5*gas_E[6]) - E_relative

            ads_Eint[28] = (ads_E[28] + 1.5* gas_E[6] + gas_E[4]) - E_relative         #28 FDCA desorption
            ads_Eint[30] = (ads_E[30] + gas_E[4] + gas_E[7]) - E_relative              #30

        ####################### G Relative ##########################################
        ads_Gint = np.zeros(ads_num)
        for i in range(ads_num):
            G_relative = G_ads[0] + gas_G[0] + 1.5*gas_G[6]
            ads_Gint[0] = (G_ads[0] + gas_G[0] + 1.5*gas_G[6]) - G_relative
            ads_Gint[i] = (G_ads[i] + 1.5*gas_G[6]) - G_relative

            ads_Gint[28] = (G_ads[28] + 1.5* gas_G[6] + gas_G[4]) - G_relative         #28 FDCA desorption
            ads_Gint[30] = (G_ads[30] + gas_G[4] + gas_G[7]) - G_relative              #30

        # Show data in table (short version)
        data = {'adsorbate':ads_name,'E0 (eV)':ads_E, 'ZPE (eV)':ads_ZPE, 'ln(q)':ads_lnq, 'H (eV)':ads_E0, 'S (eV)':S, 'G (eV)':G_ads,
                'Relative_E(eV)':ads_Eint, 'Relative_G(eV)':ads_Gint}
        pd.options.display.float_format = '{:.3f}'.format # round to two decimal places in pandas
        df_ads = pd.DataFrame(data)
        df_ads
```

Part 2: Reactions

Calculate reaction and activation energies

```
In [6]:  # Functions to calculate reaction and activation energies
         def calc_Aads(name, E_IS, E_FS, G_IS, G_FS):
             dEr = E_FS - E_IS
             dEa = 0
             dGr = (G_FS - G_IS)
             dGa = 0
             return name, dEr, dEa, dGr, dGa

         def calc_dG_arr(name, E_IS, E_FS, E_TS, G_IS, G_FS, G_TS):
             dEr = E_FS - E_IS
             dEa = E_TS - E_IS
             dGr = (G_FS - G_IS)
             dGa = (G_TS - G_IS)
             return name, dEr, dEa, dGr, dGa

         def calc_dG_ar_noTS(name, E_IS, E_FS, G_IS, G_FS):
             dEr = (E_FS - E_IS)
             dEa = max(dEr, 0)
             dGr = (G_FS - G_IS)
             dGa = max(dGr, 0)
             return name, dEr, dEa, dGr, dGa

         def calc_dG_desorption(name, E_IS, E_FS, G_IS, G_FS):
             dEr = (E_FS - E_IS)
             dEa = 0
             dGr = (G_FS - G_IS)
             dGa = 0
             return name, dEr, dEa, dGr, dGa
```

```
In [7]:  # Calculate reaction and activation energies
         def get_dG_all_reactions(ads_E0v):
             # Initialize data
             reaction_name = np.zeros(num_reaction, dtype='U40')
             dEr = np.zeros(num_reaction)
             dEa = np.zeros(num_reaction)
             dGr = np.zeros(num_reaction)
             dGa = np.zeros(num_reaction)

             #reaction   j=0: HMF_Ads;
             j = 0
             reaction_name[j], dEr[j], dEa[j], dGr[j], dGa[j] \
                 = calc_Aads('HMF_Ads', ads_Eint[0], ads_Eint[1], ads_Gint[0], ads_Gint[1])

             #reaction   j=1: HMF_rearrangement;
             j = 1
             reaction_name[j], dEr[j], dEa[j], dGr[j], dGa[j] \
                 = calc_dG_ar_noTS('HMF_rearrangement', ads_Eint[1], ads_Eint[2], ads_Gint[1], ads_Gint[2])

             #reaction   j=2: Formyl_Oxidation_A;*
             j = 2
             reaction_name[j], dEr[j], dEa[j], dGr[j], dGa[j] \
                 = calc_dG_arr('Formyl_Oxidation_A', ads_Eint[2], ads_Eint[4], ads_Eint[3], ads_Gint[2], ads_Gint[4], ads_Gint[3])

             #reaction   j=3: OH_Formation_A_I;
             j = 3
             reaction_name[j], dEr[j], dEa[j], dGr[j], dGa[j] \
                 = calc_dG_arr('OH_Formation_A_I', ads_Eint[4], ads_Eint[6], ads_Eint[5], ads_Gint[4], ads_Gint[6], ads_Gint[5])

             #reaction   j=4: OH_Breaking_A;
             j = 4
             reaction_name[j], dEr[j], dEa[j], dGr[j], dGa[j] \
                 = calc_dG_arr('OH_Breaking_A', ads_Eint[6], ads_Eint[8], ads_Eint[7], ads_Gint[6], ads_Gint[8], ads_Gint[7])

             #reaction   j=5: CH(alphaC)_Breaking_A;
             j = 5
             reaction_name[j], dEr[j], dEa[j], dGr[j], dGa[j] \
                 = calc_dG_arr('CH(alphaC)_Breaking_A', ads_Eint[8], ads_Eint[10], ads_Eint[9], ads_Gint[8], ads_Gint[10], ads_Gint[9])

             #reaction   j=6: OH_Formation_A_II;
             j = 6
             reaction_name[j], dEr[j], dEa[j], dGr[j], dGa[j] \
                 = calc_dG_arr('OH_Formation_A_II', ads_Eint[10], ads_Eint[19], ads_Eint[11], ads_Gint[10], ads_Gint[19], ads_Gint[11])

             #reaction   j=7: OH_Breaking_B;
             j = 7
             reaction_name[j], dEr[j], dEa[j], dGr[j], dGa[j] \
                 = calc_dG_arr('OH_Breaking_B', ads_Eint[1], ads_Eint[13], ads_Eint[12], ads_Gint[1], ads_Gint[13], ads_Gint[12])

             #reaction   j=8: CH(alphaC)_Breaking_B;
             j = 8
             reaction_name[j], dEr[j], dEa[j], dGr[j], dGa[j] \
                 = calc_dG_arr('CH(alphaC)_Breaking_B', ads_Eint[13], ads_Eint[15], ads_Eint[14], ads_Gint[13], ads_Gint[15],
                               ads_Gint[14])
```

```python
    #reaction  j=9: Formyl_Oxidation_B;
    j = 9
    reaction_name[j], dEr[j], dEa[j], dGr[j], dGa[j] \
        = calc_dG_arr('Formyl_Oxidation_B', ads_Eint[15], ads_Eint[17], ads_Eint[16], ads_Gint[15], ads_Gint[17], ads_Gint[16])

    #reaction j=10: OH_Formation_B;
    j = 10
    reaction_name[j], dEr[j], dEa[j], dGr[j], dGa[j] \
        = calc_dG_arr('OH_Formation_B', ads_Eint[17], ads_Eint[19], ads_Eint[18], ads_Gint[17], ads_Gint[19], ads_Gint[18])

    #reaction j=11: FFCA_HMF_rearrangement;
    j = 11
    reaction_name[j], dEr[j], dEa[j], dGr[j], dGa[j] \
        = calc_dG_ar_noTS('FFCA_HMF_rearrangement', ads_Eint[19], ads_Eint[20], ads_Gint[19], ads_Gint[20])

    #reaction j=12: OH_Formation_C(Diol);
    j = 12
    reaction_name[j], dEr[j], dEa[j], dGr[j], dGa[j] \
        = calc_dG_arr('OH_Formation_C(Diol)', ads_Eint[20], ads_Eint[22], ads_Eint[21], ads_Gint[20], ads_Gint[22],
                      ads_Gint[21])

    #reaction j=13: CH(alphaC)_Breaking_C;
    j = 13
    reaction_name[j], dEr[j], dEa[j], dGr[j], dGa[j] \
        = calc_dG_arr('CH(alphaC)_Breaking_C', ads_Eint[22], ads_Eint[24], ads_Eint[23], ads_Gint[22], ads_Gint[24],
                      ads_Gint[23])

    #reaction j=14: FDCA_Des;
    j = 14
    reaction_name[j], dEr[j], dEa[j], dGr[j], dGa[j] \
        = calc_dG_desorption('FDCA_Des', ads_Eint[24], ads_Eint[28], ads_Gint[24], ads_Gint[28])

    #reaction j=15: H2O_Formation;
    j = 15
    reaction_name[j], dEr[j], dEa[j], dGr[j], dGa[j] \
        = calc_dG_ar_noTS('FS_rearrangement', ads_Eint[28], ads_Eint[30], ads_Gint[28], ads_Gint[30])

    # Show data in table (short version)
    data = {'reaction':reaction_name,'dEr (eV)':dEr, 'dEa (eV)':dEa, 'dGr (eV)':dGr, 'dGa (eV)':dGa}
    pd.options.display.float_format = '{:.3f}'.format # round to two decimal places in pandas
    df_reac = pd.DataFrame(data)
    df_reac

    return reaction_name, dEr, dEa, dGr, dGa
```

Functions to calculate rate constants

```python
In [8]:  # Functions to calculate reaction rates
         def calc_k_arr(Gr, Ga):
             K   = np.exp(-Gr / kbT)
             kf  = kbT / h * np.exp(-Ga / kbT)
             kr  = kf / K
             return kf, kr, K

         def calc_k_ads(m, Gr):
             K   = np.exp(-Gr / kbT)
             kf  = A / np.sqrt(2 * np.pi * (m/NA/1000) * kB_J * T) * P0
             kr  = kf / K
             return kf, kr, K

         def calc_k_des(m, Gr):
             K   = np.exp(-Gr / kbT)
             kr  = A / np.sqrt(2 * np.pi * (m/NA/1000) * kB_J * T) * P0
             kf  = kr * K
             return kf, kr, K

         def n_calc_k_ads(m, sigma, theta_rot, Gr):
             R = 8.3144598      # gas constant
             if Gr < 0:  # adsorption
                 kf  = A / np.sqrt(2 * np.pi * m * kB_J * T)
                 kr  = kB_J * T**3 / h_J**3 * A * (2 * np.pi * m * kB_J) / (sigma * theta_rot) * np.exp( Gr / (kbT))
             else:       # desorption
                 kr  = A / np.sqrt(2 * np.pi * m * kB_J * T)
                 kf  = kB_J * T**3 / h_J**3 * A * (2 * np.pi * m * kB_J) / (sigma * theta_rot) * np.exp(-Gr / (kbT))
             return kf, kr, K
```

Functions to calculate rate constants and rate

```
In [9]:  # Calculate reaction rates
         def get_rate_constants(dGr, dGa):
             #Initialize data
             kf = np.zeros(num_reaction)
             kr = np.zeros(num_reaction)
             K  = np.zeros(num_reaction)

             j=0; kf[j], kr[j], K[j] = calc_k_ads(m[0], dGr[j])
             j=1; kf[j], kr[j], K[j] = calc_k_arr(dGr[j], dGa[j])
             j=2; kf[j], kr[j], K[j] = calc_k_arr(dGr[j], dGa[j])
             j=3; kf[j], kr[j], K[j] = calc_k_arr(dGr[j], dGa[j])
             j=4; kf[j], kr[j], K[j] = calc_k_arr(dGr[j], dGa[j])
             j=5; kf[j], kr[j], K[j] = calc_k_arr(dGr[j], dGa[j])
             j=6; kf[j], kr[j], K[j] = calc_k_arr(dGr[j], dGa[j])
             j=7; kf[j], kr[j], K[j] = calc_k_arr(dGr[j], dGa[j])
             j=8; kf[j], kr[j], K[j] = calc_k_arr(dGr[j], dGa[j])
             j=9; kf[j], kr[j], K[j] = calc_k_arr(dGr[j], dGa[j])
             j=10; kf[j], kr[j], K[j] = calc_k_arr(dGr[j], dGa[j])
             j=11; kf[j], kr[j], K[j] = calc_k_arr(dGr[j], dGa[j])
             j=12; kf[j], kr[j], K[j] = calc_k_arr(dGr[j], dGa[j])
             j=13; kf[j], kr[j], K[j] = calc_k_arr(dGr[j], dGa[j])
             j=14; kf[j], kr[j], K[j] = calc_k_des(m[4], dGr[j])
             j=15; kf[j], kr[j], K[j] = calc_k_arr(dGr[j], dGa[j])

             return kf, kr, K
```

Part3: Functions to do microkinetic model

```
In [10]:  from scipy.integrate import odeint
          from mpmath import mp, findroot
          import matplotlib.pyplot as plt
          %matplotlib inline
```

Define reaction rate constants, rate equations, and ODEs

```
In [11]:  ### Define rate equations ###
          def get_rates(theta):
              ### name the coverage specie
              t_HMF_I   = theta[0]
              t_HMF_II  = theta[1]
              t_A_COO   = theta[2]
              t_HMFCA   = theta[3]
              t_A_RCH2O = theta[4]
              t_A_RCHO  = theta[5]
              t_FFCA_I  = theta[6]
              t_B_RCH2O = theta[7]
              t_DFF     = theta[8]
              t_B_RCOO  = theta[9]
              t_FFCA_II = theta[10]
              t_C_RCHOH = theta[11]
              t_FDCA    = theta[12]
              t_HH      = theta[13]
              t_star    = 1.0 - np.sum(theta)

              ### define rate equations ###
              ratef = []
              rater = []
              rate  = []
              ratef.append(kf[0] * P_HMF * t_star)
              rater.append(kr[0] * t_HMF_I)
              ratef.append(kf[1] * t_HMF_I)
              rater.append(kr[1] * t_HMF_II)
              ratef.append(kf[2] * t_HMF_II)
              rater.append(kr[2] * t_A_COO)
              ratef.append(kf[3] * t_A_COO)
              rater.append(kr[3] * t_HMFCA)
              ratef.append(kf[4] * t_HMFCA)
              rater.append(kr[4] * t_A_RCH2O)
              ratef.append(kf[5] * t_A_RCH2O)
              rater.append(kr[5] * t_A_RCHO)
              ratef.append(kf[6] * t_A_RCHO)
              rater.append(kr[6] * t_FFCA_I)
              ratef.append(kf[7] * t_HMF_I)
              rater.append(kr[7] * t_B_RCH2O)
              ratef.append(kf[8] * t_B_RCH2O)
              rater.append(kr[8] * t_DFF)
              ratef.append(kf[9] * t_DFF)
              rater.append(kr[9] * t_B_RCOO)
              ratef.append(kf[10] * t_B_RCOO)
              rater.append(kr[10] * t_FFCA_I)
              ratef.append(kf[11] * t_FFCA_I)
              rater.append(kr[11] * t_FFCA_II)
              ratef.append(kf[12] * t_FFCA_II)
              rater.append(kr[12] * t_C_RCHOH)
              ratef.append(kf[13] * t_C_RCHOH)
              rater.append(kr[13] * t_FDCA)
```

```
            ratef.append(kf[14] * t_FDCA)
            rater.append(kr[14] * P_FDCA * t_HH)
            ratef.append(kf[15] * t_HH)
            rater.append(kr[15] * t_star)

        for i in range(num_reaction):
            rate.append(ratef[i]-rater[i])
        return ratef, rater, rate

### Define ODEs ###
def get_derivatives(theta, t):
    _,_,rate = get_rates(theta)
    ### define ODE equations ###
    dt_HMF_I    = (+ rate[0] - rate[1] - rate[7])
    dt_HMF_II   = (+ rate[1] - rate[2])
    dt_A_COO    = (+ rate[2] - rate[3])
    dt_HMFCA    = (+ rate[3] - rate[4])
    dt_A_RCH2O  = (+ rate[4] - rate[5])
    dt_A_RCHO   = (+ rate[5] - rate[6])
    dt_FFCA_I   = (+ rate[6] + rate[10] - rate[11])
    dt_B_RCH2O  = (+ rate[7] - rate[8])
    dt_DFF      = (+ rate[8] - rate[9])
    dt_B_RCOO   = (+ rate[9] - rate[10])
    dt_FFCA_II  = (+ rate[11] - rate[12])
    dt_C_RCHOH  = (+ rate[12] - rate[13])
    dt_FDCA     = (+ rate[13] - rate[14])
    dt_HH       = (+ rate[14] - rate[15])


    return [dt_HMF_I, dt_HMF_II, dt_A_COO, dt_HMFCA, dt_A_RCH2O, dt_A_RCHO, dt_FFCA_I, dt_B_RCH2O, dt_DFF,
            dt_B_RCOO, dt_FFCA_II, dt_C_RCHOH, dt_FDCA, dt_HH]
```

Solve MKM by Newton-method (Steady state solution)

```
In [12]: def solve_findroot(ttheta):
             # Use mpmath's findroot to solve the model
             ##################### <Adjust> ##################################
             tol = 1.0e-50
             ##################### <Adjust> ##################################
             mp.dps = 50
             mp.pretty = True
             def tmp(*args):
                 return get_derivatives(args,0)
             theta = findroot(tmp,
                              tuple(ttheta),
                              solver='mdnewton',
                              tol=tol,
                              multidimensional=True)
             return np.array(theta)
```

Print output

```
In [13]: def print_solutions(theta_findroot, rate_only = False):
             if rate_only == False:
                 print('\n')
                 print('Steady state solutions')
                 print('\n')
                 print('>>> Coverages on catalyst surface (in ML, monolayer):')
                 for i in range(num_coverage):
                     print('   # %2d = %6.4e' %(i, theta_findroot[i]))
                 theta_star = 1.0-np.sum(theta_findroot)
                 print('   #  * = %6.4e' %(theta_star))
                 if theta_star < 0:
                     print('WARNING! The theta_star is negative!')
                 print('\n')
                 print('>>> Rates of elementary steps (in s^-1):')
                 ratef_findroot, rater_findroot, rate_findroot = get_rates(theta_findroot)
                 print('           forward      backward       net')
                 for i in range(num_reaction):
                     print('   # %2d || %6.4e || %6.4e || %6.4e' %(i, ratef_findroot[i], rater_findroot[i], rate_findroot[i]))
                 print('     =====================================')
                 print('     overall rate = %6.4e' %(rate_findroot[-1]))
                 print('\n')
                 print('>>> Derivatives')
                 dthetadt_findroot = get_derivatives(theta_findroot, 0)
                 print('   maximum d(theta)/dt: %6.2e' %(np.max(dthetadt_findroot)))
                 print('   It should approach zero!')
                 print('\n')
             else:
                 ratef_findroot, rater_findroot, rate_findroot = get_rates(theta_findroot)
                 print('>>> overall rate = %6.4e s^-1' %(rate_findroot[-1]))
```

Set parameters

```
In [14]: num_reaction = 16
         num_coverage = 14
         # Define pressure
         P0 = 1e5              # in Pa
         P_HMF  = 0.04         # in bar
         P_FDCA = 1e-20        # in bar
         P_O2   = 8.16e-5      # in bar # mol of O2 gas in water  8.16e-5
         P_H2O  = 1e-20        # in bar
```

Calculations of rates and coverages

```
In [15]:  ## MAIN FUNCTION ##
          cov_name = ['*','HMF_I*','HMF_II*','A_COO*','HMFCA*','A_RCH2O*','A_RCHO*','FFCA_I*','B_RCH2O*', 'DFF*', 'B_RCOO*',
                      'FFCA_II*','C_RCHOH*','FDCA*', 'HH*']
          theta0 = np.zeros(num_coverage)

          reaction_name, dEr, dEa, dGr, dGa = get_dG_all_reactions(ads_E0)
          kf, kr, K = get_rate_constants(dGr, dGa)

          theta_findroot = solve_findroot(theta0)
          print_solutions(theta_findroot, rate_only = False)
```

Calculations of degree of rate control for all transition states

```
In [18]:  cov_name = ['*','HMF_I*','HMF_II*','A_COO*','HMFCA*','A_RCH2O*','A_RCHO*','FFCA_I*','B_RCH2O*', 'DFF*', 'B_RCOO*',
                      'FFCA_II*','C_RCHOH*','FDCA*', 'HH*']

          theta0 = np.zeros(num_coverage)

          dE_range = np.arange(-0.0004, 0.0005, 0.0001)

          step_vary = [8, 9, 10]

          for ind in range(len(step_vary)):
              s_vary = step_vary[ind]
              kf_print = []
              kr_print = []
              rate_print = []
              for dE in dE_range:
                  kf_I = np.copy(kf)
                  kr_I = np.copy(kr)
                  kf[s_vary] = (1 + dE) * kf_I[s_vary]
                  kr[s_vary] = (1 + dE) * kr_I[s_vary]

                  kf_print.append(kf[s_vary])
                  kr_print.append(kr[s_vary])

                  theta_findroot = solve_findroot(theta0)
                  _, _, rate_findroot = get_rates(theta_findroot)

                  rate_print.append(rate_findroot[-1])

              print('############################################################################')
              for j in range(len(rate_print)):
                  print('dE = %6.3f | kf = %6.3f |rate = %10.8e s^-1' %(dE_range[j], kf_print[j], rate_print[j]))

              ln_rate = []
              ln_kf  = []
              for j in range(len(rate_print)):
                  ln_rate.append(np.log(float(rate_print[j])))
                  ln_kf.append(np.log(float(kf_print[j])))

              x = np.array(ln_kf)
              y = np.array(ln_rate)
              plt.scatter(x, y)
              slope, intercept = np.polyfit(x, y, 1)
              x_line = np.linspace(min(x), max(x))
              y_line = x_line * slope + intercept
              plt.plot(x_line, y_line, '--')
              plt.show()
              print('Xrc = %10.4f' %slope)
```

Calculations of degree of thermodynamic rate control for all intermediates

In [19]:
```python
cov_name = ['*','HMF_I*','HMF_II*','A_COO*','HMFCA*','A_RCH2O*','A_RCHO*','FFCA_I*','B_RCH2O*', 'DFF*', 'B_RCOO*',
            'FFCA_II*','C_RCHOH*','FDCA*', 'HH*']

theta0 = np.zeros(num_coverage)

dE_range = np.arange(-0.00004, 0.00005, 0.00001)
int_list = [1, 15, 17]

for ind in range(len(int_list)):
    int_vary = int_list[ind]
    E_print = []
    G_print = []
    rate_print = []

    for dE in dE_range:
        ads_E0v = np.copy(ads_E)
        ads_E0v[int_vary] = ads_E0v[int_vary] + dE

        G_ads = (ads_E0v[int_vary] + ads_ZPE[int_vary]) - T*S[int_vary]

        ads_Gint[int_vary] = (G_ads + 1.5*gas_G[6]) - G_relative

        E_print.append(ads_E0v[int_vary])
        G_print.append(G_ads)

        reaction_name, dEr, dEa, dGr, dGa = get_dG_all_reactions(ads_E0v)
        kf, kr, K = get_rate_constants(dGr, dGa)

        theta_findroot = solve_findroot(theta0)
        _, _, rate_findroot = get_rates(theta_findroot)

        rate_print.append(rate_findroot[-1])

    for j in range(len(rate_print)):
        print('dE = %6.3f | E = %6.3f | G = %6.3f |rate = %10.8e s^-1' %(dE_range[j], E_print[j], G_print[j], rate_print[j]))

    ln_rate = []
    GkT  = []
    for j in range(len(rate_print)):
        ln_rate.append(np.log(float(rate_print[j])))
        GkT.append(float(-G_print[j])/(kbT))

    x = np.array(GkT)
    y = np.array(ln_rate)
    plt.scatter(x, y)
    slope, intercept = np.polyfit(x, y, 1)
    x_line = np.linspace(min(x), max(x))
    y_line = x_line * slope + intercept
    plt.plot(x_line, y_line, '--')
    plt.show()
    print('Xrc = %10.5f' %slope)
```

APPENDIX C

PUBLICATION AND PRESENTATIONS

C.1   List of publications

Plucksacholatarn, A., <u>Tharat, B</u>., Suthirakun, S., Faungnawakij, K., and Junkaew, A. (2021). Theoretical insight into the interaction on Ni and Cu surfaces for HMF hydrogenation: a density functional theory study. *New Journal of Chemistry. 45*: 21543-21552.

Usmani, A., <u>Tharat, B</u>., Watwiangkham, A., Grisdanurak., N., and Suthirakun, S. (2023). Enhancing Kinetics of Carbonyl Sulfide Hydrolysis Using Pt-Supported Al_2O_3 Catalysts: First-Principles-Informed Energetic Span Analysis. *J. Phys. Chem. C. 127*: 9002–9012.

Ngamchuea, K., <u>Tharat, B</u>., Hirunsit, P., and Suthirakun, S. (2020). Electrochemical oxidation of resorcinol: mechanistic insights from experimental and computational studies. *RSC Adv. 10*: 28454-28463.

Plerdsranoy, P., <u>Tharat, B</u>., Thiangviriya, S., Kidkhunthod, P., Siritanon, T., Suthirakun, S., Utke, S. (2023). Hydrogen sorption kinetics and mechanism of $Mg_2Fe_{(1-x)}Ni_xH_6$. *Journal of Alloys and Compounds. 15*: 168212.

C.2   List of presentations

Tharat, B., Ngamwongwan, L., Faungnawakij, K., Suthirakun, S., and Junkaew, A. (2022). Mechanistic Study of Beta-Manganese Dioxide Catalysts for 5‑Hydroxymethylfurfural Conversion to 2,5-Furandicarboxylic Acid. **Pure and Applied Chemistry International Conference (PACCON 2022).** June 30th - July 1st of 2022, KMITL Convention Hall, King Mongkut's Institute of Technology Ladkrabang, Bangkok, Thailand. (Oral presentation)

Tharat, B., Ngamwongwan, L., Faungnawakij, K., Suthirakun, S., and Junkaew, A. (2022). Mechanistic Study of 5‑Hydroxymethylfurfural Conversion to 2,5-Furandicarboxylic Acid on Beta-Manganese dioxide catalysts: First Principles and Microkinetic Modeling. **The 25th International Annual Symposium on Computational Science and Engineering 2022 (ANSCSE25).** 8-11 June 2022, Department of Physics, Faculty of Science, Khon Kaen University, Thailand. (Poster presentation)

Tharat, B., Suthirakun, S., and Chiu, C, C. (2023). Computational exploration of dual atom catalysts on defective graphene for hydrogen storage at liquid organic hydride. **International Workshop on Green Chemistry**. 3 July 2023, Department of Chemistry, National Sun Yat-sen University, Kaohsiung, Taiwan. (Oral presentation)

Abstract submitted to The Pure and Applied Chemistry International Conference

(PACCON 2022)

MECHANISTIC STUDY OF BETA-MANGANESE DIOXIDE CATALYSTS FOR 5-HYDROXYMETHYLFURFURAL CONVERSION TO 2,5-FURANDICARBOXYLIC ACID

Bunrat Tharat[1], Lappawat Ngamwongwan[1], Kajornsak Faungnawakij[2], Anchalee Junkaew[2]*, and Suwit Suthirakun [1]*

[1] School of Chemistry, Institute of Science, Suranaree University of Technology
111 University Ave., Suranaree, Muang Nakhon Ratchasima 30000, Thailand

[2] National Nanotechnology Center, National Science and Technology Development Agency
111 Thailand Science Park, Phahonyothin Road, Khlong Nueng, Khlong Luang, Pathum Thani 12120, Thailand

*[1]Email: suthirak@sut.ac.th
*[2]Email: anchalee@nanotec.or.th

Recently, aerobic oxidation of 5-hydroxymethylfurfural (HMF) to 2,5-furandicarboxylic acid (FDCA) has been extensively studied because FDCA is a monomer for producing polyethylene furanoate (PEF), the well-known bio-based polymers. The development of efficient catalysts with inexpensive prices is still challenging. Manganese dioxide ($\beta-MnO_2$) has been proposed as a promising candidate for this reaction. However, a deep understanding of the nature of the active and full reaction mechanism over this catalyst's surface is still lacking. This work presents a complete mechanistic study of HMF to FDCA over the $\beta-MnO_2(110)$ surface investigated by density functional theory (DFT) method and microkinetic analysis. The calculation reveals that the HMF oxidation over $\beta-MnO_2$ prefers the 2,5-diformylfuran (DFF) route than the 5-hydroxymethyl-2-furan carboxylic acid (HMFCA) before proceeding to 5-formyl-2-furan carboxylic acid (FFCA) and FDCA (as shown in Scheme 1) The free energy profiles revealed that the C−H bond activation at the formyl group and the oxygen vacancy formation are crucial steps. Microkinetic analysis suggests that the dehydrogenation at a formyl group of DFF is the rate-determining step on a bare surface, whereas the dehydrogenation at a formyl group of FFCA is the rate-determining step on the hydroxylated surface. The reaction rate points out that the hydroxy group (OH) promotes a dehydrogenation mechanism for aerobic oxidation of HMF. This work not only reveals the molecular-scale phenomena of the surface reaction, but the outputs also guide the way to improve the activity of metal oxide-based catalysts for the HMF to FDCA reaction.

Keywords: 5-hydroxymethylfurfural; 2,5-furandicarboxylic acid; Mechanistic study; Manganese dioxide; DFT calculations; Microkinetic modeling
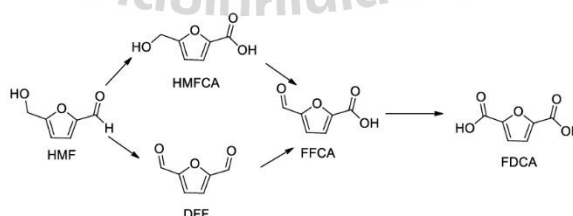
Scheme 1. Reaction pathway of HMF oxidation to produce FDCA.

Abstract submitted to The 25th International Annual Symposium on Computational Science and Engineering 2022 (ANSCSE25)

MECHANISTIC STUDY OF 5-HYDROXYMETHYLFURFURAL CONVERSION TO 2,5-FURANDICARBOXYLIC ACID ON BETA-MANGANESE DIOXIDE CATALYSTS: FIRST PRINCIPLES AND MICROKINETIC MODELING

B. Tharat[1], L. Ngamwongwan[1], K. Faungnawakij[2], A. Junkaew[2*], and S. Suthirakun[1*]

[1] *School of Chemistry, Institute of Science, Suranaree University of Technology*
111 University Ave., Suranaree, Muang Nakhon Ratchasima 30000, Thailand

[2] *National Nanotechnology Center, National Science and Technology Development Agency*
111 Thailand Science Park, Phahonyothin Road, Khlong Nueng, Khlong Luang, Pathum Thani 12120, Thailand

*Corresponding address (E-mail: suthirak@sut.ac.th, anchalee@nanotec.or.th)

The aerobic oxidation of aldehydes and alcohols over metal oxide-based catalysts is a critical reaction for biomass conversion into value-added chemicals. However, understanding the reaction mechanism is still challenging because it has a complicated reaction system and multiple reaction pathways. This work presents a mechanistic study of 5-hydroxymethylfurfural (HMF) to 2,5-furandicarboxylic acid (FDCA) over the $\beta-MnO_2(110)$ surface using the combined density functional theory (DFT) method and microkinetic analysis. Computations reveal that HMF oxidation prefers the 2,5-diformylfuran (DFF) pathway more than 5-hydroxymethyl-2-furan carboxylic acid (HMFCA) pathway before proceeding to 5-formyl-2-furan carboxylic acid (FFCA) and FDCA. The free energy profiles show that the dehydrogenation of the aldehyde group is a difficult step. Microkinetic analysis suggests that the dehydrogenation at a formyl group of DFF is the rate-determining step on a bare surface, whereas the dehydrogenation at group a formyl of FFCA is the rate-determining step on the hydroxylated surface. The reaction rate indicates that hydroxyl groups and active surface oxygen play a vital role in the HMF oxidation. A deeper understanding at molecular level can lead to further development and designs of reusable, low-cost, and effective metal oxide-based catalysts for HMF conversion.

Keywords: 5-hydroxymethylfurfural; 2,5-furandicarboxylic acid; manganese dioxide; DFT calculations; microkinetic modeling

Abstract submitted to International Workshop on Green Chemistry

International Workshop on Green Chemistry

Computational exploration of dual atom catalysts on defective graphene for hydrogen storage at liquid organic hydride

Bunrat Tharat[1], Suwit Suthirakun[1], Cheng-chau Chiu[2*]

[1] *School of Chemistry, Institute of Science, Suranaree University of Technology, Nakhon Ratchasima Thailand*

[2] *Department of Chemistry, National Sun Yat-sen University, Kaohsiung, Taiwan*

E-mail*: ccchiu@mail.nsysu.edu.tw

Mr. Bunrat Tharat
Education:
- Ph.D. candidate in Chemistry at Suranaree University of Technology (SUT), Thailand (2018–Present)
- B.Sc. (Chemistry), Ubon Ratchathani University, Thailand (2014–2017)

Scholarships: Thailand Graduate Institute of Science and Technology (TGIST- NSTDA)

Hydrogen is a clean and efficient energy carrier in various fuel-cell applications including vehicles, stationary and portable electronics, etc.[1] However, the lack of a suitable method for storage and transportation is still a limitation for its applications.[2] Liquid organic hydrogen carriers (LOHC) systems, in which hydrogen is bonded via covalent bonds are a potentially safe and cheap concept for H_2 storage. Hydrogen is stored and released through catalytic hydrogenation and dehydrogenation of organic molecules. The development of efficient and inexpensive catalysts for these reactions is still challenging. Currently, single and double-atom catalysts were widely studied as catalyst for various reactions.[3,4] In this work, we will present a mechanistic study of the hydrogenation of benzene to cyclohexane over palladium dimers supported on nitrogen doping graphene surfaces (Pd_2-N_X-VG) investigated by density functional theory (DFT) method. The energy profiles revealed that benzene hydrogenation to cyclohexane is kinetically and energetically favorable through 12B*, 123B*, and 1234B* intermediates (The numbers represent the positions of the hydrogenated C). In addition, we found that the second hydrogenation step, i.e. the conversion of 12B* to 123B*, has a barrier of about 0.90 eV, making it the rate-limiting process in the present system. However, this barrier is slightly lower than the value of the rate-limiting step on Pt (111), 1.04 eV.[5] This work not only reveals the molecular-scale phenomena of the surface reaction, but the outputs also guide the way to improve the activity of double-atom catalysts for benzene hydrogenation reaction.

References:
1. P. Megía, A. Vizcaíno, J. Calles et al., Energy Fuels **2021**, *35*, 16403−16415
2. J. Guo, C. Yin, D. Zhong et al., ChemSusChem **2021**, *14*, 2655 –2681
3. Y. Liu, R. Duan, X. Li et al., Inorg. Chem. **2022**, *61*, 13210−13217
4. T. He, A. Puente, D. Aijun., J. Catal. **2020**, *388*, 77-83
5. M. Saeys, M. Reyniers, M. Neurock et al., J. Phys. Chem. B **2005**, 1*06*, 2064–2073

CURRICULUM VITAE

Bunrat Tharat was born on May 9th, 1995, in Ubon Ratchathani, Thailand. He received his B.Sc. in Chemistry (Second-class honors) in 2017 from the Department of Chemistry, Faculty of Science, Ubon Ratchathani University, Thailand. He received a scholarship from Young Scientist and Technologist Program (YSTP - NSTDA) during 2016 - 2017. During his senior year in bachelor's degree, he studied research in the molecular modeling design and synthesis of InhA inhibitors in the class of 1-(Benzimidazol-1-yl)-3-(2,3-Dihydro-1H-inden-5-yloxy) Propan-2-ol derivatives as an anti-TB agent under the supervision of Assoc. Prof. Dr. Pornpan Pungpo. In 2018, he continued to pursue the doctor's degree program at the School of Chemistry, Suranaree University of Technology, Thailand under the supervision of Assoc. Prof. Dr. Suwit Suthirakun and Dr. Anchalee Junkaew from the National Nanotechnology Center (NANOTEC), Thailand Science Park. He received the Graduate Potential Scholarship from Suranaree University of Technology during 2018 - 2019. Then, he received the Thailand Graduate Institute of Science and Technology (TGIST) by the National Science and Technology Development Agency (NSTDA) during 2020 – 2023. In 2023, He was a graduate research assistant at the Department of Chemistry, Faculty of Science, the National Sun Yat-sen University (NSYSU), Taiwan under the supervision of Asst. Prof. Dr. Cheng-chau Chiu. He has published articles in international journals and participated in international conferences (listed in APPENDIX C) during the course of his doctor's degree.